

Forcing and variability of northwestern inflows into the northern North Sea

Peter MF Sheehan PhD thesis

University of East Anglia
School of Environmental Sciences

January 2019

Supervisors

Karen Heywood
Rob Hall
University of East Anglia

Alejandro Gallego
Barbara Berx
Marine Scotland Science

University of East Anglia
Norwich Research Park
Norwich
NR4 7TJ
United Kingdom

Marine Scotland Science
375 Victoria Road
Aberdeen
AB11 9DB
United Kingdom

Thesis submitted to the School of Environmental Sciences of the University of East Anglia in partial fulfilment of the requirements for the degree of Doctor of Philosophy.

This copy of the thesis has been supplied on condition that anyone who consults it is understood to recognise that its copyright rests with the author and that use of any information derived there from must be in accordance with current UK copyright law. In addition, any quotation or extract must include full attribution.

© Peter Sheehan, 2019

ABSTRACT

Quantifying the volume of water flowing into the North Sea and understanding its temporal and spatial variability is essential for understanding, modelling and managing North Sea ecosystems. Here, northwestern inflows are studied using traditional and cutting-edge instrumentation from a hydrographic section. Long-term variability is assessed using a 27-year time series of temperature and salinity observations from hydrographic cruises. There is a pronounced annual cycle of temperature-driven thermohaline flow that is tied the growth and decay of stratification. When present, this flow is concentrated above a strong bottom front that separates mixed waters in the west from seasonally stratified waters in the east. The front is maintained in summer by the balance between tidal stirring and surface heating. Salinity-driven flow, not identified in previous studies, maintains appreciable thermohaline flow throughout the winter when thermal stratification is absent and when salinity gradients maintain the frontal boundary. Short-term variability is assessed using observations from a two-month ocean glider deployment in autumn of 2013. The properties of inflowing water masses are observed at high resolution. The distribution of fresh coastal water and saline oceanic water are more spatially variable than previously thought, and the decay of thermal stratification during the deployment permits a greater volume of oceanic water to enter the North Sea. Absolute transport (mean 0.44 Sv) calculated using glider dive-average currents indicate that the flow is predominantly barotropic, with a small contribution from thermohaline transport (mean 0.14 Sv). However, the limited width of the glider-occupied section hinders separation of spatial and temporal changes. Wind forcing, which acts to “push” water into the North Sea, has a moderate influence on daily current variability, likely because the presence of stratification and shallow Ekman layers promotes a two-layer flow structure. The advantages and disadvantages of ocean gliders as a shelf sea observing platform are considered.

Contents

List of figures vii
Acknowledgements ix
Publications xi

1 Introduction **1**
1.1 Thesis structure 5

2 Thermohaline forcing and interannual variability from ship observations **6**
2.1 Introduction 6
2.2 Methods 9
2.3 Mean conditions over an annual cycle 14
2.3.1 Winter 14
2.3.2 Spring 14
2.3.3 Summer 16
2.3.4 Autumn 18
2.4 Amplitude & phase of the annual cycle 19
2.5 Transport of the Atlantic inflow 22
2.6 Interannual variability 25
2.7 Summary 27

3 Tidal currents and mixing fronts **29**
3.1 Introduction 29
3.2 Glider-derived tidal velocities 31
3.2.1 Method 31
3.2.2 Tidal ellipses 35
3.2.3 Tidal velocities 35
3.3 Frontal location 37
3.3.1 Comparison with model output 39
3.3.2 Comparison with observations 41
3.4 Summary 43

4 Water masses, transport and forcing from glider observations 45
4.1 Introduction . . . 45
4.2 Glider data processing . . . 47
4.3 Hydrography . . . 53
4.3.1 Water masses . . . 53
4.3.2 Influence of tidal mixing . . . 58
4.4 Velocity and transport . . . 61
4.5 Non-thermohaline forcing . . . 67
4.5.1 Wind forcing . . . 67
4.5.2 Oceanic forcing . . . 72
4.6 Summary . . . 73

5 Conclusion 75

Appendix 79

A Heating-stirring model 79
A.1 Model modifications . . . 79
A.2 Model set-up . . . 83

References 84

List of Figures

1.1 Map of the North Sea . . . 3

2.1 Occupations of the JONSIS section . . . 10
2.2 Station and interpolated data . . . 13
2.3 Mean hydrography in winter . . . 15
2.4 Mean hydrography in spring . . . 16
2.5 Mean hydrography in summer . . . 17
2.6 Mean hydrography in autumn . . . 19
2.7 Amplitude and phase: temperature and salinity . . . 20
2.8 Amplitude and phase: geostrophic velocity . . . 21
2.9 Annual cycle of transport . . . 23
2.10 Interannual variability . . . 25

3.1 Binned dive-average currents . . . 32
3.2 Tidal ellipses . . . 34
3.3 Glider-derived and TPXO tidal velocities . . . 36
3.4 $log(h/u^3)$ and frontal location . . . 38
3.5 Surface heat flux in 2013 . . . 41
3.6 Exemplar glider occupation . . . 42

4.1 Salinity de-spiking . . . 48
4.2 Salinity de-spiking . . . 49
4.3 Dive locations and optimal interpolation . . . 51
4.4 Temperature and salinity sections . . . 54
4.5 Temperature-salinity diagram . . . 55
4.6 Backscatter and chlorophyll sections . . . 59
4.7 Gridded DACs . . . 62
4.8 Velocity sections . . . 64
4.9 Transport . . . 65
4.10 DAC and wind vector correlation . . . 69
4.11 Occupation-mean wind . . . 71

5.1 Ship-glider comparison 77

A.1 Comparison of heat flux estimates 81
A.2 Modelled temperature time series 82
A.3 Exemplar modelled sections 83

Acknowledgements

A thesis has one name on the front, but it is not the work of one person. Karen, Rob, Alejandro and Bee have been unfailingly helpful, patient and generous with their time. Their enthusiasm has inspired mine, and this thesis would not be here were it not for their support. Moreover, they have been great fun to work with. I am also deeply indebted to Bastien and Gillian. They're not my supervisors, but they have always been there to answer the kind of dumb questions I haven't wanted to ask anyone else; I can code in Matlab largely because of them. They, too, have been great fun to work with. And I am grateful to Marine Scotland Science, who gave me the opportunity not only to go to sea and take a good look at the JONSIS section for myself, but also to get out of my office and bother them in theirs for a while. Many of the ideas in this thesis came to me on one of those visits. To Marina, Helen, Denis, Michael and Stuart, to Jack, Steph, Kirsty and Pierre, I should probably apologise. All you wanted was a quiet morning, but I wanted to talk about Brexit. Loudly. Sorry. I have loved these last four years: thank you to everyone who's made it that way. I'm looking forward to sticking around.

This work was funded by NERC CASE PhD studentship number NE/L009242/1.

Publications

Chapters 2 and 3 have been published in peer-reviewed journals prior to the submission of this thesis. They are included as published, apart from the changes listed below.

Chapter 2

Sheehan, P. M. F., Berx, B., Gallego, A., Hall, R. A., Heywood, K. J. and Hughes, S. L. (2017). Thermohaline forcing and interannual variability of northwestern inflows into the northern North Sea, *Continental Shelf Research* **138**: 120 – 131.

PMFS carried out the research and prepared the paper. BB, AG, RAH, KJH and SLH supported the research and provided feedback on earlier drafts of the paper.

The map presented as Figure 1 in the published paper is not reproduced here: the reader is referred to Figure 1.1 of Chapter 1. Subsequent figures in this chapter have been re-numbered. The colour scheme used in Figure 2.2 has been improved. Density in Figures 2.3 to 2.6 has been changed from in situ density to potential density. Velocities changed from cm/s to m/s for consistency with other chapters.

Chapter 3

Sheehan, P. M. F., Berx, B., Gallego, A., Hall, R. A., Heywood, K. J., Hughes, S. L. and Queste, B. Y. (2018). Shelf sea tidal currents and mixing fronts determined from ocean glider observations, *Ocean Science* **14**: 225 – 236.

PMFS carried out the research and prepared the paper. SLH modified the heating-stirring model (see appendix A). BYQ provided advice on the processing of the glider data. BB, AG, RAH and KJH supported the research and provided feedback on earlier drafts of the paper.

The map presented as Figure 1 in the published paper is not reproduced here: the reader is referred to Figure 1.1 of Chapter 1. Subsequent figures in this chapter have been re-numbered. References to figures in the text have been changed from e.g. Fig. 2 to Figure 2 for consistency with other chapters.

Chapter 4 is presented as a draft paper.

Sheehan, P. M. F., Berx, B., Gallego, A., Hall, R. A., Heywood, K. J. and Queste, B. Y. *in prep*.

PMFS carried out the research and prepared the paper. BYQ provided advice on the processing of the glider data. BB, AG, RAH and KJH supported the research and provided feedback on earlier drafts.

Chapter 1

Introduction

The North Sea lies on the northwestern European continental shelf between continental Europe and the United Kingdom (Figure 1.1). It is a shallow sea, having a mean depth of only 74 m, although depths substantially shallower than this are found in the south, off the coasts of Germany and the Low Countries (Otto et al., 1990). Strong tidal currents, sharp gradients between water masses, and the passage of short-lived weather systems (Otto et al., 1990) create diverse and dynamic marine environments in which a variety of oceanic and atmospheric forcings vie for dominance. In addition, the pronounced seasonality of solar and atmospheric forcing in the mid-latitudes creates strong annual cycles in hydrography, ecology and circulation. In winter, wind is the principal driver of a circulation that is broadly cyclonic (Otto et al., 1990; Winther and Johannessen, 2006; Holt and Proctor, 2008; Mathis et al., 2015). In summer, when winds are weaker (Coelingh et al., 1996; Siegismund and Schrum, 2001), bottom temperature gradients between stratified regions, where solar heating is confined to the surface, and fully mixed regions, where solar heating reaches the sea floor, give rise to a system of narrow thermohaline (i.e. density-driven) jets, also cyclonic, that encircle the cool, dense waters trapped beneath the strong seasonal thermocline (Otto et al., 1990; Brown et al., 1999; Winther and Johannessen, 2006; Hill et al., 2008; Holt and Proctor, 2008); the total length of such frontal systems has been estimated to be at least 1500 km (Hill et al., 1993). In all seasons, forcing from the open ocean enhances the circulation, particularly at the boundaries (Holt and Proctor, 2008). This is most apparent in the northern North Sea: the open northern boundary, its close proximity to the northern Atlantic, and the low transport of the English Channel Inflow (ECI; Figure 1.1; Otto et al., 1990; Winther and Johannessen, 2006) combine to enhance the influence of Atlantic inflows on the northern North Sea compared with the southern North Sea. The Fair Isle Current (FIC), East Shetland Atlantic Inflow (ESAI) and Norwegian Trench Inflow (NTI; all Figure 1.1) advect the physical and biogeochemical properties of Atlantic waters into the North Sea (Dickson et al., 1988; Otto et al., 1990; Turrell et al., 1992; Holliday and Reid, 2001; Edwards et al., 2002; Emeis et al., 2015) and represent a key control on the hydrography, ecology and chemistry of the region (Lindley et al., 1990; Holliday

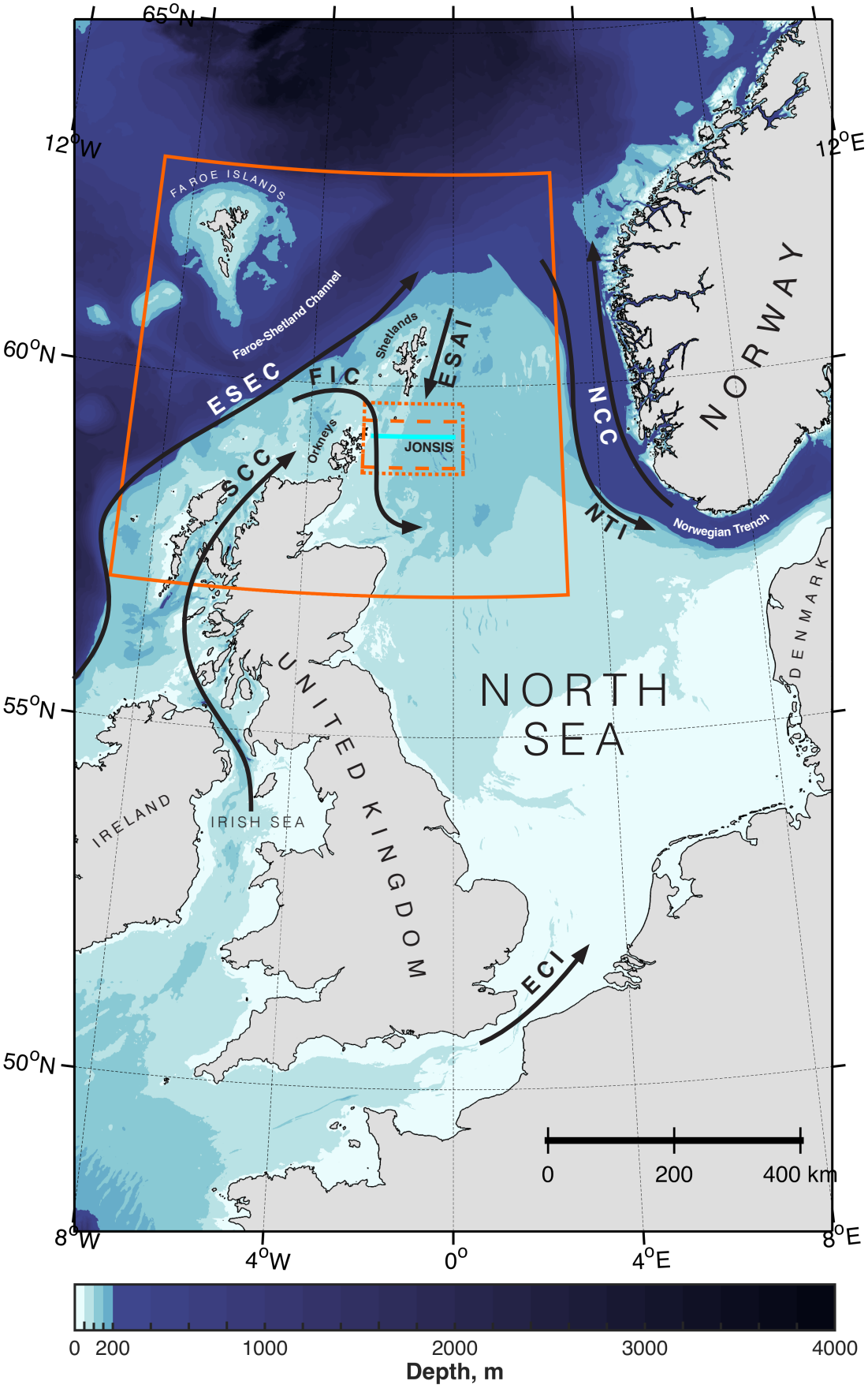
65°N
12°W
12°E
60°N
55°N
50°N
8°W
4°W
0°
4°E
8°E
FAROE ISLANDS
Faroe-Shetland Channel
ESEC
FIC
Shetlands
ESAI
JONSIS
Orkneys
SCC
NCC
NTI
Norwegian Trench
NORWAY
DENMARK
NORTH SEA
UNITED KINGDOM
IRELAND
IRISH SEA
ECI
0
200
400 km
0 200 1000 2000 3000 4000
Depth, m

Figure 1.1 Previous page Bathymetric map of the North Sea. The location of the JONSIS section (cyan line) and the approximate paths of key flows are shown: Fair Isle Current (FIC), East Shetland Atlantic Inflow (ESAI), Norwegian Trench Inflow (NTI), Norwegian Coastal Current (NCC), English Channel Inflow (ECI), the European Shelf Edge Current (ESEC) and the Scottish Coastal Current (SCC) (Otto et al., 1990; Turrell et al., 1996; Souza et al., 2001; Marsh et al., 2017). The area shown in Figure 3.1A and Figure 3.2 is enclosed within the dotted-line box; the area shown in Figure 4.3A is enclosed within the dashed-line box; and the area shown in Figures 4.10 and 4.11 is enclosed within the solid-line box. Contours are every 50 m up to 200 m and are every 200 m thereafter.

and Reid, 2001; Edwards et al., 2002; Beaugrand, 2004; Harwood et al., 2008; Leterme et al., 2008; Núñez-Riboni and Akimova, 2017). Outflow from the North Sea occurs in the Norwegian Coastal Current (NCC; Figure 1.1 Mork, 1981).

The North Sea has been affected by human activity for centuries: large-scale exploitation of fish stocks stretches back for almost a millenium (Barrett et al., 2004), although the Industrial Revolution accelerated and multiplied the impacts of human activity (Emeis et al., 2015). Today, the North Sea is one of the most managed, utilised and regulated shelf seas in the world (e.g. Claussen et al., 2009; Lenhart et al., 2010; Kannen, 2014; Merckelbach, 2016), being used for industrial-scale fishing, wind energy generation, oil and gas extraction, leisure and tourism, aquaculture and international shipping. Such a variety and intensity of use places unprecedented pressures on the marine environment that can influence both physical and ecological systems (e.g. Reiss et al., 2009; Matthias et al., 2010; Emeis et al., 2015; Wakelin et al., 2015). In response, management efforts have increase significantly in recent decades. Policies for the conservation, management and sustainable use of the North Sea have been developed at the national and sub-national level (e.g. *Scotland's National Marine Plan*, 2015). Meanwhile, the European Union provides a forum for supranational governance of the North Sea that has led to the adoption of regulations that apply across national borders (e.g. EU, 2000, 2008). These efforts provide an opportunity for the incorporation of science into policy (Claussen et al., 2009; Kannen, 2014) and add impetus to scientific efforts to understand the marine environment.

The North Sea, as is the case for shelf seas in general, is vulnerable to the effects of climate change (Holt et al., 2010), which can often act in concert with the effects of direct human activities discussed above (Wakelin et al., 2015). Rapid warming has been observed over the last three decades (Holt et al., 2010) and temperatures have been predicted to increase by between 1.5 and 3°C over the 21st century (Ådlandsvik, 2008; Holt et al., 2010). A comparison of hindcast simulations and observations has suggested that models may tend to underestimate the increase in temperature (Holt et al., 2012). In addition climate change has been predicted to increase the duration of the summer stratified period by around a fortnight (Holt et al., 2010). Processes attendant on stratification, such as frontal boundaries and thermohaline jets, may therefore be expected to become more significant as climate change progresses, and could prove to be a key mechanism by which warming influences circulation.

A decrease in salinity of around 0.2 psu is also possible, although large interannual variability in salinity makes trend detection difficult (Holt et al., 2010). Importantly, the physical and ecological impacts of climate change in the North Sea are not the same as in the nearby northern Atlantic (Holt et al., 2010; Gröger et al., 2013), so a specific understanding of the North Sea system is fundamental to developing dependable regional climate change forecasts.

Accurately predicting the future physical state of the North Sea is key to accurately predicting the future ecological state of the North Sea, as the region's physics has frequently been found to affect its ecology (Pingree et al., 1978; Kröncke et al., 1998; Holt and James, 1999; Holliday and Reid, 2001; Beaugrand, 2004; Edwards et al., 2006; Sharples, 2008; Kröncke, 2011; Alheit et al., 2012; Neumann et al., 2013). Many studies have examined the direct ecological effects of climate change – for instance, a possible increase in harmful algal blooms (Peperzak, 2003), an anticipated decrease in primary production (Gröger et al., 2013) and a decrease in abiotic carbon sequestration capacity (Thomas et al., 2007; Lorkowski et al., 2012); others have found links between ecology and climate processes such as the North Atlantic Oscillation (NAO; Ottersen et al., 2001; Kröncke et al., 2013). Consequently, existing biophysical relationships could allow climate change to indirectly influence the ecology of the North Sea through its effects on existing climate phenomena. In turn, ecological changes have the potential to alter climate: for instance, a predicted decrease in North Sea primary production could reduce the amount of North Sea biotic carbon dioxide absorbed by over 30% over the coming century (Gröger et al., 2013), thereby accelerating climate change.

The proximity of the North Sea to technologically advanced nations that have ancient relationships with the sea means that it has been the subject of scientific study almost since the advent of oceanography itself (e.g. Fulton, 1897), and that it is one of the best studied parts of the world ocean (Emeis et al., 2015). Nevertheless, the small scale of many of the North Sea's most important features, the dynamism of the system and its natural capacity to undergo rapid change are such that observational studies of the North Sea still present challenges to oceanography today. From an instrumental perspective, firstly, traditional platforms such as ships and moorings struggle to provide the spatial resolution needed to characterise narrow jets and sharp boundaries. Secondly, the importance of wind forcing means that velocity estimates from temperature and salinity observations that yield only thermohaline currents will likely underestimate flow. And thirdly, the close and well-documented connection between physical and ecological systems requires that we consistently observe physical and ecological variables together. From a scientific, policy and marine planning perspective, firstly, observing the North Sea at high temporal and spatial resolution is key to understanding how small-scale and highly variable features such as fronts and jets operate today, and to predicting how they might change in a warming climate. Secondly, the existence of a long observational record provides us with the opportunity to characterise interannual variability and establish climatological mean states (Berx and Hughes, 2009; van Leeuwen et al., 2015; Núñez-Riboni and Akimova, 2015) with greater certainty than is possible in less well-studied regions; but it remains challenging

to unambiguously distinguish between interannual variability and climate change. And finally, while the broad ”schematic” circulation has been known for some time (Figure 1.1; e.g. Turrell et al., 1996), the proximity of the North Sea to so many potential terrestrial and marine sources of pollution means that transport pathways need to be known precisely if the dispersion of pollutants is to be accurately forecast.

1.1 Thesis structure

In Chapter 2 (published as Sheehan et al., 2017, see page xi), a long-term time series of ship observations from a zonal hydrographic section in the northwestern North Sea (Figure 1.1) is complied from British and Norwegian data banks. Seasonal-mean hydrographic states are presented, an annual cycle of thermohaline flow is derived, and interannual variability is considered in the context of the NAO and the Atlantic Meridional Oscillation, a feature of sea-surface temperatures in the Atlantic. In Chapter 3 (published as Sheehan et al., 2018, see page xi), velocity observations from a two-month glider deployment at the same hydrographic section are introduced and a novel method to accurately derive tidal velocities from the glider observations – without recourse to a tide model – is described. These tidal velocities are used to investigate the influence of tidal mixing on the location of a meridional bottom front that crosses the section. In Chapter 4, water masses from the same glider deployment are analysed, absolute transport across the hydrographic section is calculated, and the day-to-day influence of wind forcing on flow across the section is quantified using a statistical technique. The results of Chapters 2 to 4 are synthesised in the conclusion (Chapter 5) and the advantages of gliders to shelf-sea observing systems are discussed.

Chapter 2

Thermohaline forcing and interannual variability of northwestern inflows into the northern North Sea

2.1 Introduction

The North Sea is a shallow shelf sea on the northwestern European continental shelf that lies between the United Kingdom and continental Europe (Figure 1.1). Inflow to the North Sea from the northern Atlantic occurs through the English Channel (English Channel Inflow), between the Orkney and Shetland Islands (Fair Isle Current, FIC), along the eastern coast of the Shetland Islands (East Shetland Atlantic Inflow, ESAI), and along the western slope of the Norwegian Trench (Norwegian Trench Inflow; Otto et al., 1990; Svendsen et al., 1991; Turrell et al., 1996). Outflow occurs primarily in the Norwegian Coastal Current (NCC; Damm et al., 1994). The approximate locations of these flows are illustrated in Figure 1.1. These currents are, in turn, largely fed by the Shelf-Edge Current, which flows northwards along the European continental margin (Turrell et al., 1996; Marsh et al., 2017). Input to the FIC also occurs from the Scottish Coastal Current, a northward flow along the western coast of Scotland. The English Channel Inflow is weak compared with the northern inflows (Otto et al., 1990; Winther and Johannessen, 2006). The Norwegian Trench Inflow is the largest by volume transport (Otto et al., 1990; Winther and Johannessen, 2006) but it retroflects within the Norwegian Trench and flows out with the NCC. Consequently, it is the FIC and ESAI, the northwestern inflows, that have the greatest effect on conditions in the northern North Sea. The waters of the northwestern inflows approximately follow the 100 m isobath southwards down the eastern coast

of Scotland before turning eastwards between 57.5 and 58°N and flowing towards Norway. Within the North Sea, the circulation is broadly cyclonic (Otto et al., 1990; Hill et al., 2008).

The rate of oceanic inflow strongly influences the region's ecosystem (Lindley et al., 1990; Holliday and Reid, 2001; Edwards et al., 2002; Beaugrand, 2004), and the FIC and ESAI provide pathways for perturbations of oceanic origin to propagate into the North Sea (Dickson et al., 1988; Holliday and Reid, 2001; Edwards et al., 2002). Reliable models of contaminant pathways and of water quality depend on accurate knowledge of these inflows (Taylor, 1987; Turrell and Henderson, 1990); reliable models of phytoplankton and nutrient distributions depend on proper physical modelling (Skogen and Moll, 2005). In the last decade, the EU's Marine Strategy Framework Directive has placed on EU member states the responsibility of ensuring "good environmental status" (EU, 2008) for their territorial waters, so providing a regional regulatory driver to efforts to improve our understanding of the physical and ecological dynamics of the North Sea.

The FIC has been described in broad terms as a southward-flowing current, approximately 30 nautical miles (56 km) wide (Svendsen et al., 1991), that flows through the Fair Isle Gap between the Orkney and Shetland islands (Dooley, 1974). In the North Sea, it is found close to the eastern coast of the Orkneys (Svendsen et al., 1991) in the approximate region of the 100 m isobath (Dooley, 1974; Winther and Johannessen, 2006). The ESAI is a more recent discovery than the FIC. In his review of the circulation of the northern North Sea, Dooley (1974) did not find evidence of a persistent inflow to the east of the Shetlands, but studies since then have found evidence of such a flow (Turrell, 1992; Turrell et al., 1996). Winther and Johannessen (2006) note that the ESAI is a more diffuse flow than the FIC, but that average transports in the two currents are similar. Between 57.5 and 58°N, the combined inflow turns east and flows towards the Norwegian coast in what has become known as the Dooley Current (Dooley, 1974; Otto et al., 1990; Winther and Johannessen, 2006). Little water from northwestern inflows reaches the southern North Sea (Pohlmann and Puls, 1994).

Previous studies in the region (e.g. Turrell, 1992) have separated the Atlantic inflow into wind-driven and non-wind-driven components, and have assumed that the wind-driven component represents the depth-constant flow that remains once the bottom-referenced geostrophic shear has been removed from the velocity profile. Subsequent references to wind- and non-wind-driven flow follow this convention.

The Atlantic inflow exhibits seasonal variations (Dooley, 1983; Turrell, 1992). It is thought to be primarily non-wind-driven in summer and primarily wind-driven in winter (Dooley, 1983; Otto et al., 1990; Svendsen et al., 1991; Turrell, 1992; Pohlmann and Puls, 1994; Winther and Johannessen, 2006). During the spring, stratification develops offshore of both the Orkney and Shetland archipelagoes as atmospheric heating warms the surface, isolating cool, dense waters left over from the previous winter beneath the thermocline (Svendsen et al., 1991; Turrell, 1992; Turrell et al., 1996; Hill et al., 2008). Closer to the shore, tidal currents are sufficiently strong that the water column remains fully mixed even when deeper, offshore waters are

stratified (Svendsen et al., 1991). The density front that emerges between these two regions drives an along-front jet between the dense bottom water in the offshore, stratified region and the lighter water in the coastal mixed region (Svendsen et al., 1991; Turrell, 1992; Hill et al., 2008). This density pattern is common on the northwestern European shelf and makes the FIC and ESAI part of the thermohaline circulation that is a common feature on the northwestern European shelf in summer (Brown et al., 1999; Hill et al., 2008). The zonal salinity distribution reinforces this density pattern. The waters of the FIC originate along the western coast of Scotland where, prior to entering the North Sea, they are mixed with fresh water of terrestrial origin (Turrell et al., 1990; Turrell, 1992). The salinity gradient between water that exhibits this fresh water influence and more saline water found offshore may be traced around the northern coast of Scotland (Dooley, 1974). The lack of major river systems on, and the relatively small landmass of, the Orkney and Shetland Islands, means that further appreciable addition of fresh water to the FIC and ESAI from terrestrial sources does not occur in the vicinity of these archipelagoes.

The switch to a wind-driven regime occurs because wind forcing is stronger in winter (Coelingh et al., 1996; Siegismund and Schrum, 2001). Winds from the west and north tend to force an anti-clockwise circulation around the northern North Sea, a pattern that promotes inflow of water from the northwest (Furnes, 1980). The correlation between volume transport in the inflows and the North Atlantic Oscillation (NAO; Hurrell et al., 2003), an index which characterises the meridional pressure difference across the northern Atlantic and the strength of westerly winds in the region, is higher at this time of year than it is in summer (Winther and Johannessen, 2006; Hjøllo et al., 2009). The breakdown of thermal stratification is also important (Turrell et al., 1990): the disappearance of the thermocline enhances Ekman transport throughout the water column (Winther and Johannessen, 2006) and reduces the density difference between near- and offshore regions, lessening the influence of the horizontal density gradient on the circulation (Turrell, 1992). A horizontal salinity gradient persists between the low-salinity coastal water and the high-salinity water of Atlantic origin towards the centre of the North Sea (Turrell, 1992), but Prandle (1984) estimates that it drives a flow an order of magnitude less than that driven by the wind.

Our understanding of the annual cycle of non-wind-driven flow in the Atlantic inflow has, to date, been based on observations from limited periods of time. Previous studies have relied on current meter records from a few months and on hydrographic observations from single cruises (e.g. Furnes, 1980; Turrell et al., 1990; Brown et al., 1999). Descriptions of the hydrography and flow in the region based on long-term observations are lacking in the literature. Volume fluxes are known to be limited by narrow sampling windows when estimated from observations (Hjøllo et al., 2009), and the role of non-wind-driven forcing in winter is not well understood (Dooley, 1983). Furthermore, the effect of horizontal temperature and salinity gradients on the non-wind-driven flow is yet to be considered separately. That stratification and horizontal temperature gradients influence the current has been understood for some time (Backhaus

and Maier-Reimer, 1983; Turrell, 1992), as has the role of thermohaline circulation in the shelf seas more generally (Hill et al., 2008). The influence of horizontal salinity gradients on the Atlantic inflow has received less attention, and no attempt has been made to describe and quantify the separate influence of temperature and salinity gradients.

This chapter analyses 27 years of data from a hydrographic section in the northern North Sea. The annual cycle of non-wind-driven forcing of, and transport in, the Atlantic inflow is quantified from this newly compiled data set, and the separate roles played by temperature and salinity on the non-wind-driven forcing are investigated.

2.2 Methods

The Joint North Sea Information System (JONSIS) section is a zonal section between 2.233°W and the prime meridian at 59.28°N (Figure 1.1). The section is occupied multiple times a year (Figure 2.1) by Scottish research ships, which sample at 12 stations, and Norwegian research ships, which occupy a section at the same latitude known as the Orkney-Utsire section that crosses the entire North Sea; eight stations on the Orkney-Utsire section fall between 0°and 2.233°W (Figure 2.1). Temperature and salinity profiles from Scottish occupations were obtained from Marine Scotland's data archive; temperature and salinity profiles from Norwegian occupations were obtained from the online data portal of the International Council for the Exploration of the Sea[1] (ICES). Scottish and Norwegian data were visually inspected to identify complete occupations; isolated data points, occupations with fewer than eight stations, occupations with unevenly spaced stations, and occupations with poor vertical resolution (i.e. profiles with measurements at greater than 1 m intervals, the standard being 1 m resolution) were rejected. The combined Scottish-Norwegian dataset comprises 122 occupations, between December 1989 and April 2015 (Figure 2.1). Data are available for every month apart from August; a limited number of occupations are available for January, February and March, and only one occupation is available for June (Figure 2.1). In situ temperature and practical salinity were converted into conservative temperature and absolute salinity respectively (IOC et al., 2010); all subsequent uses of temperature and salinity refer to these TEOS-10 variables. This definition of salinity gives values that are typically 0.2 higher than those reported in previous studies that used different definitions of salinity.

An objective mapping technique (Bretherton et al., 1976; Denman and Freeland, 1985; Chereskin and Trunnell, 1996) based on a Gaussian weighting function was used to interpolate the data onto a regular grid. Grid spacing was 0.01° (568 m) in the horizontal and 2 m in the vertical. Semivariograms were used to determine appropriate correlation length scales for the mapping process. Semivariograms quantify the dissimilarity (i.e. the semivariance) between observations as a function of the distance between them (Schaeffer et al.,

[1] www.ocean.ices.dk/HydChem

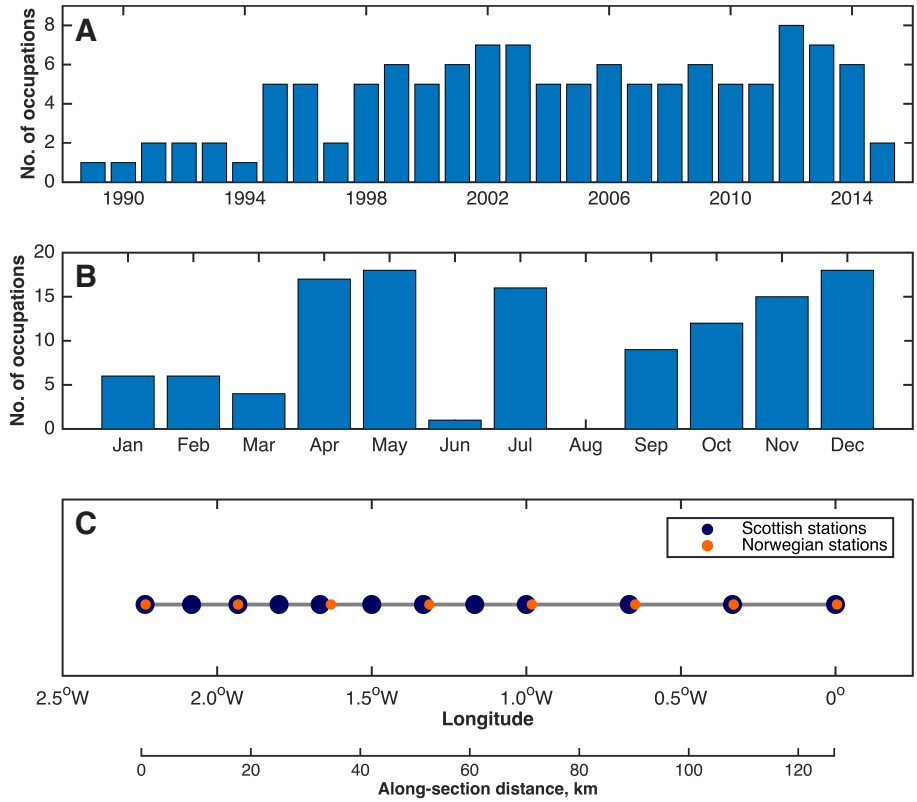

Figure 2.1 Occupations of the JONSIS section: **A** by year and **B** by month. **C** Scottish and Norwegian stations on the JONSIS section (59.28°N).

2015). The maximum permissible correlation length scale is the distance at which dissimilarity ceases to increase with distance, although the correlation length scale may be set below this maximum (Janssen et al., 1999). The correlation length scales were 0.3° longitude (28.4 km) and 2 m in the horizontal and vertical respectively. These values are considerably less than the maximum possible correlation length scales, reflecting the need to use only the most closely correlated neighbouring data points in the interpolation, for instance, to preserve sharp thermoclines. Larger length scales produced temperature and salinity fields that were unrealistically smooth and which did not agree well with the non-gridded observations. More information on semivariogram analysis is presented in Box 2.1 on page 11.

After the objective mapping process, in cases where the observations did not cover the entire water column, the deepest interpolated measurement was extrapolated to the seafloor using a fixed-value method; similarly, where necessary the shallowest interpolated measurement was extrapolated to the surface using a fixed-value method. Such extrapolations were carried out over a depth range of typically no more than 5 m, and extrapolations to the surface were always within the surface mixed layer. Bathymetry was extracted from the GEBCO dataset[2] (resolution 30 arc-seconds). An example Marine Scotland occupation from September

[2]GEBCO_08 grid, version 20100927, www.gebco.net

BOX 2.1 Semivariograms

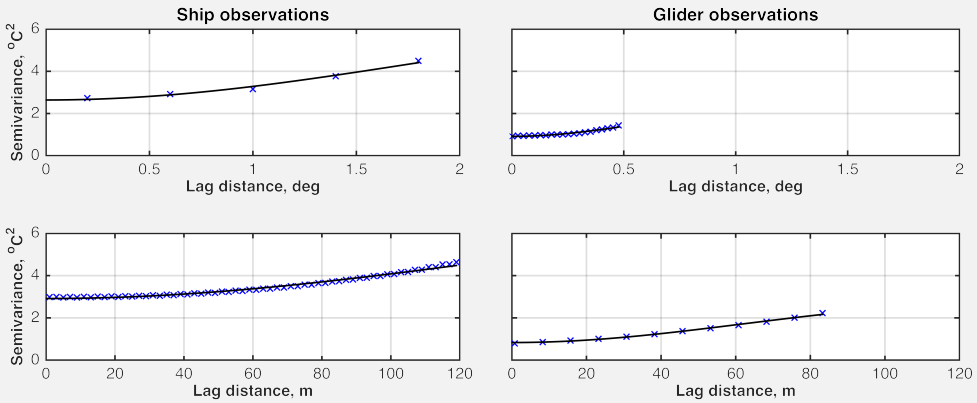

A semivariogram quantifies the dissimilarity of a sample of a variable contained within a window of a given size. The size of this window is known as the lag distance. Semivariograms plotted from ship and glider temperature observations are shown in the left and right panels respectively in the above figure.

The lag distance is progressively increased by a constant increment and the variance of the observations within that lag distance is calculated. The variance may be expected to increase with increasing lag distance until it equals the variance of the underlying data. Variance is plotted against lag distance to produce an empirical semivariogram (blue crosses in the above figure). Using a least-squares method, a theoretical semivariogram is fitted to the empirical semivariogram (black lines in the above figure). A theoretical semivariogram may be defined by one of a number of functions (e.g. Guassian, spherical, exponential), the most appropriate being that which provides the best fit to the empirical semivariogram (i.e. highest R^2). The glider and ship data described in this chapter and in Chapter 4 were best described using a Gaussian semivariogram.

A theoretical semivariogram yields three key parameters: the sill, the range and the nugget. The sill is the estimated value of the variance of the underlying observations: it is the maximum value of semivariance reached in the analysis. The range is the magnitude of the lag distance at which the sill is reached. This is taken to be the maximum distance at which two points in the distribution are correlated and is the maximum length scale that may be used in optimal interpolation. The nugget is the variance calculated at a zero lag distance, and is taken to represent error inherent in the sampling scheme. The nugget is higher for the ship observations than for the glider observations because the ship observations cover a period of 27 years, where as the glider observations cover only two months; over a 27-year period, the variance of temperature at a single point may reasonably be expected to be higher than over a two-month period.

1990 showing observations and the interpolated data is presented in Figure 2.2. The instrumental and gridding errors are estimated to be two to three orders of magnitude smaller than the variability discussed in Sections 2.3 to 2.6.

Hydrographic data are presented as seasonal (JFM, AMJ, JAS and OND) mean sections; volume transport is presented as monthly mean values. Geostrophic velocity and volume transport are calculated occupation by occupation, prior to averaging, rather than from seasonally averaged distributions of temperature and salinity. Geostrophic velocity is calculated relative to an assumed level-of-no-motion at the deepest common level between adjacent horizontal grid points. The geostrophic approximation is discussed in Box 2.2 on page 12. In order to assess the relative contributions that temperature and salinity make to this velocity,

BOX 2.2 The geostrophic approximation

The geostrophic approximation is used to simplify the momentum equations, which for meridional motion, as considered in this chapter, is:

$$\frac{dv}{dt} = -\frac{1}{\rho}\frac{\partial p}{\partial y} - 2u\Omega \sin\phi u + F$$

where $\frac{dv}{dt}$ is acceleration, ρ is density, $\frac{\partial p}{\partial y}$ is the pressure gradient force, u is zonal velocity, Ω is the angular velocity of the earth, ϕ is latitude and F is friction. When calculating geostrophic velocity, friction is assumed to be negligible and that acceleration is assumed to be an order of magnitude smaller than both the pressure gradient force and the Coriolis force. The above equation then simplifies to

$$-\frac{1}{\rho}\frac{\partial p}{\partial y} - 2u\Omega \sin\phi u = 0$$

in which case the pressure gradient force is exactly balanced by the Coriolis force; all other processes that can affect flow are ignored. Crucially, the lack of acceleration means that geostrophic flow occurs only in a straight line. Furthermore, the geostrophic approximation is valid only as spatial scales greater than the local Rossby radius: observations are smoothed at this Radius before geostrophic velocities are calculated, but in shelf seas it is likely that many processes – for instance, wind-driven currents – operate at smaller spatial scales.

The lack of an acceleration term in the geostrophic equations is particularly limiting to the application of the geostrophic approximation in dynamic shelf sea environments. Firstly, changes to the density gradients that drive baroclinic geostrophic flows that occur on timescales shorter than approximately a day are ageostrophic. Secondly, non-straight-line flows, such as occur when currents such as the FIC are steered by topography, are ageostrophic.
The temporal spacing of occupations used in this chapter is such that small-scale temporal changes will not be resolved. Furthermore, this chapter considers considers only the flow across a zonal section: we do not try to describe the flow along its path, for example, in which case the lack of acceleration in the geostrophic approximation might be more of a limitation.

The exclusion of friction may be similarly limiting in shelf seas. Bottom friction is particularly significant in shelf seas, where a greater proportion of the water column is affected by bottom friction than in the deep ocean. As a consequence, the thermohaline flow as defined in this chapter, may be expected to include an ageostrophic component introduced by friction. Friction reduces the speed of a flow, which reduces the magnitude of the Coriolis force, which is dependent on speed. The pressure gradient force then becomes the larger of the two terms, deflecting the flow down the pressure gradient. In this results presented here, this would reduce the meridional velocity and would introduce a component of thermohaline flow in the offshore direction.

the components of geostrophic flow driven by the temperature and salinity distributions are also calculated. The temperature-driven component is defined as the geostrophic velocity calculated using the observed temperature distribution for a given occupation and an artificial salinity distribution in which salinity is constant in space. The salinity-driven component is defined as the geostrophic velocity calculated using the observed salinity distribution for a given occupation and an artificial temperature distribution in which temperature is constant in space. The constant salinity value is the spatial and temporal mean salinity calculated from all 122 occupations (35.33 g kg^{-1}); the constant temperature value is the spatial and temporal mean temperature calculated from all 122 occupations (9.05°C). So if geostrophic velocity, v, is a function of temperature, t, salinity, S and depth, z, the temperature-driven component is $v(t, \overline{S}, z)$ and the salinity-driven component is $v(\overline{t}, S, z)$ where an overbar denotes a spatial and temporal mean.

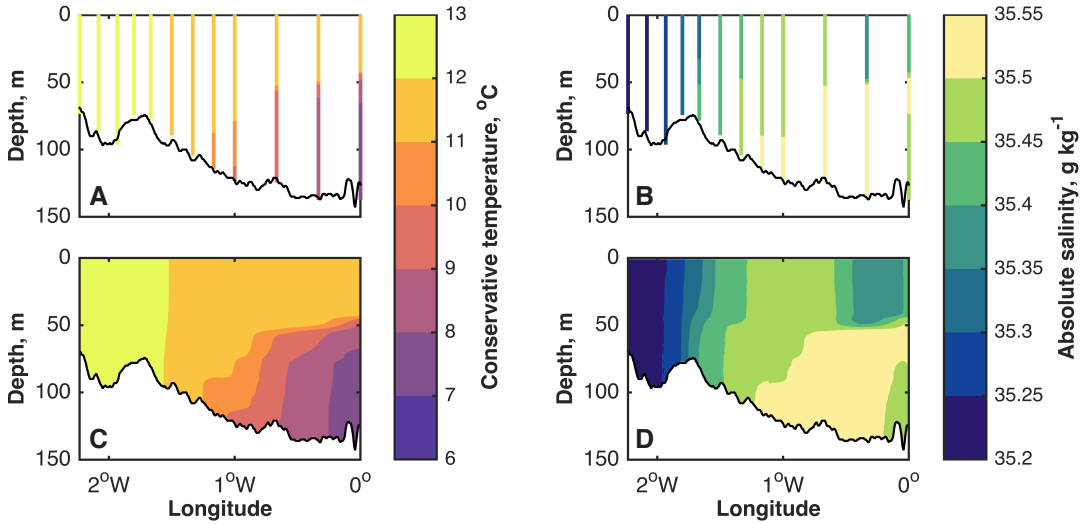

Figure 2.2 A comparison of station data and interpolated data for an exemplar occupation **A** Observations of conservative temperature (°C) and **B** observations of absolute salinity (g kg^{-1}). **C** Optimally interpolated conservative temperature (°C) and **D** optimally interpolated absolute salinity (g kg^{-1}).

The amplitudes and phases of the annual cycle of temperature, salinity and geostrophic velocity at each grid point are calculated using a harmonic analysis method (Thomson and Emery, 2014); the fitted (cos)sinusoids are required have a period of 365 days. This allows the construction of a sinusoidal annual cycle at each grid point for the three variables. Sampling a grid point's sinusoid at the time of each occupation and subtracting this value from the observed value permits the calculation of residual distributions of temperature, salinity and geostrophic velocity for each occupation. We will refer to these as de-seasoned distributions. Similarly, a sinusoidal annual cycle of 365 days is fitted to the time series of volume transport, and the residual (de-seasoned) time series calculated. The de-seasoned variables, once spatially averaged by occupation, are used to calculate the one-dimensional time series of occupation-mean temperature, occupation-mean salinity and occupation-integrated volume transport discussed in Section 2.6. Long-term trends were not removed from the data. The NAO index used in Section 2.6 was downloaded from NOAA's Climate Prediction Centre[3], and the Atlantic Multidecadal Oscillation (AMO) index, which characterises the interdecadal variability of sea-surface temperature in the Atlantic once the signal of anthropogenic climate change has been removed (Schlesinger and Ramankutty, 1994; Trenberth and Shea, 2006), was downloaded from NOAA's Earth System Research Laboratory[4].

[3] www.cpc.ncep.noaa.gov/products/precip/CWlink/pna/nao.shtml
[4] www.esrl.noaa.gov/psd/data/timeseries/AMO; un-smoothed product

2.3 Mean conditions over an annual cycle

2.3.1 Winter

In winter, there is very little spatial variation in temperature, either horizontally or vertically (Figure 2.3A). Consequently, the temperature-driven component of the geostrophic flow is small: current speeds peak at approximately 0.01 m s^{-1} flowing northward in the far west of the section. The horizontal salinity gradient is strong (Figure 2.3B). Salinity increases from less than 35 g kg^{-1} at the western limit of the section to over 35.4 g kg^{-1} at the eastern limit. The strongest salinity gradient, the boundary between low-salinity coastal water and high-salinity water of Atlantic origin (Dooley, 1974; Turrell et al., 1990), is found west of 1.5°W. This salinity gradient drives a salinity-dependent geostrophic flow approximately 60 km wide with peak southward current speeds of over 4 cm s^{-1}. The salinity-driven flow is at its strongest in March, when southward current speeds exceed 0.07 m s^{-1} at the surface. This is caused by a strengthening of the horizontal salinity gradient between 1.5 and 2°W.

The signal of the salinity-driven component is clearly visible in the depth-varying geostrophic flow (Figure 2.3C). The weak temperature-driven component has little impact, despite flowing in the opposite direction. The identification of a marked horizontal salinity gradient across the JONSIS line in winter, particularly in March, and the attribution to this gradient of a defined depth-varying southward current, provides evidence of the winter-time non-wind-driven component of the Atlantic inflow proposed by Dooley (1983) but thought non-existent by Turrell (1992). However, contrary to the suggestion of Dooley (1983), this component is a narrow, near-coast feature, rather than being spread over too wide an area to be readily observed.

The mean surface geostrophic currents are slower than those predicted by models when the influence of the wind is taken into account. Winther and Johannessen (2006), in a modelling study that includes wind-driven flow, find surface currents across the western part of the JONSIS section to be approximately 0.2 m s^{-1} in February; in the east, current speeds are approximately 0.06 m s^{-1}. That such current speeds are not observed in the present study when wind forcing is not taken into account is consistent with the dominant role played by the wind in driving Atlantic inflow in winter.

2.3.2 Spring

In spring, thermal stratification begins to develop in the eastern half of the JONSIS section (Figure 2.4A). The lack of stratification west of 1.5°W is evidence of the near-shore tidal mixing identified by Svendsen et al. (1991). The weak horizontal temperature gradient between the stratified and mixed regimes induces a weak, southward, temperature-driven component of the geostrophic flow, with maximum speeds of only 0.01 m s^{-1}. This temperature-driven flow strengthens as spring progresses. There is only one occupation available in June (Figure 2.1), but this occupation has a temperature-driven flow faster (0.04 m s^{-1}) and wider (50 km) than

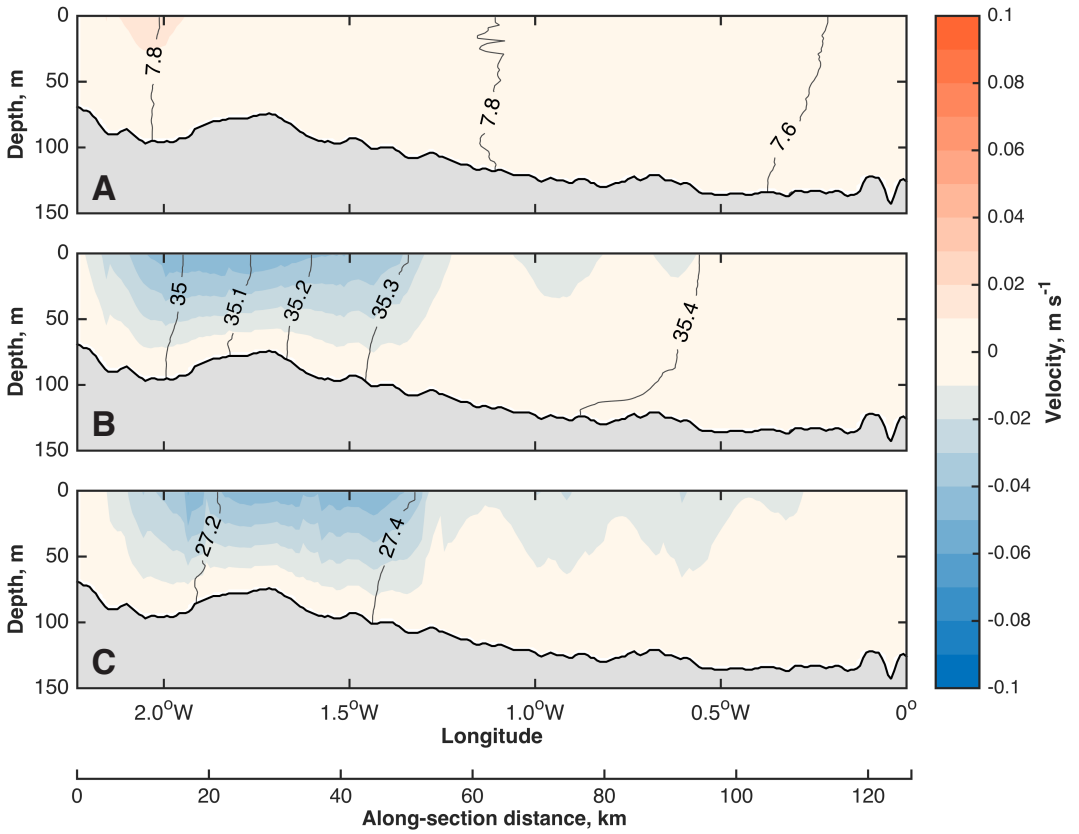

Figure 2.3 Mean conditions in winter: January, February and March. **A** Geostrophic velocity calculated using an assumed uniform salinity of 35.33 g kg^{-1} (shading; m s^{-1}); conservative temperature (contours; °C). **B** Geostrophic velocity calculated using an assumed uniform temperature of 9.05°C (shading; cm s^{-1}); absolute salinity (contours; g kg^{-1}). **C** Geostrophic velocity (shading; m s^{-1}); density (contours; kg m^{-3}). Negative velocity indicates southward flow.

the average presented here. Mean salinity in the far west of the section is higher than in winter, and a slight surface freshening leads to the development of a weak halocline east of 1.5°W (Figure 2.4B). The increase in salinity in the west of the section is balanced by the westward expansion of high-salinity water, as demonstrated by the westward displacement of the 35.4 g kg^{-1} isohaline, rather than by a commensurate salinity increase in the east. This contradicts previous studies which found that the horizontal salinity gradient was kept constant by equal changes in the salinity across the FIC, rather than to changes to the extent of high- and low-salinity waters (Turrell, 1992). The salinity-driven component of the geostrophic flow remains of a comparable speed to that in winter, but is narrower (approximately 40 km wide) and centred further east. In the single June occupation, the salinity-driven flow is much weaker than this average, being 30 km wide and having a maximum speed of 0.02 m s^{-1}.

The geostrophic flow observed in spring (Figure 2.4C) is present as two separate cores with peak southward velocities of over 0.05 m s^{-1}, one centred at 2.1 °W and the other at 1.6 °W. The western core is driven by the salinity component. The eastern core is driven primarily by

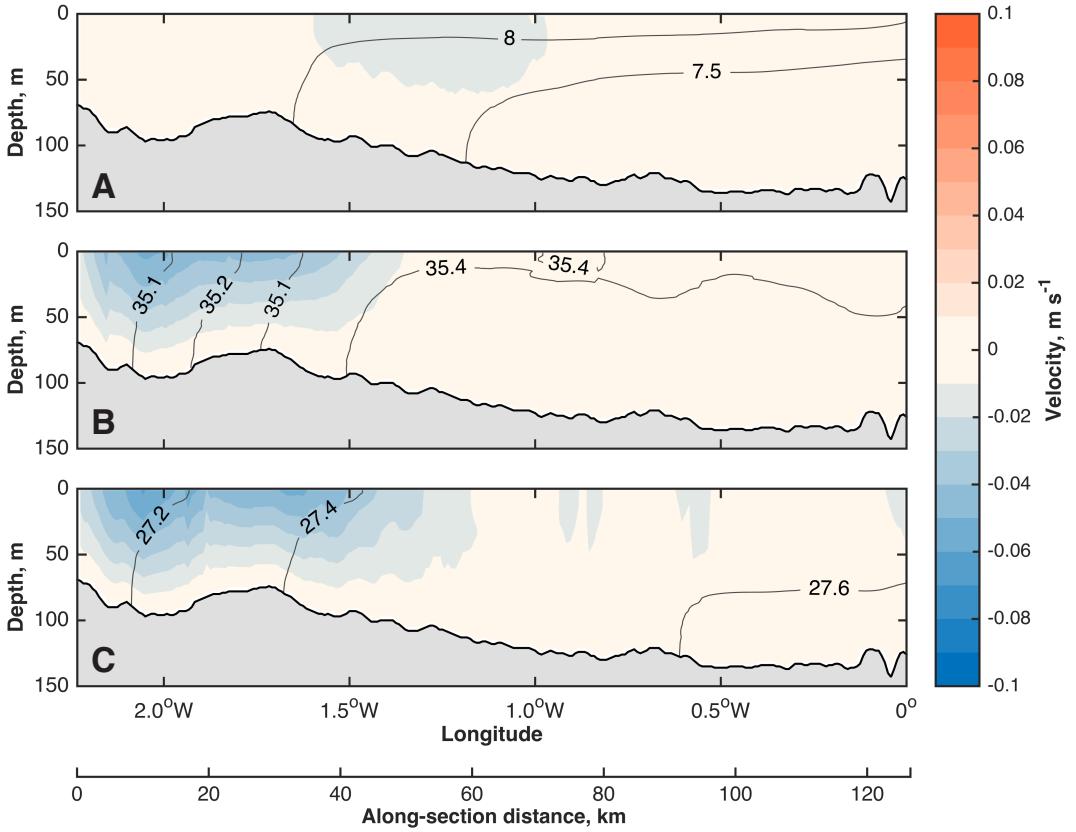

Figure 2.4 Mean conditions in spring: April, May and June. Panels, shading, contours and units are as in Figure 2.3.

the salinity component, but with a contribution from the temperature component. An individual occupation may exhibit either one or both of the cores visible in the long-term mean. The temperature component appears to be responsible for the region of low velocity (< 0.02 m s^{-1}) flow that extends to the east of the eastern core. The results for spring are in better agreement than those for winter with the model results of Winther and Johannessen (2006). In June, in the west of the section, they report surface speeds of approximately 0.1 m s^{-1}, and in the east report surface speeds of below 0.04 m s^{-1}. This suggests that, as stratification develops, the non-wind-driven flow accounts for a greater proportion of total flow than it did in winter, both as the wind-driven component of the flow has weakened and the non-wind-driven component has strengthened.

2.3.3 Summer

Thermal stratification reaches its peak over the summer, as surface temperatures in an average year exceed 13°C (Figure 2.5A). Tidal stirring west of 1.5°W mixes heat throughout the water column: bottom temperatures in the mixed region are approximately 4°C higher than bottom temperatures in the stratified region. Temperature-driven flow is present across almost the

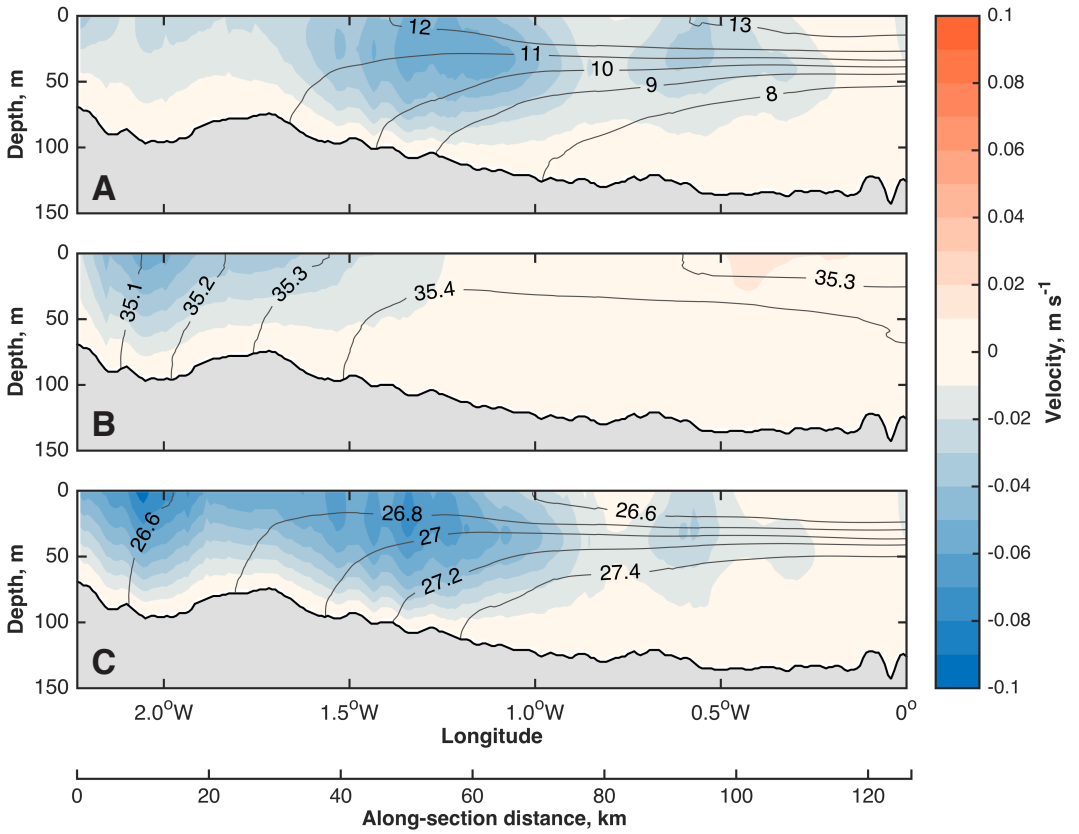

Figure 2.5 Mean conditions in summer: July and September (there are no data for August). Panels, shading, contours and units are as in Figure 2.3.

entire width of the section, but principally in a central core between 1 and 1.5°W with speeds in excess of 0.05 m s^{-1}. As the summer progresses, temperature-driven current speeds in this central core increase as those to the west decrease. The freshening of surface waters in the east of the section has continued since the spring (Figure 2.5B). This is likely evidence of incursions of low-salinity water from the NCC, transported westward across the northern North Sea via Ekman transport driven by northerly winds in summer (Sætre et al., 1988). Turrell et al. (1992) find evidence of this water in September 1987 in the centre of the northern North Sea. The salinity-driven component of the geostrophic flow remains confined to the western limit of the section. The speed of the salinity-driven flow reaches a maximum of 0.05 m s^{-1} at 2.1°W, although in September this flow is broader (70 km) and considerably slower (0.03 m s^{-1}) and than the average presented here. Together, the temperature and salinity stratification east of 1.5°W give rise to strong density stratification (Figure 2.5C).

Depth-varying geostrophic flow is at its fastest (0.07 m s^{-1}) in summer (Figure 2.5C). The contributions of both the temperature- and salinity-driven components can be seen clearly. The central core of the flow, centred between 1 and 1.5°W, is driven by the temperature component, as is the weaker eastern core (0.6°W). The western core, centred at 2.6°W, is driven by the salinity component, but is amplified by the weak (0.02 m s^{-1}) temperature component that is

also found in that region.

The strongly stratified regime that these results confirm explains the different response of the Atlantic inflow to wind forcing in summer compared with winter. The effects of wind forcing take longer to be felt in summer (15 to 20 hours) than in winter (0 hours; Turrell et al., 1992). At a time when the FIC is driven primarily by the horizontal density gradient (Turrell, 1992), and when stratification inhibits a barotropic response to wind forcing, it is the horizontal density gradient (Figure 2.5C) that must adjust to changes in the overlying wind stress. Turrell et al. (1992) propose that northerly winds promote the inflow of high-salinity Atlantic water that, at the JONSIS section, sits beneath the thermocline (Figure 2.5B). In turn, this strengthens the horizontal salinity gradient and so increases geostrophic flow. Conversely, they propose that southwesterly winds reduce the inflow of high-salinity Atlantic water and so weaken the horizontal salinity gradient (Turrell et al., 1992). Winther and Johannessen (2006) find that northerly winds lead to upwelling of approximately 0.5 m day^{-1} around the coast of the Shetland Islands, increasing northwards towards the shelf break. This, too, could bring high-salinity water of Atlantic origin into the northern North Sea.

2.3.4 Autumn

Temperature stratification and salinity stratification weaken in the autumn (Figure 2.6A and B). The horizontal gradients also weaken substantially, with a corresponding weakening of the temperature- and salinity-driven components of the geostrophic flow. Maximum temperature-driven speeds are 0.03 m s^{-1}; maximum salinity-driven speeds are 0.04 m s^{-1}. A reversal of the horizontal salinity gradient between 0.2 and 0.5°W induces a weak (0.01 m s^{-1}) northward flow at the same location. Month to month, as autumn progresses, the core of the temperature-driven flow moves eastward as the location of the horizontal temperature gradient moves offshore. The location of the salinity-driven flow remains largely unchanged. The maximum speed of the geostrophic flow is 0.05 m s^{-1}, but the flow is at its broadest (approximately 110 km) in autumn. The western part of the flow is driven by the salinity component; the eastern part of the flow is driven by the temperature component. The region of weaker flow at 0.2°W appears to be a result of the northward salinity-driven flow mentioned above.

Results from the Autumn Circulation Experiment suggest that wind forcing switches from the summer, non-wind-driven regime to the winter, wind-driven regime in November and December (Turrell et al., 1990). By December, once stratification has decayed almost completely, greatest inflow is induced by southwesterly winds (Turrell et al., 1990). This suggests that a barotropic response to wind forcing is once again dominant by the end of autumn.

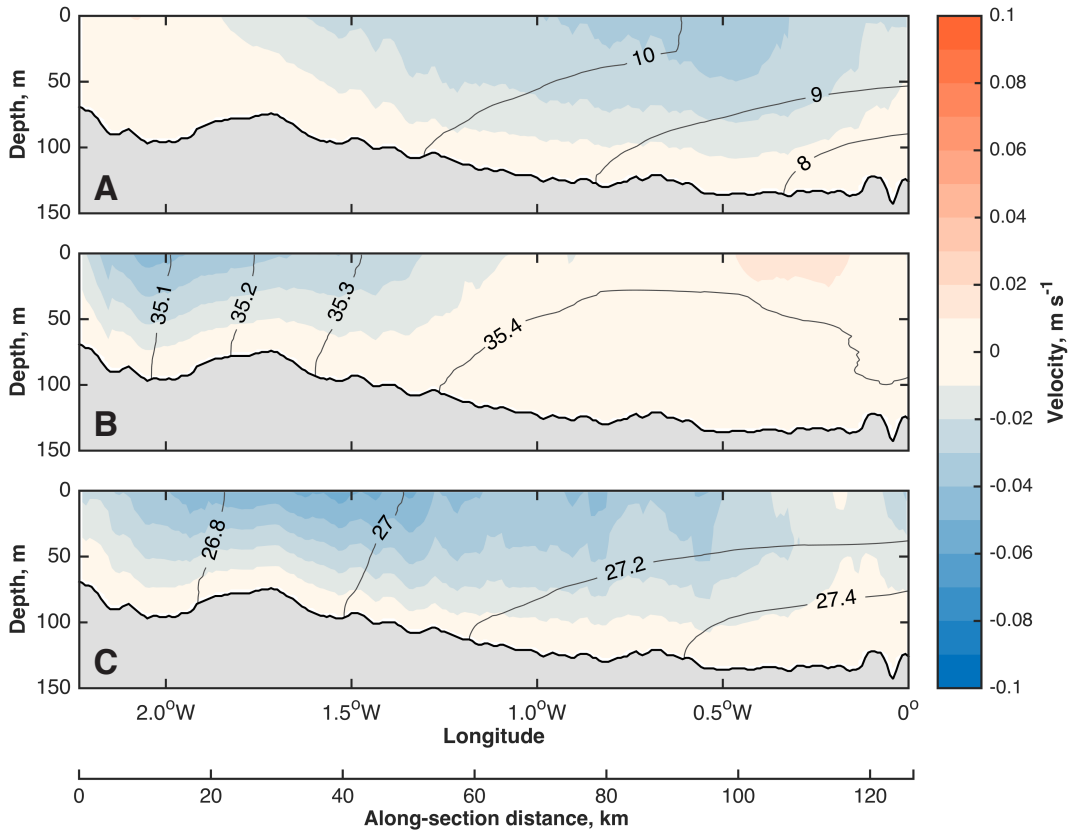

Figure 2.6 Mean conditions in autumn: October, November and December. Panels, shading, contours and units are as in Figure 2.3.

2.4 Amplitude & phase of the annual cycle

High amplitudes ($>$ 2°C) of the annual cycle of temperature (Figure 2.7A) are found in regions that are subject to the greatest degree of warming in the summer: the well-mixed coastal region and the surface in the stratified region. These same regions have higher R^2 values ($>$ 0.8; Figure 2.7B), indicating that the annual cycle explains a greater portion of the observed variability in these regions than it does elsewhere, i.e. in the sub-thermocline region of Atlantic water. Maximum temperatures at the surface and in the mixed regions are reached in August and September (Figure 2.7B). In the stratified region, maximum temperatures are reached progressively later with depth. At the seabed, east of 0.5°W, maximum temperature is not reached until December once stratification has broken down. In this region of Atlantic influence, where annual variability is lowest, the correlation between the derived annual cycle and the observations is at a minimum, indicating that processes other than the annual cycle of air temperature and insolation have a greater impact on the annual cycle of temperature here than they do elsewhere in the section. The annual cycle of temperature provides a statistically significant fit to the observations at all longitudes and depths of the JONSIS section. The strength of this fit is also reflected in the high degree of qualitative similarity between the

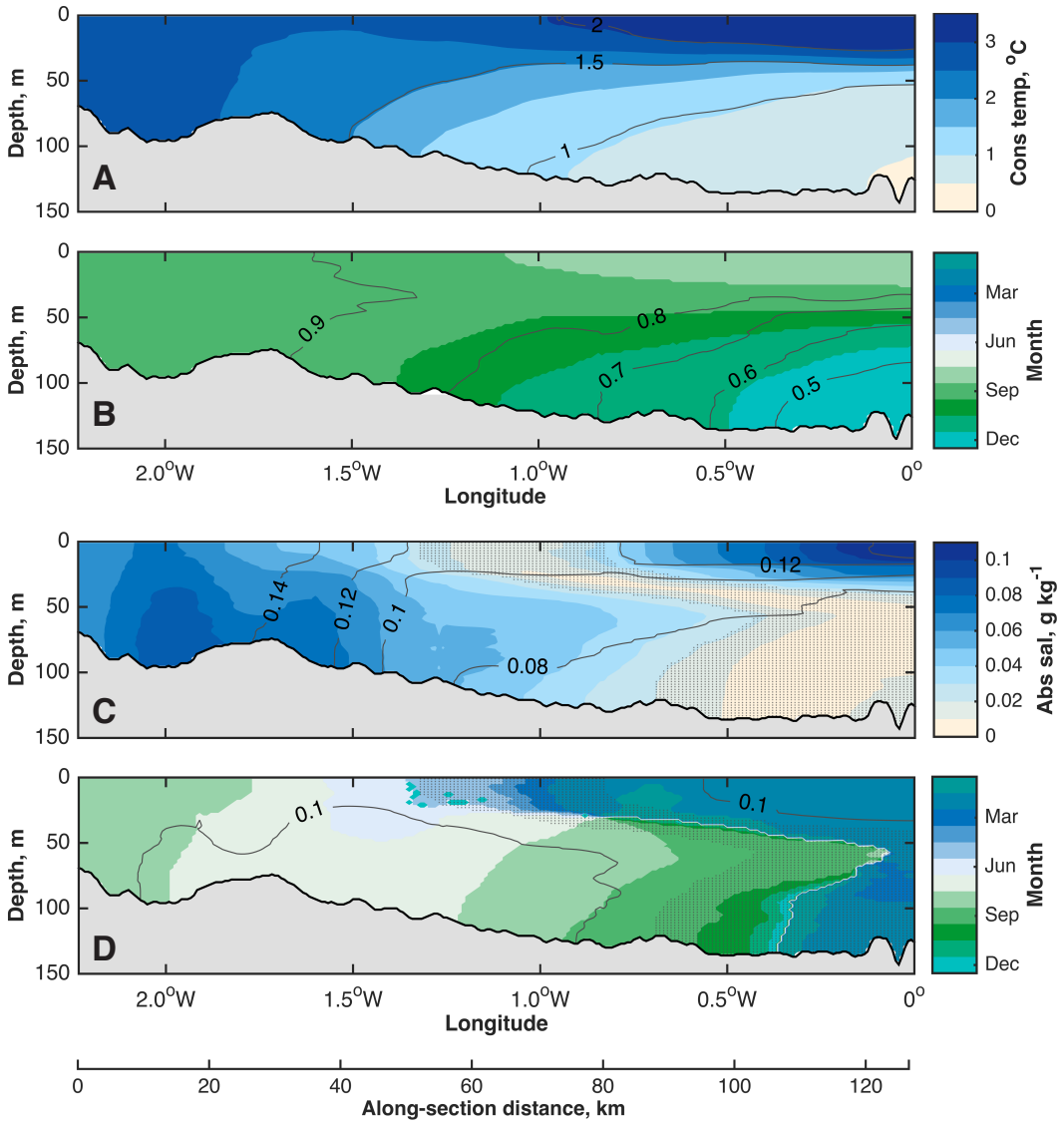

Figure 2.7 **A** Amplitude of the annual cycle of conservative temperature (shading; °C) and standard deviation of conservative temperature (contours; °C). **B** Phase of the annual cycle as month of maximum temperature (shading) and goodness of fit of the annual cycle (R^2; contours). **C** and **D** As A and B but for absolute salinity (g kg^{-1}). Grey dots cover regions where the annual cycle does not provide a statistically significant fit to the observations at the 5% significance level (i.e. $p > 0.05$).

distribution of the standard deviation of temperature and of the amplitude of the annual cycle of temperature (Figure 2.7).

The amplitude of the annual cycle of salinity is highest (> 0.1 g kg^{-1}) at the surface east of 0.2°W (Figure 2.7C) in the region that is most influenced by incursions of NCC water in the summer (Figure 2.5; Sætre et al., 1988). Amplitude is also high (> 0.08 g kg^{-1}) at the seafloor around 2°W. This reflects the changing strength of the horizontal salinity gradient between coastal and Atlantic waters (Dooley, 1974) that occurs over an annual cycle. A horizontal gradient in standard deviation separates the relatively high-amplitude, high-variability region

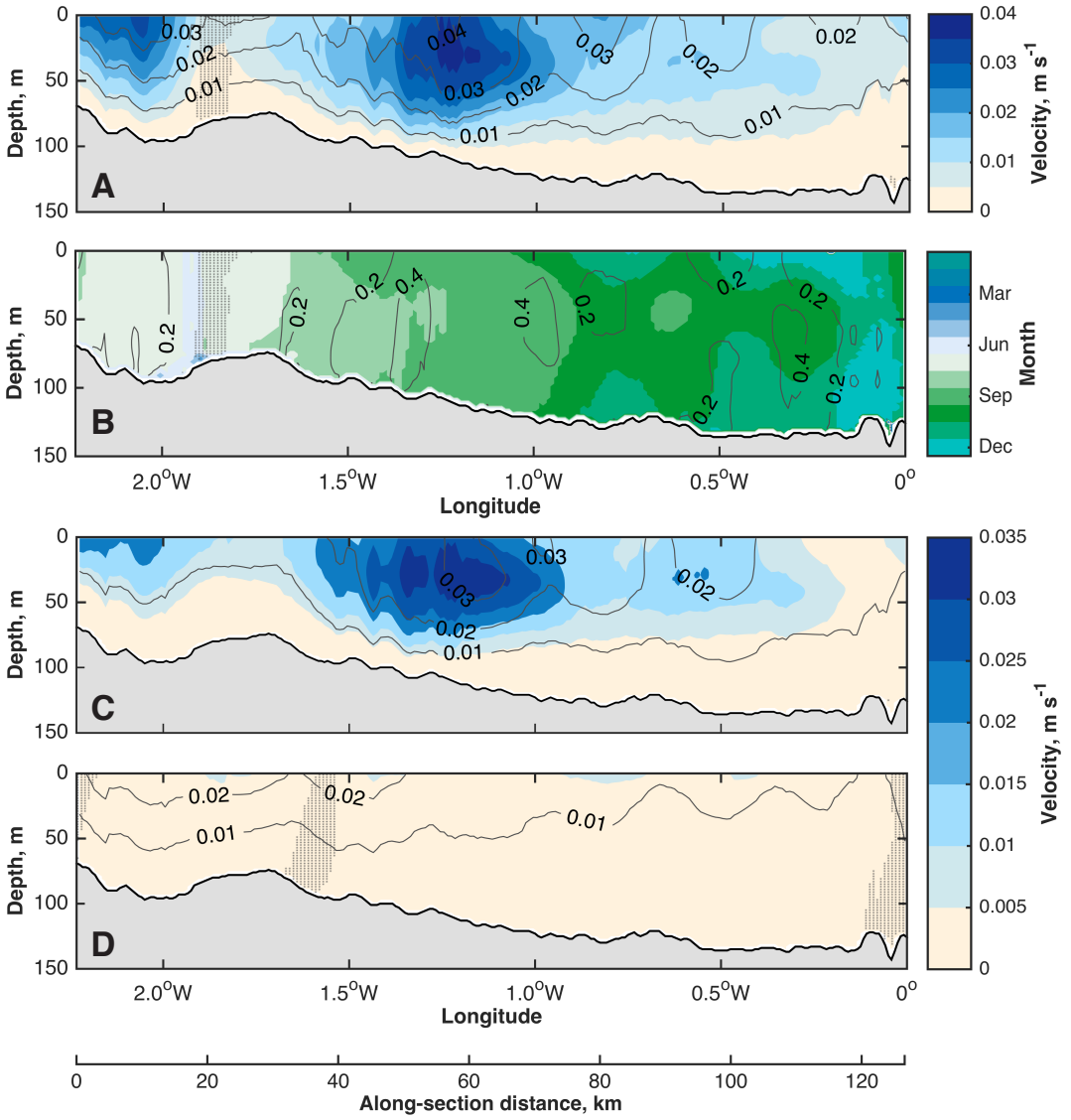

Figure 2.8 Amplitude of the annual cycle of geostrophic velocity (shading; cm s^{-1}) and standard deviation of geostrophic velocity (contours; m s^{-1}). **B** Phase of the annual cycle as month of maximum southward velocity (shading) and goodness of fit of the annual cycle (R^2; contours). **C** Amplitude of the annual cycle of temperature-driven geostrophic velocity (shading; m s^{-1}), and standard deviation of temperature-driven geostrophic velocity (contours; m s^{-1}). **D** As for C, but for the annual cycle of salinity-driven geostrophic velocity. Grey dots cover regions where the annual cycle does not provide a statistically significant fit to the observations at the 5% significance level (i.e. $p > 0.05$).

to the west from the region at depth to the east where salinity is less variable. That contours of standard deviation cross contours of amplitude around 1.5°W indicates that there is salinity variability at the surface that is not explained by the annual cycle. Maximum salinity in the east and west of the section occurs approximately six months out of phase (Figure 2.7D): in the east, it occurs in February; in the west, it occurs in July and August. These results suggests that the amplitude of the annual cycle of salinity is not the same across the JONSIS section and that changes do not happen in phase; this contradicts previous studies based on limited

data (Turrell, 1992). Changes in the strength of the salinity-driven geostrophic flow from month to month, although small, occur as a result of zonal differences in the amplitude and phase of the annual cycle of salinity. However, the correlation between the annual cycle and the observations is low (Figure 2.7D), indicating that the annual cycle presented here explains only a small part (around 10%) of the observed variability. The correlation is strongest in the region of NCC influence to the east of the JONSIS section, which is likely explained by the strong influence that the lateral extent of this low-salinity water is known to have on the salinity of the northeastern North Sea (Marsh et al., 2017). In regions where the annual cycle of salinity is of low amplitude, the annual cycle does not provide a statistically significant fit to the observations at the 5% significance level.

The annual cycle of geostrophic velocity has two regions of high amplitude (> 0.02 m s^{-1}; Figure 2.8A): the first west of 2°W, and the second centred at 1.2°W. The region of low variability in between is where annual mean geostrophic velocity (not shown) is highest: this is the location of the most persistent flow over an annual cycle. Both high-amplitude regions are caused more by the annual cycle of the temperature-driven flow than by that of the salinity-driven flow, which is the less variable of the two (Figure 2.8C and 2.8D). The temperature-driven flow is near negligible in winter but reaches speeds of over 0.05 m s^{-1} in summer; consequently, regions where the greatest temperature-driven velocity is observed in summer are regions where the amplitude of the annual cycle of temperature-driven velocity is high. In contrast, the core of the salinity-driven flow is present throughout the year (Figures 2.3 to 2.6). It is therefore the annual cycle of the temperature-driven flow that is the greater determinant of the annual cycle of the overall geostrophic flow.

The month of the velocity maximum becomes progressively later in the year with distance east along the JONSIS section (Figure 2.8B). West of 1.6°W, maximum velocity is reached in July when the temperature- and salinity-driven components combine to produce a fast (0.08 m s^{-1}) flow. As temperature takes over as the principal driver of the geostrophic flow later in the year, the month of the velocity maximum shifts gradually eastwards as the location of the horizontal temperature gradient moves eastwards. In parts of the eastern limit of the section, maximum velocity does not occur until December. The annual cycle of geostrophic velocity and of the temperature- and salinity-driven components of geostrophic velocity provides a statistically significant fit to the observations in all but small parts of the JONSIS section (Figure 2.8).

2.5 Transport of the Atlantic inflow

Volume transport calculated from the bottom-referenced geostrophic shear across the JONSIS section (Figure 2.9) is lowest in February (0.11 Sv) and highest in October (0.36 Sv). Surface velocity is highest in September, peaking at over 0.09 m s^{-1}; in October, maximum

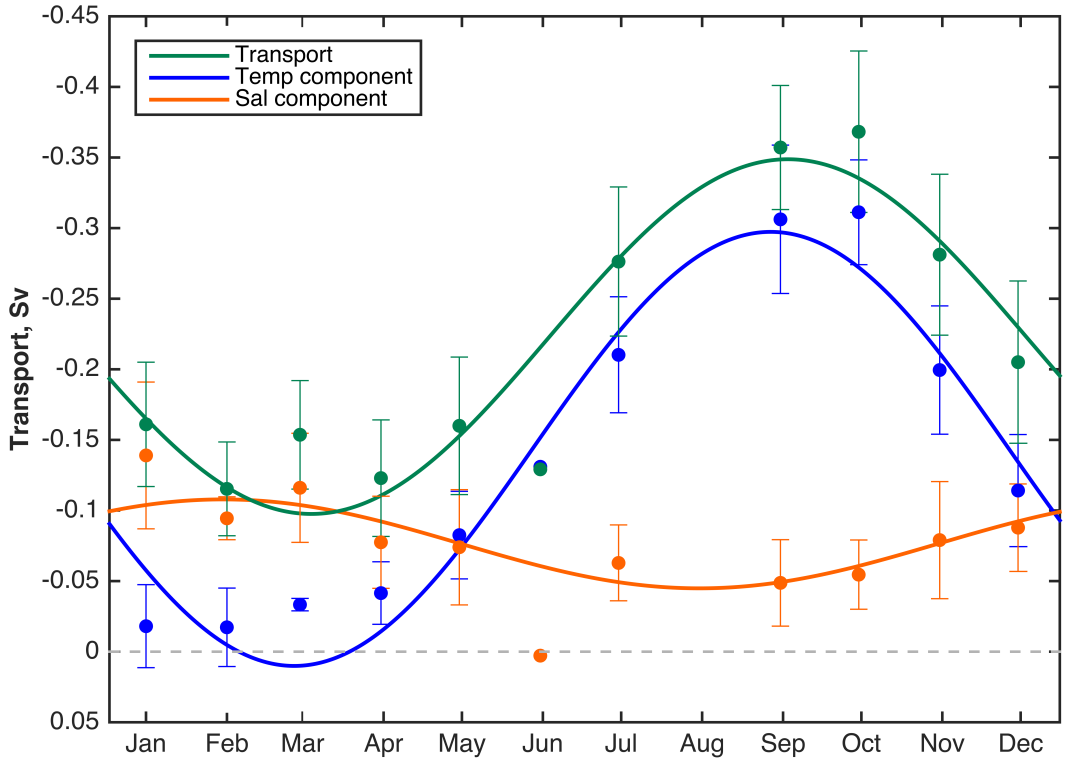

Figure 2.9 **Green** Thermohaline volume transport (Sv) across the JONSIS section over an annual cycle. **Blue** The temperature-dependent component of transport (Sv). **Orange** The salinity-dependent component of transport (Sv). Dots indicate monthly mean values, with error bars representing plus/minus one standard deviation; lines indicate the annual cycle derived from harmonic analysis. No error bars are drawn for June because only one occupation is available for that month. Note that the y axis has been reversed. Negative transport indicates southward flow.

velocity is lower (0.07 m s^{-1}) than in September, but the flow is broader, offsetting the decline in velocity. The same is true of the temperature-driven transport: velocity peaks in September, but the broader current in October results in a higher temperature-driven transport. Maximum salinity-driven transport (0.14 Sv) occurs in January, when the salinity-driven flow is broad (approximately 90 km wide) and has a peak speed of approximately 0.05 m s^{-1}. The salinity-driven current reaches its maximum speed in March, but the narrowing of the salinity-driven current between January and March offsets the increase in transport that the increase in velocity would otherwise cause.

The derived annual cycles of transport, of temperature-driven transport and of salinity-driven transport are also presented in Figure 2.9. (Note that the derived annual cycles are calculated from the complete time series and not from the monthly means plotted in Figure 2.9.) The derived annual cycle of transport explains 71.3% of variability in transport; the derived annual cycle of temperature-driven transport explains 86.0% of variability in the temperature-driven transport; and the derived annual cycle of salinity-driven transport explains 22.5% of variability in salinity-driven transport. The comparatively little variability in salinity-driven transport that is explained by its derived annual cycle suggests that, unlike the temperature-driven

transport, the salinity-driven transport and the salinity distribution that drives it are not principally controlled by seasonally varying processes. All three derived annual cycles provide a statistically significant fit to the observations at the 1% level (i.e. $p < 0.01$). However, some features of the monthly mean transports are not accurately represented by the derived annual cycles. The derived cycles greatly underestimate transport and temperature-driven transport in March, the derived cycles being more than one standard deviation away from the respective monthly mean value in both cases. In the case of temperature-driven transport, the derived annual cycle predicts a positive (i.e. northward) transport between February and April, which is unrealistic given the monthly mean values. The addition of higher harmonics, for instance, the addition of a semi-annual cycle, was not found to make an appreciable difference to the results.

The annual cycle of transport is governed primarily by the annual cycle of the temperature-driven component. The greater amplitude of the cycle of temperature-driven transport compared with that of the salinity-driven transport, as well as the low proportion of the salinity-driven transport that is explained by its annual cycle, ensures that the annual cycle of transport most closely follows that of its temperature-driven component. Salinity-driven transport, while amplifying the temperature-driven transport throughout the year, nevertheless becomes the principal driver of thermohaline flow between January and May, maintaining a thermohaline forcing of the Atlantic inflow at a time when horizontal temperature gradients are almost negligible.

The monthly mean transport results presented above are in broad agreement with those of Turrell et al. (1990), which were derived from current meters. They estimate a non-wind-driven transport of 0.3 – 0.4 Sv in the FIC for periods of low wind speed (< 2 m s^{-1}) during October 1987; non-wind-driven transport reduced to 0.2 – 0.3 Sv in November of that year, and then to below 0.1 Sv in December. It is encouraging that estimates from current meters and hydrographic measurements yield similar results. When compared with the modelled estimates of total (i.e. wind- and non-wind-driven) transport presented by Winther and Johannessen (2006), the largest discrepancies (up to approximately 1 Sv) between non-wind-driven transport and total transport occur between December and March, a time when this study finds the former to be at a minimum and when wind-forcing is known to de dominant. In July and September, when density-forcing is dominant, the results of Winther and Johannessen (2006) suggest that wind-driven transport accounts for up to 0.1 and 0.4 Sv respectively. However, the time series presented by Damm et al. (1994) of transport through the Fair Isle Gap tends to vary between approximately 0.3 and 0.6 Sv in summer and winter respectively. Consequently, these results, together with those of the present study, imply a wind-driven transport of approximately 0.5 Sv in summer and a transport of 0.1 Sv out of the North Sea in winter. That wind forcing could drive a transport out of the North Sea in summer has been suggested by Winther and Johannessen (2006).

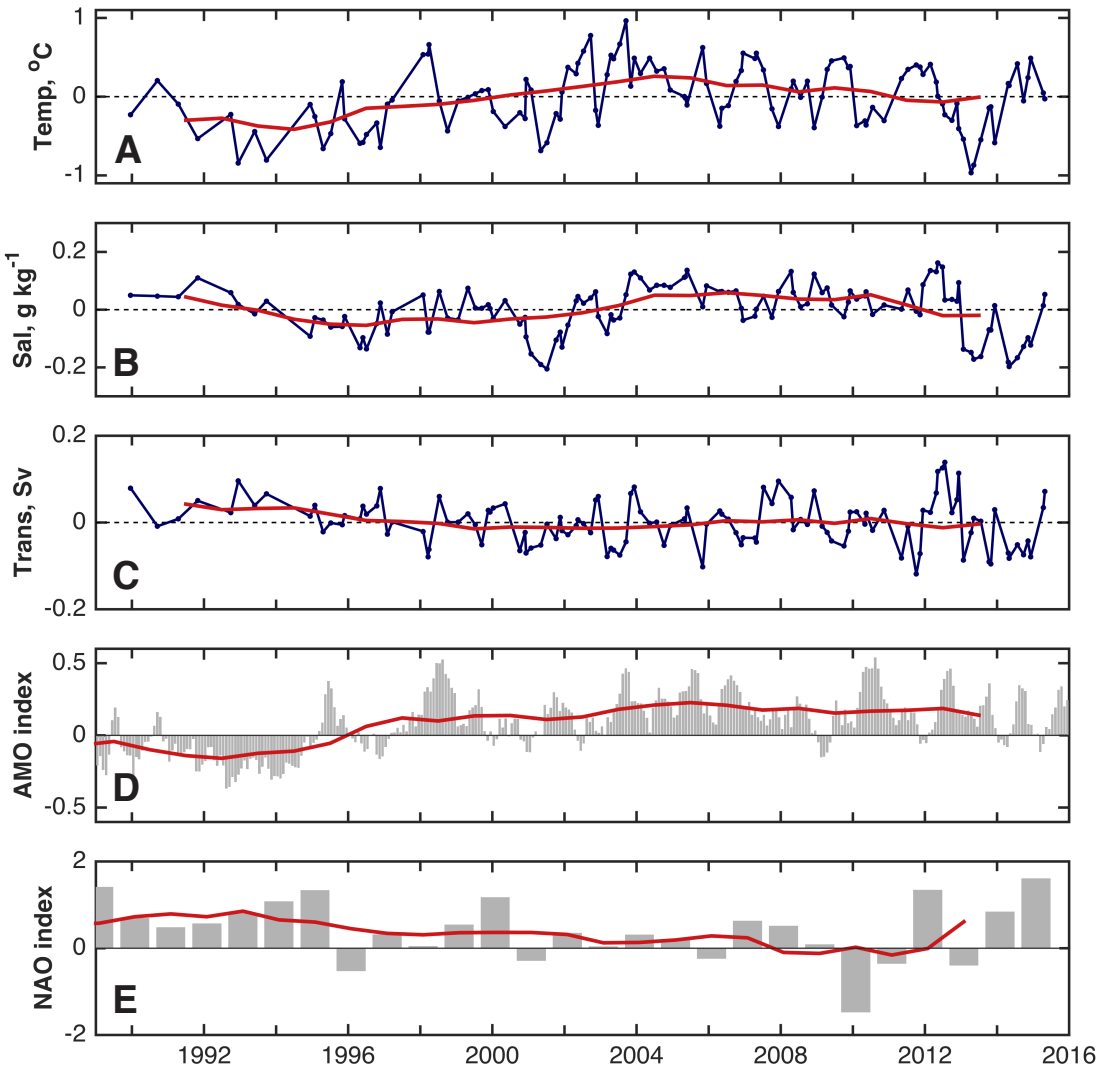

Figure 2.10 Time series of occupation-mean de-seasoned conservative temperature (**A**; °C), absolute salinity (**B**; g kg^{-1}) and geostrophic volume transport (**C**; Sv) as an anomaly from the time-series mean (blue lines in each plot). Negative transport indicates southward flow. **D** Monthly AMO index (grey bars). **E** Mean winter NAO index (grey bars). In all panels, the red line is the five-year running mean.

2.6 Interannual variability

Occupation-mean de-seasoned temperature and salinity (derived as discussed in Section 2.2) at the JONSIS section exhibit coherent interannual variability (Figure 2.10A and B). Occupation-mean temperature and salinity vary in phase. They are below their respective time-series means during the 1990s; values peak in the mid-2000s before falling again towards the present day. There is no appreciable trend in de-seasoned volume transport (Figure 2.10C). Interannual variability of de-seasoned salinity in the coastal waters to the west of the section is more pronounced than in the higher-salinity waters to the east of the section; however, the long-term trends in both regions are qualitatively similar to the trend calculated over the entire JONSIS

section, so they are not considered separately.

Interannual variability in occupation-mean de-seasoned temperature and salinity is positively correlated with the AMO (Figure 2.10D). Positive values of the AMO indicate anomalously warm conditions; negative values of the AMO index indicate anomalously cool conditions. With a five-year smoothing applied (i.e. the red lines in Figure 2.10), variability in the AMO index explains 79.7% and 8.0% of variability in occupation-mean de-seasoned temperature and salinity respectively.

Interannual variability in occupation-mean de-seasoned temperature and salinity is negatively correlated with the NAO (Figure 2.10E). The NAO is one of the key drivers of variability in the climate of the northern hemisphere (Hurrell et al., 2003) and has a strong influence on North Sea inflows (Winther and Johannessen, 2006). Only the average winter index has been considered as the NAO explains more climate variability in winter than in summer (Hurrell, 2009). With a five-year smoothing applied, variability in the NAO index explains 49.95% and 13.20% of variability in occupation-mean de-seasoned temperature and salinity respectively. The slopes of the regression lines associated with the temperature correlations (i.e. AMO and NAO) are significantly different from zero at the 5% significance level (i.e. $p < 0.05$). The regression lines associated with the salinity correlations are not statistically significant. The significance of the correlations is calculated once auto-correlation of the time series has been accounted for. Autocorrelation is a potential feature of a time series in which individual observations are not truly independent: an observation taken at time t is to some degree influenced by observations that fall within the time $t - \lambda$, and itself influences observations taken within the time $i + \lambda$, where λ is a time lag. For example, the annual cycle of solar heating is such that sea-surface temperature in July is not wholly independent of sea-surface temperature in either June or August. The degree of autocorrelation may be described by the time lag, λ, that must elapse before the influence of an observation is no longer felt on subsequent observations. Autocorrelation reduces the degrees of freedom in a time series, and so increases the threshold for statistical significance in a correlation with a second time series.

A positive AMO and a negative NAO are generally associated with a warm, salty inflow; a negative AMO and a positive NAO are generally associated with a cool, fresh inflow (Figure 2.10). The link between the NAO and Atlantic inflow would likely be stronger if the wind-driven flow were included. While the NAO is thought to affect inflows to the North Sea via water mass exchange, this is secondary to the control that it exerts on the wind-driven circulation (Sündermann and Pohlmann, 2011).

Marsh et al. (2017) hypothesise a strong link between Atlantic inflow into the North Sea and the salinity of the North Sea on interannual time scales. In a hindcast model simulation, they report a decline in the transport of water from the European Shelf Edge Current to the North Sea between the early 1990s and the mid-2000s, a likely consequence of the transition from a positive to a neutral NAO over the same period; in their simulation, however, this coincides with a freshening in the northern North Sea that does not appear to agree with the long-

term observations presented here. Furthermore, Hjøllo et al. (2009) find that salinity in the approximate region of the JONSIS section cannot be accurately reproduced by forcing which does not include conditions in the northern Atlantic subpolar gyre; they also link a weaker circulation in the subpolar gyre to higher salinities in the northern North Sea. This suggests that the observed correlation between the NAO, AMO and mean temperature in the Atlantic inflow may be explained at least in part by large-scale variability in the circulation of the northern Atlantic that occurs in response to changes in the NAO and AMO. The influence of these indices on salinity appears to be less certain, perhaps because salinity may also be affected by, for example, interannual variability in run off into the source waters of the FIC to the west of Scotland.

2.7 Summary

Atlantic inflow is a key control on the hydrography and ecology of the northern North Sea. Data from 27 years of occupations of the JONSIS section, a zonal hydrographic section in the northern North Sea that crosses the path of the inflow, have been analysed to describe and quantify the annual cycles of temperature, salinity and bottom-referenced geostrophic velocity. A horizontal gradient between low-salinity water near the Scottish coast and high-salinity water at depth offshore is present throughout the year. This gradient gives rise to a salinity-driven flow, the strength and location of which changes with the strength and location of the horizontal salinity gradient. The transport associated with this salinity-driven flow is stronger in winter than in summer.

There are pronounced changes in the temperature distribution over an annual cycle. Near negligible thermal gradients exist in the winter, both horizontally and vertically. In the summer a strong thermocline develops offshore in response to surface warming; however, in the shallower water close to the coast, tidal currents ensure that the water column remains fully mixed throughout the year, even when offshore waters are stratified. The growth and subsequent decay of the horizontal thermal gradient between the stratified and mixed regions give rise to a temperature-driven flow that is strongly seasonal: in the winter, very little temperature-driven flow occurs; in summer, a broad and relatively fast temperature-driven flow occurs. The transport associated with this temperature-driven flow is greater than that associated with the salinity-driven flow: the annual cycle of transport of the geostrophic shear is therefore influenced primarily by that of its temperature-driven component, being much greater in the summer than in the winter. The effect of the salinity-driven component is to maintain appreciable non-wind-driven inflow during the winter, during which season Atlantic inflow is known to be a principally wind-driven.

Occupation-mean de-seasoned temperature and salinity exhibit interannual variability, rising from anomalously low to anomalously high values between the early 1990s and the mid-2000s

before declining towards the respective time-series mean value by the early 2010s. In the case of temperature, the correlation with the AMO index and the anti-correlation with the NAO index are statistically significant at the 1% level.

Future work would benefit from data with higher spatial resolution in order that the often sharp vertical and horizontal gradients be better resolved. Hydrographic observations from June and August would fill in gaps in the data and would enable us to better constrain the derived annual cycles of temperature, salinity and transport during these months. Sustained observations of the wind-driven component of the flow would permit a truly comprehensive description of Atlantic inflow into the northern North Sea over an annual cycle.

These results provide a description of the density forcing of a shelf-sea current in a tidally energetic environment, accounting in detail for the influence of both temperature and salinity. The use of a 27-year-long time series allows for the calculation of robust averages and annual cycles that provide a statistically significant fit to the observations. It is hoped that these results will provide a useful background to further studies of the northern North Sea.

Chapter 3

Shelf sea tidal currents and mixing fronts determined from ocean glider observations

3.1 Introduction

Tides are of fundamental importance for understanding shelf sea dynamics and ecosystems. Not only are tidal currents frequently the dominant flows in these regions (Otto et al., 1990), the turbulence, bottom-mixing and circulation patterns to which they give rise have a profound effect on the physics, biogeochemistry and ecology of shelf seas (Simpson and Hunter, 1974; Lenhart et al., 1995; Holt and Umlauf, 2008). In shallow regions with fast tidal currents, full-depth mixing is maintained throughout the year. In deeper regions, or where tidal currents are slower, tidal mixing cannot overcome buoyancy forcing in summer and the water column stratifies seasonally. The boundaries between mixed and stratified areas are sharp ($\sim$20 km; Hill et al., 2008) and are known as tidal mixing fronts. These fronts separate water masses with markedly different physical and biogeochemical properties, and the density-driven jets to which they give rise are important transport pathways (Hill et al., 2008). Consequently, understanding the processes that control the formation and location of tidal mixing fronts, alongside an accurate knowledge of the tidal currents themselves, is necessary for effective management of economically important shelf sea ecosystems and for modelling the dispersion of tracers, contaminants and organisms.

Simpson and Hunter (1974) predict the location of tidal mixing fronts by considering surface heat fluxes and tidal stirring. They assume that surface heating is spatially uniform over the northwestern European continental shelf, and exclude wind mixing and residual currents, to propose that tidal mixing fronts may be found at a critical value of h/u^3, where h is the water

depth and u is the amplitude of the M_2 tidal speed. We refer to this as the heating-stirring theory. No consideration is given to the influence of salinity and non-tidal flows. Subsequent studies have confirmed the validity of this theory and the utility of the h/u^3 parameter (Garrett et al., 1978; Pingree and Griffiths, 1978; Simpson and Bowers, 1981; Bowers and Simpson, 1987). The critical value on the northwestern European shelf is $log(h/u^3) = 2.7 \pm 0.4$ (Simpson and Sharples, 1994). Later contributions added that frontal location may be expected to move as maximum tidal speeds vary over the spring-neap cycle (Simpson and Bowers, 1981; Loder and Greenberg, 1986). The local heating-stirring balance is not, however, the only control on frontal location. Salinity has been found to influence frontal location and movement in Regions of Freshwater Influence (ROFI; Hopkins and Polton, 2012), and ice melt water has been found to be an important component of frontal systems in the high latitudes (Schumacher et al., 1979). Furthermore, tidal straining – i.e. the shearing of the density field by the tide – can lead to a semidiurnal mixing-stratification cycle that can influence both tidal and residual circulation (Souza and Simpson, 1996; Verspecht et al., 2009; Palmer, 2010). Salinity is of clear importance in frontal dynamics, but its effect other than in ROFIs – for instance, in deeper shelf-sea regions where horizontal salinity gradients are less pronounced and in regions with a complex water mass distribution – has been less thoroughly investigated.

A meridional front, co-located with the path of the Fair Isle Current (FIC; Figure 1.1) is present in the northwestern North Sea to the west of 1°W (Chapter 2; Turrell et al., 1996). The front is bottom-intensified and frequently has only a limited surface signature (Chapter 2; Hughes, 2014). Consequently, the front may be more readily observed from sub-surface observations collected from a ship or a profiling glider than in satellite observations of sea-surface temperature. The region, which is influenced by cool (< 9°C), saline (> 35.4 g kg^{-1}) water found to the east of the front (Chapter 2; Hill et al., 2008), is characterised by features excluded from the heating-stirring theory: coastal and oceanic water masses flow south into the North Sea, introducing temperature and salinity gradients that are not a consequence of heating-stirring interactions (Turrell, 1992; Hill et al., 2008; Sheehan et al., 2017), and a generally southward residual current persists throughout the year (Dooley, 1974; Turrell, 1992; Winther and Johannessen, 2006). Nevertheless, it is thought that the location of the front is at least partially influenced by the local heating-stirring balance, with tidal stirring being responsible for maintaining fully mixed conditions west of the front (Svendsen et al., 1991). The hydrographic setting of this front means that its behaviour may be different from fronts where the influence of the open ocean is less pronounced.

We use high-resolution hydrographic and dive-average current (DAC) observations from a profiling ocean glider that repeatedly crossed this front to quantify tidal flows in the vicinity of the front. The DAC time series is used to accurately determine the velocities of the M_2 and S_2 tidal constituents at the time and location of each glider dive without recourse to a tide model. DAC observations are known to be accurate to within a few cm s^{-1} (Merckelbach et al., 2008), and a glider's speed through water can be determined with sufficient accuracy for gliders to

measure, for example, fine-scale turbulence (e.g. Beaird et al., 2012; Fer et al., 2014). In this study, we augment this capability by demonstrating that individual DAC observations may be accurately separated into tidal and residual components. We then use these glider-derived tidal velocities, together with the output of a simple model, to investigate the influence of tidal and non-tidal processes on the location of the mixing front. The high spatial resolution of glider observations permits a more accurate estimate of frontal location than is possible from ship-based observations (e.g. Schumacher et al., 1979; Hill et al., 1997; Sheehan et al., 2017). The method for calculating tidal velocities from DAC observations, outlined in Section 3.2, is a key result of the work with potential applications beyond that presented in Section 3.3.

3.2 Glider-derived tidal velocities

3.2.1 Method

Between 12th October and 1st December 2013, the glider (Seaglider 502; Eriksen et al., 2001) completed 10 partial occupations of the Joint North Sea Information System (JONSIS) hydrographic section (Turrell et al., 1996; Berx et al., 2018). Occupations took between three and 11 days, depending on how much of the section was sampled. The 127 km-long section, between 2.23°W and the prime meridian at 59.28°N (Figure 1.1), crosses the combined path of the two western Atlantic inflows into the northwestern North Sea: the FIC and the East Shetland Atlantic Inflow (ESAI; Figure 1.1; Turrell et al., 1996). Bathymetry along the section varies between 69 and 143 m, deepening eastward. All bathymetric data used in this study were extracted from the GEBCO dataset[1] (resolution 30 arc-seconds). While it is possible to estimate bathymetry from the glider's altimeter observations, we believe that bathymetry from a databank for a well-studied region such as the North Sea is likely more accurate. Glider dives were, on average, 20 minutes and 300 m apart; as one dive comprises two profiles, profiles are therefore an average of 150 m apart. Most dives sampled the full water column. DAC observations are obtained incidentally during a glider's flight as the glider is advected by the flow over the duration of a dive-climb cycle. On surfacing, the glider compares its actual, GPS-determined position with its position as estimated by dead-reckoning; the difference is attributed to advection by the DAC (Eriksen et al., 2001; Merckelbach et al., 2008). The accuracy of DAC observations was improved post-deployment by optimising the hydrodynamic model of the glider's flight (Frajka-Williams et al., 2011) using the UEA Glider Toolbox[2] (Queste, 2013). No compass calibration dive was performed during the deployment, so the directional and magnitude uncertainty introduced to the DAC estimates by compass error cannot be quantified. Compass miscalibration would, in the case of no actual DAC, introduce an erroneous DAC estimate due to the glider's inability to know its actual location. Errors and uncertainties

[1] GEBCO_08 grid, version 20100927, www.gebco.net
[2] www.bitbucket.org/bastienqueste/uea-seaglider-toolbox

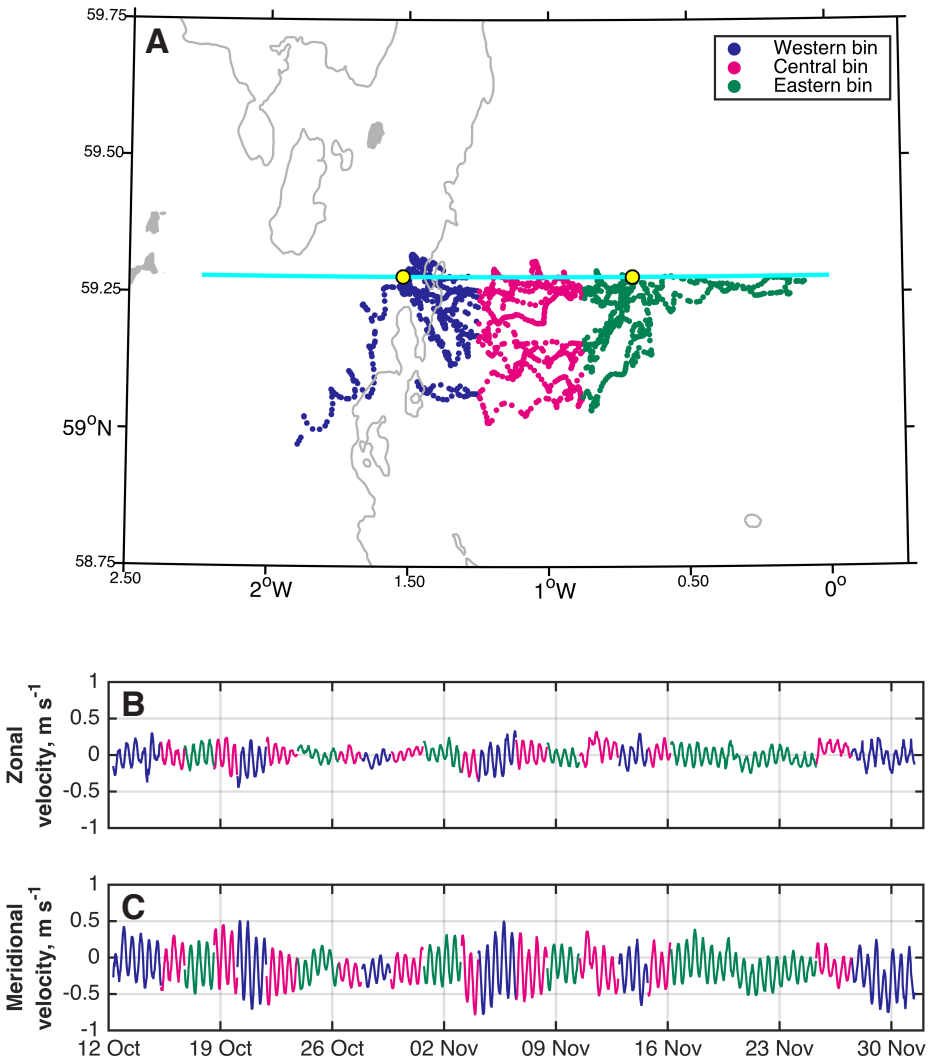

Figure 3.1 **A** The location of glider dives along the JONSIS section (cyan line), with dives coloured by longitudinal bin (see legend in panel A). The location of the current meters is shown by the yellow dots. The 100 m isobath is shown in grey. **B** Zonal and **C** meridional DAC velocities, coloured by bin (same colour scheme as panel A).

in the calculation of the flight model will also add uncertainty to DAC estimates.

DAC velocities were divided into three longitudinal bins along the JONSIS section (Figure 3.1A), the boundaries being chosen such that each bin contained an approximately equal number of dives: 502 in the eastern bin, 514 in the central bin and 503 in the western bin. Binned velocities were treated as three discontinuous time series (Figure 3.1B and C). At the central longitude of each bin, the amplitude and phase of the M_2 and S_2 tidal constituents were determined using harmonic analysis (Thomson and Emery, 2014). These results were used to construct tidal ellipses along the JONSIS section (Figure 3.2). Combined M_2 and S_2 (hereafter denoted M_2+S_2) zonal and meridional velocities were then calculated at the time of each glider dive. Finally, tidal velocity was linearly interpolated onto that dive's longitude to construct a time series of tidal velocity along the glider's overground track – that is, a time series of tidal

velocities with data points at the time and location of each dive (Figure 3.1A). These are hereafter referred to as along-track velocities (Figure 3.3). Nearest-neighbour extrapolation was used for dives to the east and west of the three bins; extrapolation is necessary because some dives lie to the east and west of the central points of the eastern and western bins respectively.

The accuracy of the glider-derived ellipses, and consequently of the derived tidal currents, is dependent on the number of dives that fall within a bin, and the number of bins determines the number of points along the section at which the tide may be resolved. There is therefore a trade off between the number of constituents that can be resolved in the harmonic analysis and the spatial resolution. For a regularly spaced, continuous time series, the Rayleigh criterion ($\Delta f = 1/T$, where Δf is the difference in frequency between two constituents, and T is the length of the time series) dictates the minimum length of time series needed to separately resolve constituents of different frequencies. To resolve the M_2 and S_2 constituents from a combined signal, a time series of at least 14.8 days is needed: that is, the cycle introduced into tidal signals by the interaction of the M_2 and S_2 constituents, known as the spring-neap cycle. The Rayleigh criterion is harder to apply to a time series of irregularly spaced DAC, particularly when temporal discontinuities are introduced by the binning process (Figure 3.1). Instead, setting the limits of each bin such that an equal number of dives falls in each ensures that amplitude and phase estimates are of a comparable accuracy across the section. The cumulative length of time that the glider spends in each bin is 14.6, 17.1 and 17.7 days for the western, central and eastern bin respectively, which is approximately equal to, or greater than, the minimum length of time needed to separately resolve the M_2 and S_2 constituents in a regularly spaced, continuous time series. Separating the time series into four or more bins necessarily reduces the number of dives and the length of time the glider spends in each bin. Using four or more bins resulted in S_2 ellipses with unrealistic amplitudes and inclinations, suggesting an inadequate resolution of this weaker constituent.

Two current meters were deployed on the JONSIS section for a period covering the glider deployment: an Aanderaa Seaguard single-point current meter at a depth of 40 m (1.52°W; Figure 3.1A), and a Nortek AWAC profiling current meter that took measurements in 4 m bins centred from 9 to 89 m below the surface (0.70°W; Figure 3.1A; Berx et al., 2014). Observations from the profiling current meter were depth-averaged for comparison with glider DAC. The amplitude and phase of the M_2 and S_2 tidal constituents were determined from the current meter records using the same harmonic analysis as for the glider data. To compare the results of our method with an established alternative, estimates of M_2 and S_2 amplitude, phase and velocity, were extracted from the TPXO inverse model European shelf solution[3] (1/30° resolution; Egbert et al., 1994; Egbert and Erofeeva, 2002; Egbert et al., 2010) using the Tidal Model Driver software for Matlab[4].

[3] volkov.oce.orst.edu/tides

[4] esr.org/research/polar-tide-models/tmd-software

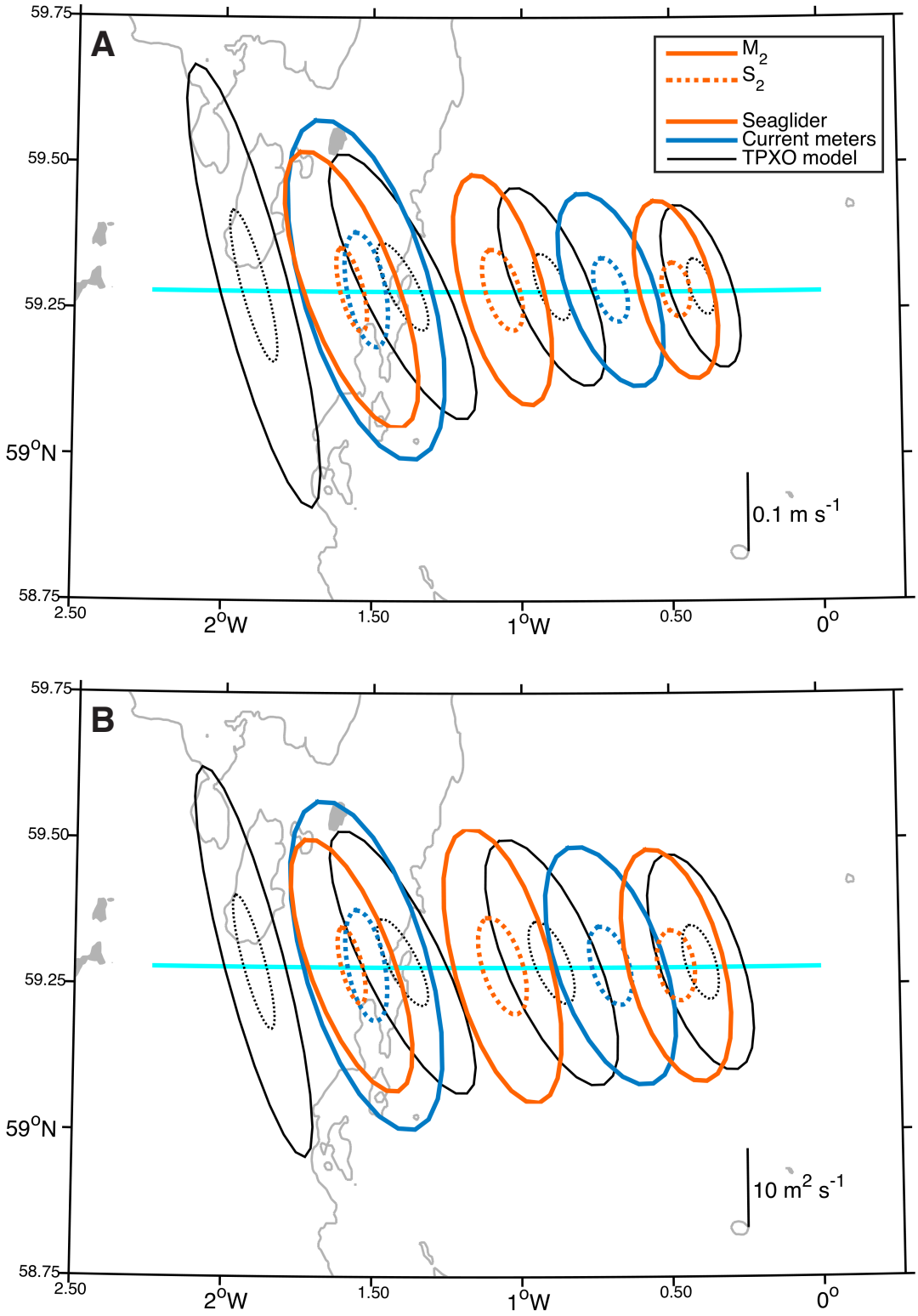

Figure 3.2 **A** Tidal ellipses from glider observations (orange), current meter observations (blue) and the TPXO tide model (every fifth grid point, black). **B** Tidal transport ellipses, with colours as in panel a. In both panels, solid lines are for the M_2 constituent; dotted lines are for the S_2 constituent. The JONSIS section is shown in cyan and the 100 m isobath is shown in grey.

3.2.2 Tidal ellipses

Tidal ellipses of the glider-derived tide show a decrease in the amplitude of zonal and meridional tidal velocity with distance offshore (Figure 3.2A). Semi-major axes are consistently larger than semi-minor axes, and the offshore decrease in the magnitude of the semi-major axes is greater than the offshore decrease in semi-minor axes. The smaller rate of change in the eastern part of the section is because bathymetry gradients are smaller than in the west. Velocity amplitudes were multiplied by the mean water depth in each bin to derive ellipses of tidal transport per unit width (Figure 3.2B). Compared with velocity amplitude, transport amplitude changes less markedly with distance offshore, suggesting that the greater tidal velocities observed in shallow water than in deep water are primarily a result of volume continuity rather than the exponential offshore decay of the tidal Kelvin wave.

Glider velocity ellipses compare well with velocity ellipses from the current meter observations and the TPXO model (Figure 3.2A). Ellipses from the three sources indicate clockwise rotation of the tide. The ellipse from the western, single-point current meter observations (Figure 3.1A and 3.2) is likely larger (i.e. indicating faster tidal velocities) than the depth-mean glider and TPXO ellipses because tidal currents at the depth of this current meter (40 m) are less influenced by bottom friction than are depth-average velocities. Comparing glider ellipses with the TPXO ellipses at the same location, the difference between the M_2 semi-major axes is 0.10 m s^{-1} (25%) in the western bin and 0.01 m s^{-1} in the central and eastern bins (2% and 4% respectively). The difference between the M_2 semi-minor axes is 0.01 m s^{-1} in all three bins ($<$ 1%, 8% and 15% in the western, central and eastern bins respectively). The phases of the M_2 ellipses differ by 10°, 7°and 11° in the western, central and eastern bins respectively. S_2 semi-major axes differ by 0.05 m s^{-1} (44%) in the western bin and by 0.01 m s^{-1} in the central and eastern bins (8% and 9% respectively). S_2 semi-minor axes differ by 0.01 m s^{-1} in all three bins (48%, 18% and 19% in the western, central and eastern bins respectively). The phases of the S_2 ellipses differ by 7°, 2° and 17° in the western, central and eastern bins respectively. Percentage differences between the S_2 ellipses are larger in the western bin because the magnitude of the glider-derived S_2 tide is smaller than in the central and eastern bin. Differences between the ellipses in the western bin could be greater than in the central and eastern bins because the TPXO model is an inversion of satellite altimeter observations, which are less reliable near coastlines (Egbert and Erofeeva, 2002). The glider ellipses are potentially a more accurate characterisation of the tide in this part of the section.

3.2.3 Tidal velocities

To quantify the accuracy of the glider-derived tide (Figure 3.3), the along-track M_2+S_2 velocity time series are compared with the M_2+S_2 along-track time series from the TPXO model sampled at full resolution. Unlike the current meter observations, this model provides estimates of tidal velocity across the entire JONSIS section. The root-mean-square-differences

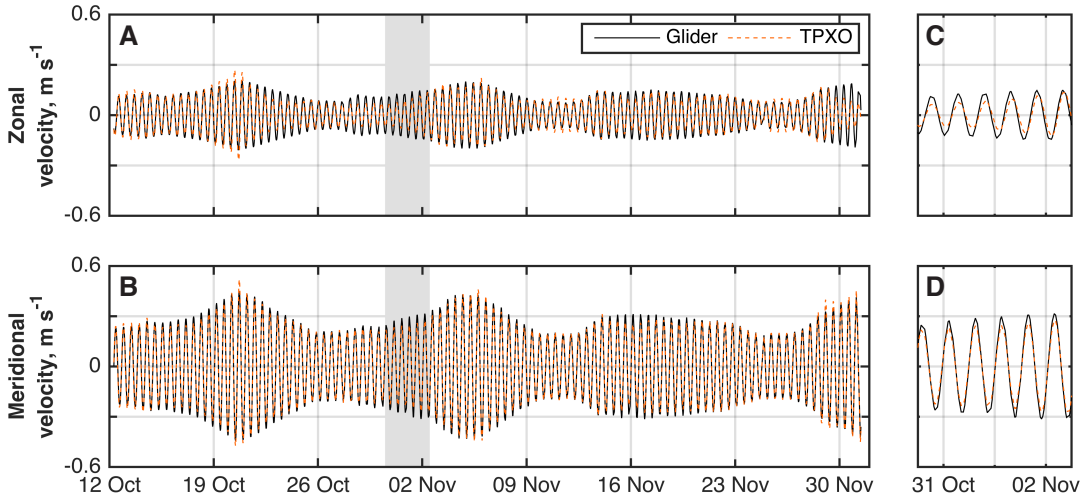

Figure 3.3 **A** Zonal and **B** meridional velocity. **C** and **D** are zoomed-in excerpts of panels A and C respectively. The region shown in panels C and D is marked by the grey box in panels A and B respectively. In all panels, the solid black line is the M_2+S_2 tidal velocity determined from the glider observations and the dashed orange line is the M_2+S_2 tidal velocity from the sub-sampled TPXO model.

(RMSD) between the glider- and the TPXO-derived tides are 0.03 and 0.02 m s^{-1} for the zonal and meridional velocities respectively.

To determine the extent to which the difference between the glider- and TPXO-derived time series may be attributed to the comparatively low resolution of the glider-derived tide, we firstly compare the fully sampled TPXO tide with the TPXO tide sampled at the same locations as the glider-derived tide (i.e. the centre of each of the three bins, Figure 3.1). Velocity time series are extracted from the TPXO model at the central point of each glider bin and at the time of each glider dive. These velocities are interpolated zonally onto the location of each dive, replicating the method used to calculate the glider-derived tide. The RMSDs between the fully and sub-sampled TPXO time series are 0.04 and 0.02 m s^{-1} for the zonal and meridional velocities respectively. Secondly, to simulate a longer glider deployment with more dives from which it would be possible to use smaller spatial bins and so increase spatial resolution, we compare the fully sampled TPXO tide with the TPXO model sub-sampled every 0.5° longitude between 2.5°W and the prime meridian. This decreases the zonal RMSD to 0.03 m s^{-1}; the meridional RMSD remains 0.02 m s^{-1}. The spatial resolution of the glider-derived tide appears to have little influence on the results compared with the output of a high-resolution tide model.

The ability to use glider DAC to estimate along-track tidal velocity to within $\pm$ 0.02 to 0.04 m s^{-1}, even when the tide may be resolved at only a few points along a section, could be of considerable use in regions where tide models are unreliable or unavailable, enhancing the utility of gliders, for example in remote regions such as the Antarctic shelf. In order to use this method on DAC observations from other glider missions, we make the following recommendations:

1. Obtain repeat occupations of the same transect.
2. Set the transect length so as to avoid aliasing the spring-neap cycle – i.e. avoid individual occupations lasting around one or two weeks.
3. Optimise the hydrodynamic model of the glider's flight (Frajka-Williams et al., 2011) to obtain accurate DAC observations.
4. Do not attempt to resolve more constituents than may be accurately resolved given the length of each binned, discontinuous time series.

3.3 Frontal location

We apply the glider-derived tide described in the previous section to study the location of a front in the northwestern North Sea. Specifically, we investigate the extent to which the location of the front may be explained by heating-stirring interactions, a principal component of which is tidal speed. Furthermore, this analysis serves as an illustration of a potential application of the method. We use TEOS-10 variables (IOC et al., 2010) in this analysis.

The location of the front as determined from the glider observations is shown in Figure 3.4. The front is defined to be where the top-bottom temperature difference is 0.5°C. This definition has the advantage of being straightforward to calculate, both from observations and models, and follows the approach used in previous studies (Bowers and Simpson, 1987; Holt and Umlauf, 2008; O'Dea et al., 2012). On a number of crossings of the front, the top-bottom temperature difference equals 0.5°C at several points (Figure 3.4A). This is because the front often covers a zonal distance wider than that between glider dives. Observations of frontal location are not corrected for zonal tidal advection of the front. Instead, we acknowledge a zonal uncertainty in frontal position of $\pm$ 2 km (0.04° longitude), that being the mean zonal tidal displacement during the deployment.

We calculate $log(h/u^3)$ at the time and location of each glider dive. The amplitude of tidal speed used to calculate $log(h/u^3)$, in place of the amplitude of the M_2 tidal speed, is that of the M_2+S_2 constituents; this is to capture changes in tidal speed over the spring-neap cycle. The M_2+S_2 amplitude is derived from the along-track glider-derived tide: we extract a time series of the maximum speed achieved over each tidal cycle (Figure 3.4B, red line) and interpolate this onto the time of each glider dive.

Values of $log(h/u^3)$ at the front vary considerably over time (Figure 3.4A), from below 3 around 21st October to over 4 around 12th November. Some of this range may likely be attributed to the width of the front, which can cover a range of values of $log(h/u^3)$ at this high spatial and temporal resolution (Hughes, 2014). Often, the frontal value of $log(h/u^3)$ lies outside the range 2.7 $\pm$ 0.4 typically used as the critical value for the northwestern European shelf region (Simpson and Sharples, 1994). However, our modified definition of the amplitude of tidal speed (i.e. M_2+S_2) precludes direct comparison of our values of $log(h/u^3)$ with those

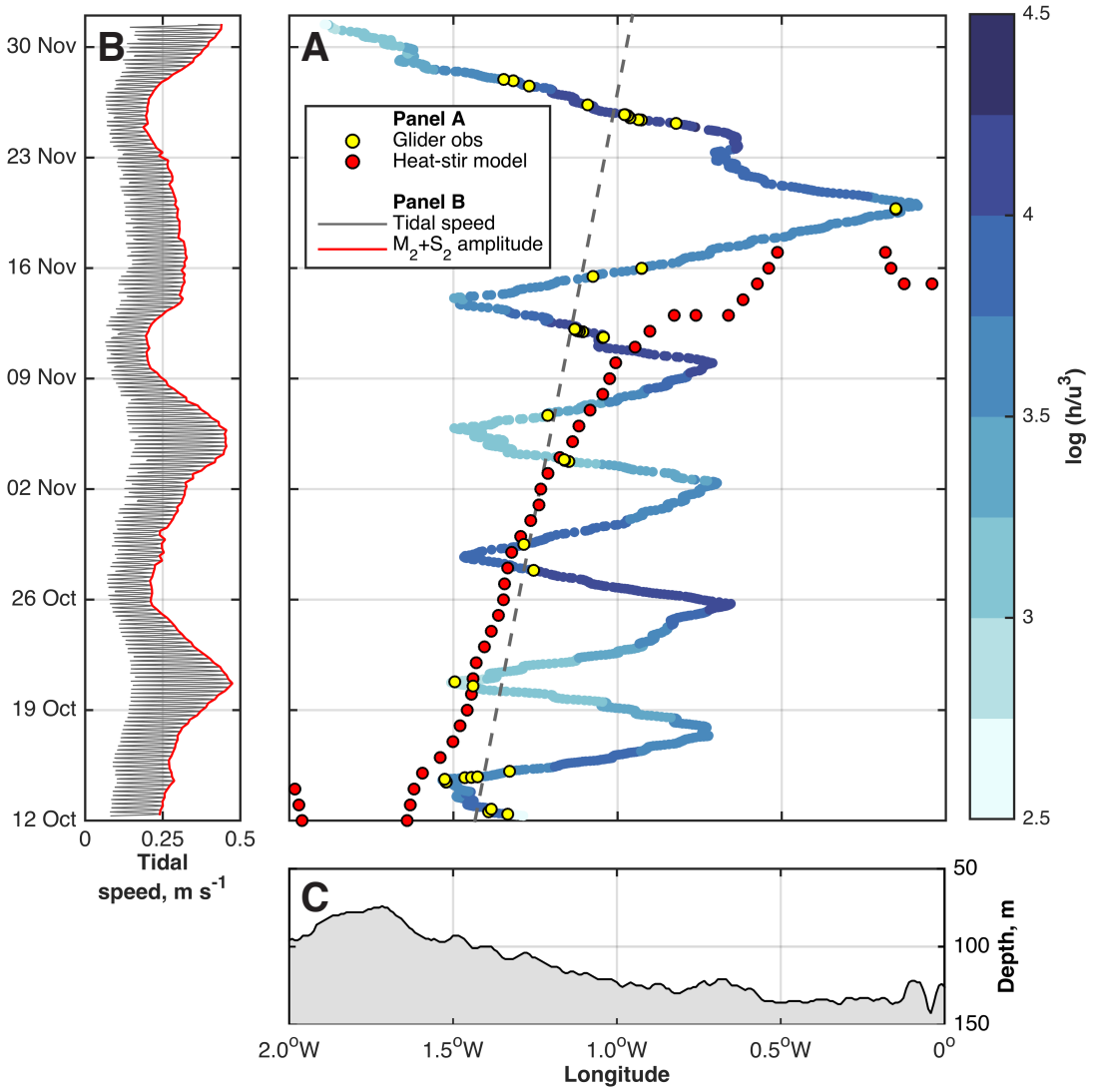

Figure 3.4 **A** Hovmöller plot of $log(h/u^3)$ (colour scale) from glider observations. Yellow circles mark the observed locations of the front. The dashed grey line is the line-of-best-fit through these points. Red circles mark the location of the front as modelled by the heating-stirring model. **B** M_2+S_2 tidal speed (m s^{-1}; grey line) at the location of each glider dive as calculated using the glider-derived tidal velocities. The red line joins up the maximum speeds and is the estimate of tidal velocity amplitude, u, used to calculate $log(h/u^3)$ in panel A. **C** Bathymetry (m) along the JONSIS section – i.e. h in $log(h/u^3)$.

previously published. Using only the M_2 tidal speed allows comparison with previous studies, although this results in a $log(h/u^3)$ distribution that changes only spatially and that does not account for changes in the amplitude of tidal speed over the spring-neap cycle. Values of $log(h/u^3)$ at the front when only the M_2 constituent is included (not shown) fall between 3.25 and 3.75. These M_2-only values cover a narrower range than when the S_2 constituent is included and all fall outside the range 2.7 ± 0.4.

Pingree and Griffiths (1978) note that fronts in the vicinity of the Orkney and Shetland ar-

chipelagoes are found at higher than expected values of $log(h/u^3)$, although they modify the theory to account for bottom drag, so their values of the critical contour are not directly comparable. Salinity gradients and geographical variations in the surface heat flux are suggested as possible reasons for the deviation from predictions. Hughes (2014), using a heat flux appropriate to the northwestern North Sea, concluded from a modelling study that the critical value for frontal location in the region should be 3.4; the applicability of this value was confirmed by examination of 28 years (1982 – 2008 inclusive) of satellite observations of sea-surface temperature (Hughes, 2014). The higher critical value is attributed to the reduced heat flux and enhanced wind mixing at the latitudes of the northwestern North Sea compared with the latitudes of the Celtic Sea (Hughes, 2014), the site of much previous work on the h/u^3 criterion (e.g. Simpson and Hunter, 1974). 3.4 falls within the range of values reported in this study; our observations enable assessment of the critical value derived by Hughes (2014) against full-depth observations of the front.

We acknowledge that the accuracy of $log(h/u^3)$ as a predictor of frontal location is greater in summer, when surface heating is the dominant control on frontal location, than it is at other times of year. However, in the absence of full-depth glider observations of the front in summer, the higher frontal values reported here appear to confirm the tendency, found in both model results and surface observations, for the front in the northwestern North Sea to be found at higher critical values of $log(h/u^3)$ than those once thought applicable to the entire northwestern European continental shelf (Simpson and Sharples, 1994). Glider observations of the front in summer are desirable.

There does not appear to be adjustment of frontal location with the spring-neap cycle, although the effects of such adjustment would be much greater immediately after frontal development – i.e. in late spring and early summer (Simpson and Bowers, 1981). Furthermore, some of the additional mixing energy available at spring tides is expended reducing stored potential energy on the stratified side of the front rather than moving the front itself, limiting the extent of spring-neap frontal adjustment (Simpson and Bowers, 1981). Instead, the dominant signal in frontal location is its offshore movement over the course of the glider deployment (Figure 3.4A). From a longitude of approximately 1.4°W at the start of the deployment, the front moves eastwards into deeper water, reaching approximately 1°W by the middle of November. It then widens considerably towards the end of the deployment, being spread between 1.4 and 0.8°W at the time of the final occupation (19th November – 1st December). A least-squares line of best fit through the frontal locations indicates that the front moves eastward at a rate of 0.53 ± 0.06 km day^{-1}.

3.3.1 Comparison with model output

We compare the observations of frontal location with the output of a numerical model of heating-stirring processes to identify if and when heating-stirring interactions control frontal location during the deployment. We use the open-source, one-dimensional heating-stirring

model of Simpson and Bowers (1984, see also Elliott and Clarke, 1991, and Simpson and Sharples, 2012). The model is straight-forward to run; it may be readily adapted to suit the study region and to work with the glider-derived tide described in Section 3.2; and it includes only the physical heating-stirring processes used to describe frontal location by Simpson and Hunter (1974) and Simpson and Bowers (1984), and described in Section 3.1. Consequently, the model allows us to investigate the extent to which heating-stirring interactions influence the location of the observed front (Figure 3.4).

The model is forced with meteorological parameters from the NOCS Flux v2.0 data set (National Oceanography Centre, 2008; Berry and Kent, 2009, 2011) and with tidal speed. It simulates a temperature profile for a water column of a given depth. 55% of incoming heat energy is absorbed at the surface, the remaining 45% being distributed exponentially with depth. This distribution is typical for coastal waters (Ivanoff, 1977). Once heat loss to the atmosphere has been extracted from the surface layer, the additional heat is mixed downwards until the increase in potential energy equals the effective stirring energy input from the wind over the given time step; the profile is then further modified by bottom-up tidal mixing until the increase in potential energy equals the effective stirring energy input from the tide. If the net surface heat flux is negative (i.e. heat loss) the model simulates convection. The new surface temperature is then used to calculate the surface heat flux for the subsequent time step (Simpson and Bowers, 1984). The original model is modified to include the improved parameterisation of heat exchange through the sea surface implemented by Sharples et al. (2006) and Hughes (2014), and to include the additional energy available for bottom-up mixing provided by a constant background flow of 0.1 m s^{-1} following the method of Hughes (2014). The magnitude of the background flow is chosen to be representative of the values observed in the region (Turrell et al., 1990; Turrell, 1992; Turrell et al., 1996). The stirring effects of a persistent background flow were not included in the original formulation of the h/u^3 theory, but the presence of Atlantic inflow in the study region makes it a necessary addition. More information on these modifications, and on the model equations and set up, is provided in Appendix A alongside illustrative figures.

Temperature profiles are simulated at every 0.1° longitude along the JONSIS section and for every day of the glider deployment at daily resolution. The diurnal heating-cooling cycle is not resolved. We take as the tidal speed the meridional M_2+S_2 velocity amplitude midway between spring and neap tides, and use the glider-derived tide to capture the offshore decay in tidal amplitude. Meridional M_2+S_2 velocity amplitude is calculated at the centre of each bin (Figure 3.1A) and is interpolated onto the longitude of each model grid point. We do not simulate the spring-neap cycle because spring-neap frontal adjustment is not observed in the glider sections (Figure 3.4A).

Using the same definition of frontal location as used for the glider profiles, the heating-stirring model places the front in a similar position to the observations during the first four weeks of the deployment (Figure 3.4A), albeit approximately 0.1° further west prior to 15th

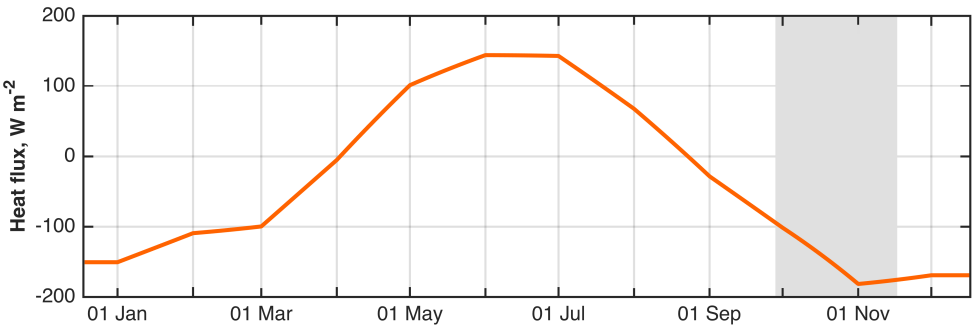

Figure 3.5 Total surface heat flux (i.e. the sum of latent, sensible, incoming radiative and outgoing radiative fluxes; W m^{-2}) in 2013 averaged zonally across the JONSIS section. Positive fluxes indicate energy transfer into the ocean. Latent, sensible and outgoing radiative fluxes are calculated by the heating-stirring model using the method of Sharples et al. (2006) from monthly mean meteorological parameters extracted from the NOCS Flux v2.0 dataset (National Oceanography Centre, 2008). Monthly mean incoming radiative flux is extracted from NOCS Flux v2.0. The period of the glider deployment is indicated by the grey box.

October. The coastal front that appears in the far west of the section between 12th and 14th October is not considered here because it is outside the longitudinal range of the glider sections. We test the sensitivity of the results to the speed of the background flow. Modifying the background flow speed by $\pm$ 0.03 m s^{-1}, a reasonable range, makes no difference to the results at the bottom of the range, and shifts the front by approximately 0.05° longitude (3 km) eastward at the top of the range.

The similarity between the heating-stirring model (with a realistic background current of 0.1 m s^{-1} and an intermediate tidal amplitude) and the observations during the first four weeks of the glider deployment suggests that the interaction between surface heat fluxes and tidal mixing explains the location of the front during this period. Specifically, the negative surface heat flux (i.e. heat loss to the atmosphere) during the period of the glider deployment (Figure 3.5) means that stratification is maintained only by heat remaining in the water column after the period of summer heating (April to September; Figure 3.5). As heat is progressively lost to the atmosphere, the influence of tidal stirring becomes ever more dominant, pushing the front into deeper water (Figure 3.4). However, the persistence of the observed front after 17th November 2013 and its slower easterly advance compared with that of the modelled front (1.59 ± 0.08 km day^{-1}; rate excludes the secondary front that emerges on 15th November 2013 around 0.1°W), suggests that the heating-stirring balance is not the primary control on frontal location in the latter period of the glider deployment (i.e. after approximately 4th November).

3.3.2 Comparison with observations

The existence of the front in the observations despite its disappearance in the heating-stirring model suggests that processes other than heating-stirring interactions are responsible for maintaining the front into the latter weeks of the glider deployment. In addition to the hori-

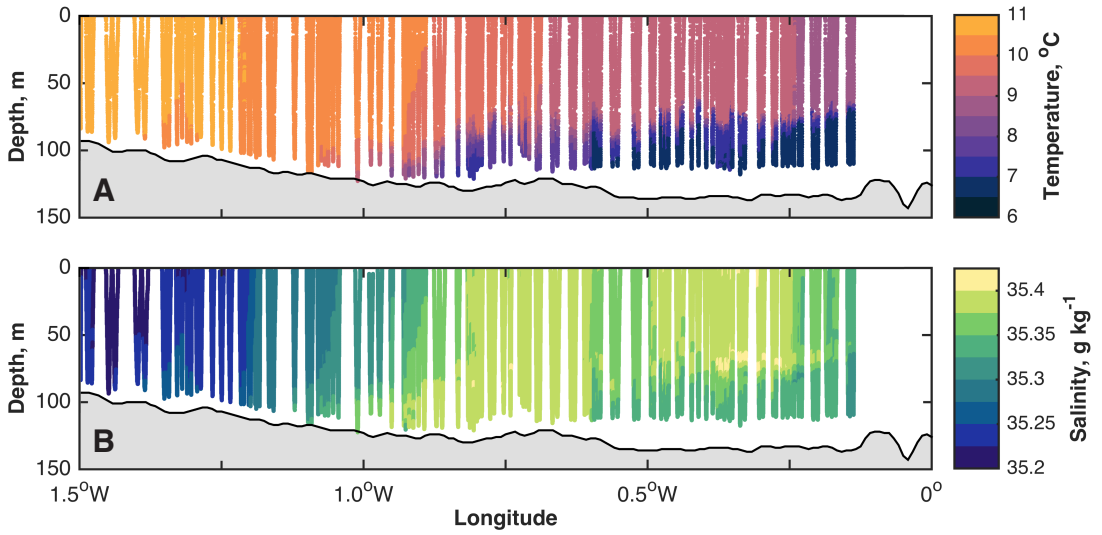

Figure 3.6 **A** Conservative temperature (°C) and **B** absolute salinity (g kg^{-1}) from the penultimate glider occupation of the JONSIS section (14th – 20th November 2013).

zontal temperature gradient observed by the glider on its final two crossings of the front (observations from the penultimate crossing are shown in Figure 3.6) a horizontal salinity gradient exists between the relatively fresh waters in the west of the section and the relatively saline waters in the east. Salinity is a useful water mass tracer in the region and permits identification of the water masses present in the observations. The salinity minimum ($<$ 35.25 g kg^{-1}) to the west of the section is indicative of coastal water from around Scotland, which is freshened by river input and runoff (Dooley, 1974; Turrell et al., 1992); the salinity maximum ($>$ 35.25 g kg^{-1}) to the east of the section is indicative of water of recent Atlantic origin (Turrell et al., 1992). Intermediate salinity ($\sim$35.275 g kg^{-1}) and minimum temperature ($<$ 7.5°C) is indicative of water that has spent the previous summer isolated beneath the seasonal thermocline (Svendsen et al., 1991; Turrell et al., 1992; Hill et al., 2008); this has been called Cooled Atlantic Water (CAW; Turrell et al., 1992). The southward penetration of Atlantic water from the open northern boundary of the North Sea elevates the salinity of CAW (Hill et al., 2008). The heating-stirring model cannot reproduce these water masses: they are not formed locally by heating-stirring interactions and their distribution in the northern North Sea is controlled by advection. The temperature distribution created by these water masses is such that a horizontal temperature gradient is maintained. In particular, the bottom front, which is the most dynamically significant feature of the frontal system (Chapter 2; Hill et al., 2008) is maintained by the presence of the Atlantic-influenced CAW.

The glider observations presented in Figs. 3.4 and 3.6 demonstrate that a front can exist in the northwestern North Sea independently of heating-stirring interactions. Such a front is clearly not simply a tidal mixing front. However, during the first part of the deployment, the observed frontal location compares well to frontal location as predicted from consideration of

only heating-stirring interactions. We propose that the observed front is a hybrid between a tidal mixing front and a front which forms due to horizontal gradients between adjacent water masses in a region of complex water mass interaction. In winter, in the absence of local solar heating and when temperature variation between water masses is negligible, there exists a salinity front in the region that gives rise to thermohaline flow (Chapter 2). In summer, we propose that local heating-stirring interactions modify the water masses to the extent that the front is moved to a position as predicted by consideration of heating-stirring interactions. The present study does not include observations of the front at this time, but when forced with an annual cycle of multi-decadal mean meteorological values, the heating-stirring model places a tidal mixing front at approximately 1.5°W in summer; the front is found at the same location in multi-decadal summertime averages of JONSIS section hydrography (Chapter 2). The observations presented in this study (Figure 3.4A) capture the period in the annual cycle when, in 2013, the front makes the transition from being a front controlled by heating-stirring interactions to being a front controlled by the distribution of water masses.

3.4 Summary

We have demonstrated that glider DAC observations may be used to determine tidal velocities at the time and location of each glider dive to within $\pm$ 0.04 m s^{-1}. Glider-derived tidal velocities compare favourably to output from current meters and the TPXO tide model. The method enhances the utility of gliders as an ocean-observing platform, particularly in regions such as Antarctica where tide models are known to be poorly constrained. The method could also be extended to two dimensions: for instance, to two gliders flown along parallel transects, or to one or more gliders flown in a butterfly pattern. A longer deployment than the two-month deployment presented in this study would allow for more tidal constituents to be resolved from the resulting DAC time series.

Glider-derived tidal velocities were applied to study the location of a front in the northwestern North Sea. The results of a one-dimensional heating-stirring model, and comparison of these results with the glider's hydrographic observations, demonstrated that salinity gradients and the distribution of water masses are important controls on frontal location in the region, in addition to surface heating and primarily tidally induced mixing. A water mass distribution exists which gives rise to a frontal boundary in temperature and salinity. In the absence of significant surface heating, this is the primary source of a frontal boundary and therefore the primary control on frontal location. In summer, heating-stirring interactions modify the water masses, enhancing the background temperature gradient such that heating-stirring interactions become the primary control on frontal location. This situation persists until the autumn: the observations presented in this study capture the period during which, in 2013, the front transitions from being primarily a tidal mixing front to being primarily a front between different water masses. The interannual variability of the timing of this transition is a topic for further

investigation.

Increasing the temporal resolution of the meteorological observations used to force the heating-stirring model – for instance, by using daily values from the ERA Interim re-analysis rather than monthly values from NOCS Flux v2.0 – could lead to a more complete understanding of how frontal location changes on day-to-day time scales, and could produce more variability in modelled frontal location. This would not require any fundamental change to the model set-up. A further possible experiment would be to include the effects of salinity in the model, to test the hypothesis that haline buoyancy plays a dominant role in determining frontal location during the winter.

Water mass distribution and attendant spatial gradients of thermal and haline buoyancy are likely to be important in shelf seas where significant incursions of oceanic water are found, such as the northwestern North Sea, the South China Sea (Shaw, 1991; Su, 2004), along the eastern coast of the United States (Blanton et al., 1981) and around Antarctica (Moffat et al., 2009). While heating-stirring interactions are ubiquitous in shelf seas, fronts in such regions may persist during periods when local heating-stirring interactions would not promote frontal formation. Consequently, controls on frontal location may change over an annual cycle. Given the thermohaline flows commonly associated with shelf sea fronts, and given the influence that fronts have on the distribution of physical and biogeochemical properties (Turrell, 1992; Hill et al., 2008), this has important implications for the dynamics, ecology and management of shelf sea regions.

Chapter 4

Hydrography, transport and forcing of the northwestern inflows

4.1 Introduction

The North Sea is a shallow sea on the northwest European continental shelf which separates the United Kingdom from mainland Europe (Figure 1.1). Inflow to the North Sea occurs through the Fair Isle Current (FIC; 0.5 Sv), the East Shetland Atlantic Inflow (ESAI; 0.5 Sv), the Norwegian Trench Inflow (NTI; 1.2 Sv) and the English Channel Inflow (ECI; 0.2 Sv; Figure 1.1; volume transports from Winther and Johannessen, 2006). The waters of the NTI retroflect largely within the Norwegian Trench (Furnes et al., 1986) and volume transport of the ECI is considerably less than that of the other three inflows (Otto et al., 1990; Winther and Johannessen, 2006). Consequently, it is the FIC and ESAI, the northwestern inflows, that have the greatest effect on conditions in the northern North Sea (Chapter 2). The FIC originates to the west of the Fair Isle Gap (FIG), the narrow sea passage between the Orkney and Shetland archipelagoes through which the current enters the North Sea (Figure 1.1); it comprises a mixture of Atlantic water from the northward-flowing European Shelf Edge Current (ESEC; Figure 1.1; Marsh et al., 2017) and low-salinity coastal water from around the complex island chains off the western coast of Scotland (Dooley, 1974; Turrell et al., 1992, 1996). Within the North Sea, the path of the FIC has been traced southward from the FIG to approximately 57.5°N (Dooley, 1974; Turrell et al., 1992). The ESAI comprises water of more recent Atlantic origin (Turrell et al., 1992) and is fed by waters of the ESEC that cross onto the continental shelf to the north of the Shetlands (Turrell et al., 1996). Within the North Sea the ESAI follows a similar path to the FIC (Turrell et al., 1992). The ESAI is a more diffuse flow than the FIC, but average transports in the two currents are similar (Winther and Johannessen, 2006).

The hydrographic properties of inflowing water masses, combined with the rate of the inflow, exert a strong influence on a region's ecosystem (Lindley et al., 1990; Holliday and Reid, 2001; Edwards et al., 2002; Beaugrand, 2004) and are the means by which oceanic perturbations may propagate into the region (Dickson et al., 1988; Holliday and Reid, 2001; Edwards et al., 2002). An accurate physical description of the inflows is a prerequisite for developing reliable models of a region's water quality, biogeochemistry and ecology (Taylor, 1987; Turrell and Henderson, 1990; Skogen and Moll, 2005), and for understanding potential contaminant pathways (Taylor, 1987; Turrell and Henderson, 1990; du Bois, 1996). The adoption of the European Union's Marine Strategy Framework Directive (EU, 2008), which requires that the EU member states of the North Sea perimeter ensure "good environmental status" of their territorial waters, provides a regulatory impetus for improving both understanding and management. It is common, both in published studies (e.g. Turrell et al., 1996), and in scientific reports and indices (e.g. the annual Report on Ocean Climate published by the International Council for the Exploration of the Sea; Larsen et al., 2014, 2016, ocean.ices.dk/iroc) to use standard longitudes and depths to define the characteristics of water masses. This method assumes that the distribution of water masses is more or less constant in time. Measurements of a sufficiently high resolution to examine the validity of this assumption have not yet been presented in the literature.

The hydrography and circulation of the northwestern North Sea change seasonally. The northwestern inflows are thought to consist of primarily wind-driven flow in winter and of primarily density-driven, thermohaline flow in summer (Dooley, 1983; Otto et al., 1990; Turrell et al., 1990; Svendsen et al., 1991; Turrell, 1992; Pohlmann and Puls, 1994; Winther and Johannessen, 2006). Winther and Johannessen (2006) find that North Sea inflows are strongly influenced by westerly winds in winter and spring, when stratification is absent (Chapter 2), but not in summer and autumn. Similarly, Mathis et al. (2015) find an enhanced ocean response to westerly wind forcing in winter than in summer; Turrell et al. (1990) find a linear response to southwesterly wind stress in winter that is far less pronounced in summer. Sheehan et al. (2017) found a clear annual cycle of thermohaline flow that closely followed the spring growth and fall decay of stratification (Chapter 2). Strong tidal mixing in the vicinity of the FIG and to the east of the Orkney Islands (Chapter 3; Turrell et al., 1992) fully vertically mixes the water column: this sets up a horizontal bottom temperature gradient between warm bottom waters in the coastal mixed zone and cool bottom waters in the stratified zone (Chapter 2) that forces a southward thermohaline flow. The horizontal salinity gradient between relatively fresh coastal water and relatively more saline oceanic water offshore forces also forces a southward thermohaline flow. The location and nature of the sharp, bottom-intensified front that separates the mixed and stratified regions has been shown to vary seasonally (Chapters 2 and 3). In summer, it is primarily a tidal mixing front, its location and nature determined by the interaction between surface heat input and tidal mixing. In winter, it persists as the boundary between different water masses advected to the northwestern North Sea through the northwestern inflows

and it is primarily visible in the salinity distribution. Chapter 3 present observations of the offshore (i.e. eastward) advance of the front that coincides with the autumn decay of stratification and the switch between the two frontal regimes (Chapter 3).

The proposed annual cycle in the forcing of the northwestern inflows leads to the separation of flow into thermohaline- and wind-driven components (e.g. Chapter 2; Dooley, 1983; Turrell, 1992; Turrell et al., 1992). The wind-driven component is simply taken to be the difference between the thermohaline-driven transport and the absolute transport. This separation of the flow gives no consideration to the contribution of open-ocean forcing to flow within the North Sea – that is, flow that would occur in the absence of wind forcing and North Sea density structure – which has received little attention (Holt and Proctor, 2008). Furthermore, to date, there has been no investigation into where the wind stress occurs in order to drive inflow: into whether wind stress pushes water into the northwestern North Sea from the northern Atlantic, or whether wind stress pulls water from the northern Atlantic into the northwestern North Sea. Here, we use observations collected by an autonomous ocean glider to examine water mass characteristics in the northwestern inflows at unprecedented spatial resolution over a two-month period, presenting the most high-resolution description yet of the water masses flowing into the northwestern North Sea. We examine velocity observations obtained by the glider and derived thermohaline flows to assess the contribution of thermohaline flows to circulation in the region, and to identify the region over which wind stress has the greatest effect on the northwestern inflows.

4.2 Glider data processing

The Joint North Sea Information System (JONSIS) section is a hydrographic section between 2.23°W and the prime meridian at 59.28°N (Figure 1.1). The section is occupied multiple times a year by Norwegian and British research ships and has been for a number of decades (Chapter 2). A Seaglider (SG502; Eriksen et al., 2001) deployed along the section in 2013 made 10 repeat partial occupations between 12th October and 2nd December (Berx et al., 2018). 1,520 dives were recovered from the glider; dives were, on average, 20 minutes in duration and 300 m apart. Most sampled the full water column. The glider was equipped with an un-pumped Seabird CTD and a WETLabs Eco Puck optical sensor that measured chlorophyll *a* fluorescence at 470/695 nm and scattering at 470 nm (blue) and 700 nm (red) wavelengths. Hydrographic observations were processed using the UEA Glider Toolbox[1] (Queste, 2013) to optimise the hydrodynamic model of the glider's flight path (Frajka-Williams et al., 2011) and to correct for thermal lag of the un-pumped conductivity cell (Figure 4.1; Garau et al., 2011). This second process is especially important for removing artificial spikes in salinity profiles: erroneous measurements that arise from a mismatch between the water temperature recorded by the glider and the actual water temperature inside the conductivity cell. Because the strength

[1] www.bitbucket.org/bastienqueste/uea-seaglider-toolbox

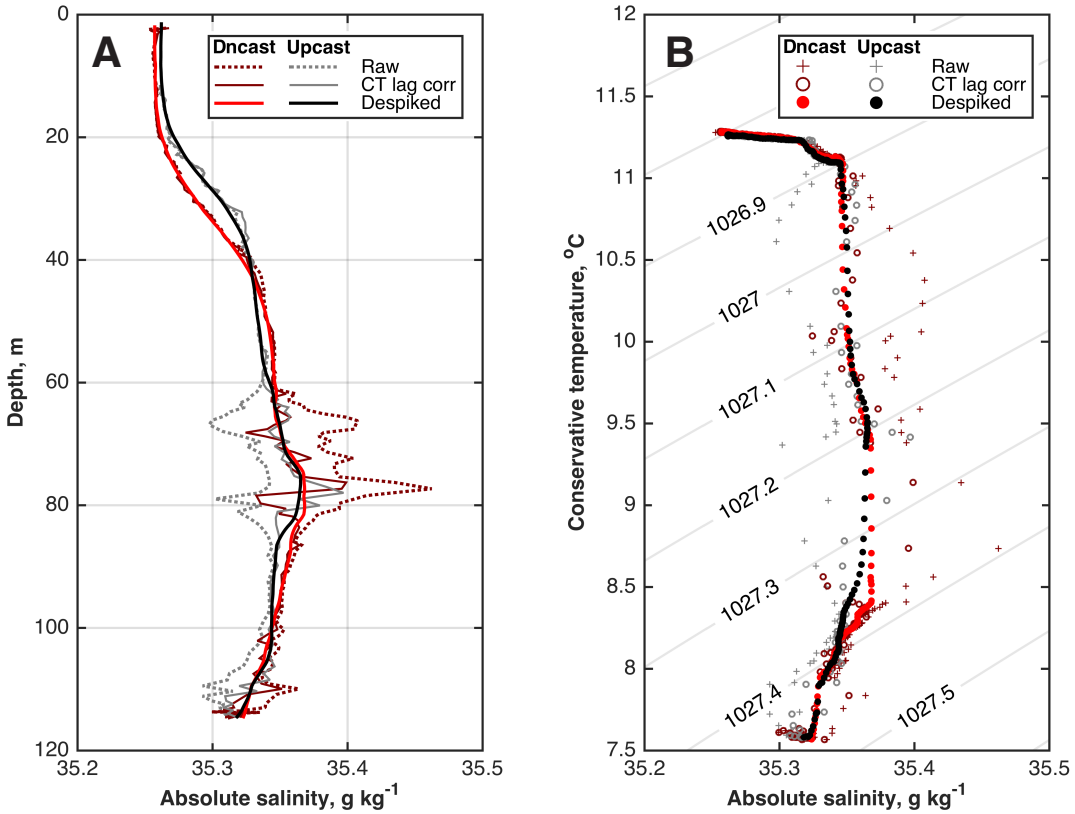

Figure 4.1 **A** Depth profiles of absolute salinity (g kg^{-1}) from dive 255 (0.78°W, 17th October 2013, 04:45 UTC) at different stages of the despiking processes. **B** The same two profiles plotted in temperature-salinity space, with contours of potential density (kg m^{-3}). Down: downcast. Up: upcast. Raw: uncorrected profile. CT lag corr: profile corrected to minimise effect of thermal lag of the CT cell (Garau et al., 2011). Despiked: profile corrected to remove spikes and smoothed with 5 m running median.

of the thermocline in the study region was such that thermal lag correction alone was insufficient to remove all the spikes, additional quality control procedures were necessary. To remove remaining spikes that were symmetrical about the mean of each upcast-downcast pair, salinity measurements that differed from the mean of a given dive-climb pair by more than 0.01 g kg^{-1} were removed and interpolated over. To remove spikes that were not symmetrical about the mean of a dive-climb pair, all salinity profiles were then smoothed with a 10 m running mean calculated over a square window. These last two procedures had little effect at the top and bottom of dives where the data are more reliable and where vertical gradients are small, but produced a smooth profile at the depth of the thermocline where the unprocessed observations were clearly unphysical (Figure 4.1). Temperature and salinity are presented as the TEOS-10 variables conservative temperature and absolute salinity respectively (IOC et al., 2010) and are used to calculate potential density; all subsequent uses of temperature and salinity refer to these TEOS-10 variables.

The glider's temperature and salinity observations from its first complete occupation of the

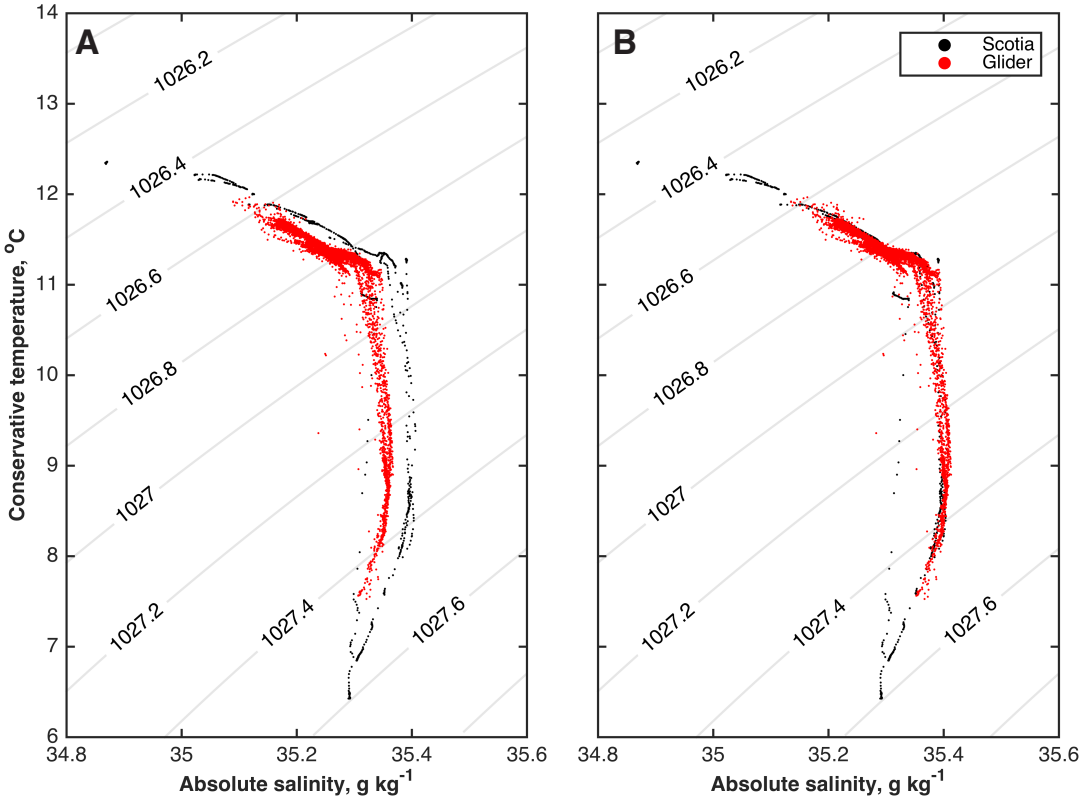

Figure 4.2 Temperature and salinity observations from the first glider occupation of the JONSIS section (red) **A** before and **B** after salinity calibration against observations from the MRV Scotia deployment cruise (black).

JONSIS section (14th – 17th October 2013) were compared to the temperature and salinity observations from the JONSIS section collected by the MRV Scotia[2] immediately after the glider deployment (13th – 14th October 2013; Figure 4.2). These ship observations are the closest in time and space to the initial glider observations. Salinity observations made by the Scotia CTD are calibrated against salinometry. A salinity offset between the glider and ship observations was found (Figure 4.2A). Glider observations from the up- or downcast closest in longitude to the stations occupied by the Scotia were interpolated onto the same depths as the ship observations (i.e. every 1 m. At each depth, the glider observation was subtracted from the ship observation; the median difference was 0.0455 g kg^{-1}. This offset was added to all glider salinity observations, improving agreement with observations from the Scotia (Figure 4.2B).

Particulate backscatter intensity, b_{bp} (m^{-1}), was calculated from the observed volume scattering function (VSF), β, at a centroid angle of 124° and a wavelength of 470 nm after Green et al. (2014) and Hall et al. (2017). β was measured using a glider-mounted WETlabs Eco Puck optical sensor; the centroid angle and wavelength are properties of the sensor. The VSF of pure seawater, β_{sw}, which is dependent on wavelength, centroid angle, temperature and salinity, was calculated following the method of Zhang et al. (2009); β_{sw} was then subtracted

[2]www.gov.scot/resource/0039/00391672.pdf

from β to determine β_p, i.e. the particulate-only VSF. β_p was converted to b_{bp} using:

$$b_{bp} = 2\pi\chi_p\beta_p \tag{4.1}$$

where χ_p is a conversion factor (Chami et al., 2006). For a given centroid angle, χ_p may be assumed to be wavelength invariant in the absence of phytoplankton blooms (Chami et al., 2006); chlorophyll concentrations observed during this deployment are below that at which the effect of phytoplankton must be accounted for (Chami et al., 2006). We take χ_p to be 1.2 for a centroid angle of 124° and a wavelength of 470 nm, although we note that it could fall between 1.1 and 1.3 (Chami et al., 2006). Altering χ_p within this range would change the derived values of b_{bp} by up to 10%, but would not change the distribution. We assume that backscatter intensity is a qualitative proxy for suspended sediment concentration. Chlorophyll *a* concentration was calculated using the manufacturer's calibration; the results from the first glider occupation were found to compare well to chlorophyll *a* concentrations calculated from bottle samples taken during the cruise that deployed the glider.

The majority of glider dives were at latitudes south of the JONSIS section (Figure 4.3A), as strong tidal currents and a generally southward residual flow made keeping to the transect challenging. In the northwestern North Sea, the FIC is known to follow the 100 m isobath, which makes an average angle of 28° with meridians in the study region (Figure 4.3A). However, the average dive-average current vector (DAC; Chapter 3; not shown) was not directed along this isobath, making instead an angle of just 4°with meridians; average meridional velocity was 0.13 m s^{-1}, while average zonal velocity was less than 0.01 m s^{-1}. Therefore, no attempt was made to account for southward excursion of the glider during data processing. Observations from pronounced loops in the glider's track due to tidal advection were excluded, as were the final dives made by the glider as it travelled southward from the JONSIS section prior to recovery (Figure 4.3A).

The processed observations were optimally interpolated (Bretherton et al., 1976; Denman and Freeland, 1985; Chereskin and Trunnell, 1996) onto a regular grid using a Gaussian weighting function, following the method used to interpolate ship-based observations in Chapter 2. Grid spacing was 0.01° longitude (568 m) in the horizontal and 2 m in the vertical. Semivariograms were used to determine appropriate correlation length scales for the interpolation. Semivariograms quantify the the dissimilarity between observations as a function of distance between them. The maximum permissible length scale is the distance at which dissimilarity ceases to increase with distance, although the length scale may be set below this maximum Janssen et al. (1999). The length scales were set at 0.02° longitude and 5 m in the horizontal and vertical respectively. The length scales were considerably less than the maximum permissible length scales, reflecting the need to use only the most closely correlated neighbouring data points in the interpolation – for instance, to preserve sharp thermoclines. More information on semivariogram analysis is presented in Box 4.1 on page 11. Bathymetry

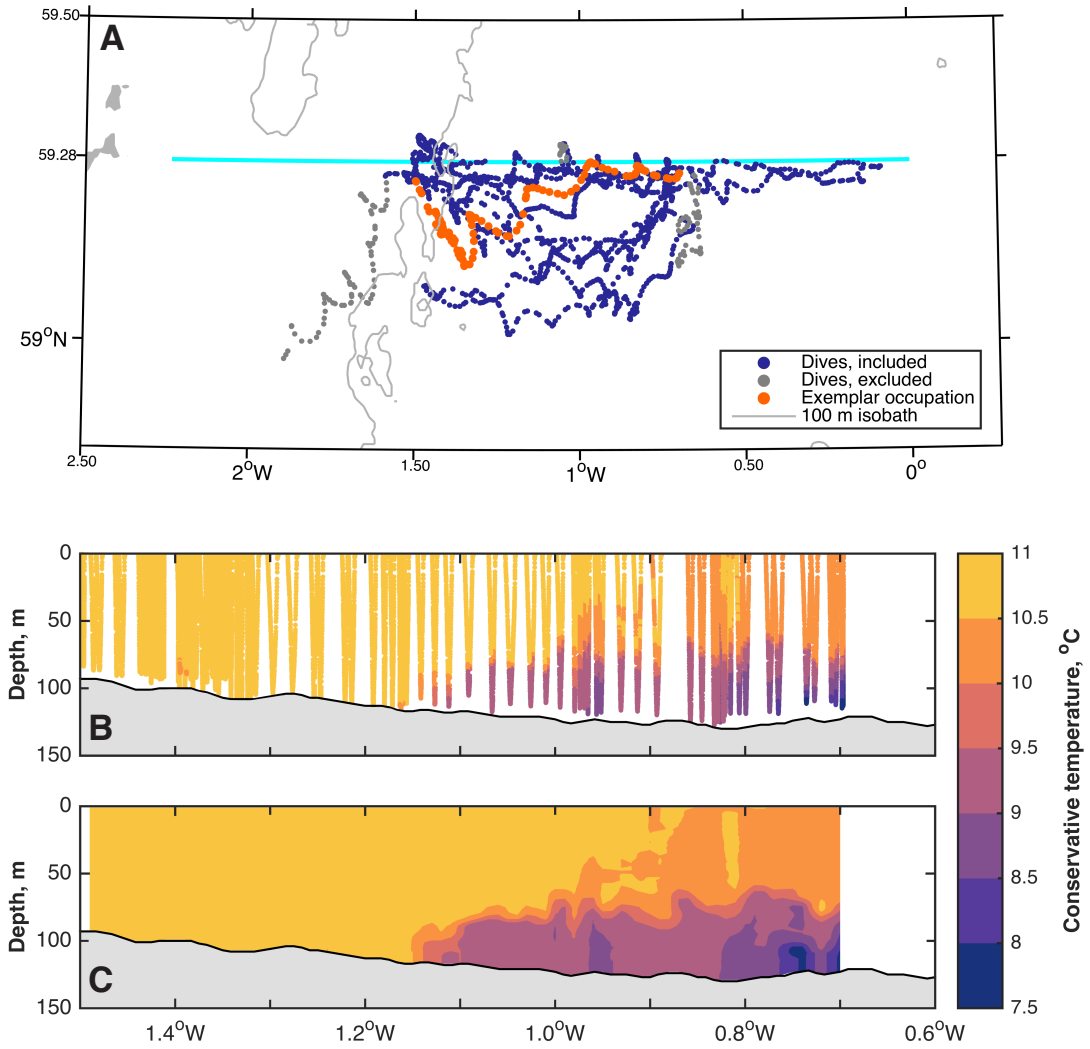

Figure 4.3 **A** The location of glider dives. Blue circles indicate dives included in the optimal interpolation; grey circles indicate dives excluded from the optimal interpolation. Dives in the exemplar occupation shown in panel B are shown in orange. The 100 m isobath is marked in grey, land is shaded and the JONSIS section is shown in cyan. **B** Glider observations of conservative temperature (°C) from an exemplar occupation prior to interpolation and **C** after interpolation. Note that panel C shows the extrapolated version of the interpolated observations.

was extracted from the GEBCO dataset[3] (resolution 30 arc-seconds). An exemplar occupation before and after interpolation is presented in Figure 4.3B and 4.3C).

Interpolated temperature and salinity fields were smoothed horizontally using a Gaussian-weighted running mean prior to calculating the geostrophic shear. The standard deviation of the Gaussian function was 2000 m, the first baroclinic Rossby radius at the latitude of the JONSIS section. This radius is typical of shallow, stratified shelf seas at higher latitudes (e.g. Nurser and Bacon, 2014). Where observations did not cover the entire water column, the

[3]GEBCO_08 grid, version 20100927, www.gebco.net

deepest observation in the interpolated data set was extrapolated to the sea floor using a nearest-neighbour method. The thermohaline component of the inflows – i.e. flow driven by horizontal temperature and salinity gradients – was derived by referencing the geostrophic shear to an assumed level-of-no-motion at the deepest common level between adjacent horizontal grid points. DAC observations were de-tided using the TPXO inverse model European shelf solution[4] (0.1° resolution; M_2, S_2, N_2, K_2, K_1, O_1, P_1, Q_1, M_4, MS_4, MN_4 constituents; Egbert et al., 1994; Egbert and Erofeeva, 2002; Egbert et al., 2010). More information about DACs may be found in Chapter 3. The de-tided velocities were linearly interpolated onto the same longitudinal grid as the hydrographic observations and were smoothed using a horizontal Gaussian-weighted running mean with a radius of 2000 m. The absolute velocity was calculated by referencing the geostrophic shear to the de-tided, gridded, smoothed meridional DAC velocity. Thermohaline transport and absolute transport were derived from the thermohaline velocity and absolute velocity respectively. For each occupation, we calculate both the thermohaline transport and the absolute geostrophic transport over the full width of each glider occupation; we call this the full-width transport. This width is variable and so the full-width transports may not be compared over time; note, for instance, that longitudes east of approximately 0.6°W are sampled only in two occupations (Figure 4.3A). We also calculate the thermohaline transport and the absolute transport across that portion of the JONSIS section that is sampled by the glider in all 10 occupations: this is referred to as the standardised section and the associated transports as the standardised transports. Standardised transport values are comparable over time. Negative transports are southward – that is, into the North Sea.

We use a Monte Carlo technique to estimate transport error arising from uncertainty in the DAC observations. For each of the 10 occupations, we created a set of 1000 assumed errors taken from a normal distribution with a standard deviation of 0.04 m s^{-1}. The assumed errors were added to the gridded DAC observations, and for each of the 1000 sets the absolute transport is calculated. The standard deviation of these 1000 transports is taken to be the representative uncertainty that arises from DAC uncertainty. Additional uncertainty may be expected to arise from the nearest-neighbour extrapolation of the observed temperature and salinity values to the seafloor in order that transport estimates be integrated over the entire water column. The uncertainty associated with the extrapolation cannot be quantified – although we assume that it increases the accuracy of our results relative to not doing the extrapolation – but it is likely to be near-negligible in regions with minimal bottom temperature and salinity gradients, such as the east and west of the section (Figures 2.3 to 2.6, and 3.6). Uncertainty is likely greatest in the region of the bottom front. Uncertainty in the GEBCO bathymetry and in the TPXO tide model would also contribute to uncertainty in the transport estimates, although again these uncertainties are difficult to quantify accurately.

[4] volkov.oce.orst.edu/tides

4.3 Hydrography

4.3.1 Water masses

The large range of temperatures and salinities observed by the glider (Figure 4.4) is indicative of the diverse water masses present at the JONSIS section in autumn (Figure 4.5A; to avoid crowding, we present three sections in this figure that contain features of interest). The very warmest water observed by the glider is also the freshest (Figure 4.4). This is the signal of Scottish Coastal water (SCW; Figure 4.5A; Turrell et al., 1992), which generally occupies the shallower western portion of the section closest to the coast (Figure 4.4). This water lies to the west of the Fair Isle Current (Figure 1.1) and is therefore found to the far west of the JONSIS section. SCW originates in the Scottish Coastal Current, a low-salinity, near-shore, flow that originates in the Irish Sea and flows northward up the western coast of the United Kingdom (Figure 1.1). The current is further diluted by river input and run off around the complex island chains to the northwest of the United Kingdom (Turrell, 1992; Turrell et al., 1992; Hill et al., 1997; Huthnance et al., 2009; Inall et al., 2009). The location of SCW is variable on short (four to five days) time scales, which was not apparent in previous ship-based surveys of the region (e.g. Chapter 2A; Turrell et al., 1992). For instance, in occupations one to three, SCW extends eastward across the surface, overlying considerably more saline waters immediately below. This feature is most pronounced in occupation three, where a core of SCW is observed at the surface at approximately 1°W (Figure 4.4). In occupation four, some four days later, there is no evidence of this core and the vertical salinity gradient is greatly reduced. In occupations four, five and six, SCW is not present in the observations, presumably because it has retreated to shallow, western waters not sampled by the glider. The two-month duration of the glider deployment allows us to follow the changing properties of SCW through the autumn decay of thermal stratification. The temperature of SCW decreases from between 11.5 and 12°C at the start of the deployment to between 10 and 10.5°C at the end of the deployment (Figure 4.4), likely a consequence of surface heat loss over the period (Figure 3.5). In Figure 4.5A, we distinguish between the temperature-salinity signal of SCW in October (SCW_{Oct}) and SCW in November (SCW_{Nov}). This cooling of approximately 1.5°C reduces the density of SCW by almost 0.3 kg m^{-3}. The salinity of SCW remains unchanged over this period.

The water mass that is more saline and marginally cooler than SCW is FIC water, the core water mass of the FIC (Turrell et al., 1992). FIC water is found to the east of SCW and overlies the cooler, more saline waters at the bottom to the east of the section (Figure 4.4). FIC water is slightly cooler than SCW, having a temperature of between 10.5 and 11°C in early occupations (e.g. occupation three in Figure 4.5A) to between 9 and 9.5° in late occupations (e.g. occupation 10 in Figure 4.5A). In some occupations (e.g. occupations five, six and seven), FIC water is present as the previously described well-mixed strip of water, the eastern extent of which overlies more saline water at the seafloor (Turrell et al., 1992, Figure 4.4); in other occupations, this distribution is disrupted by eastward extensions of SCW (e.g. occupations

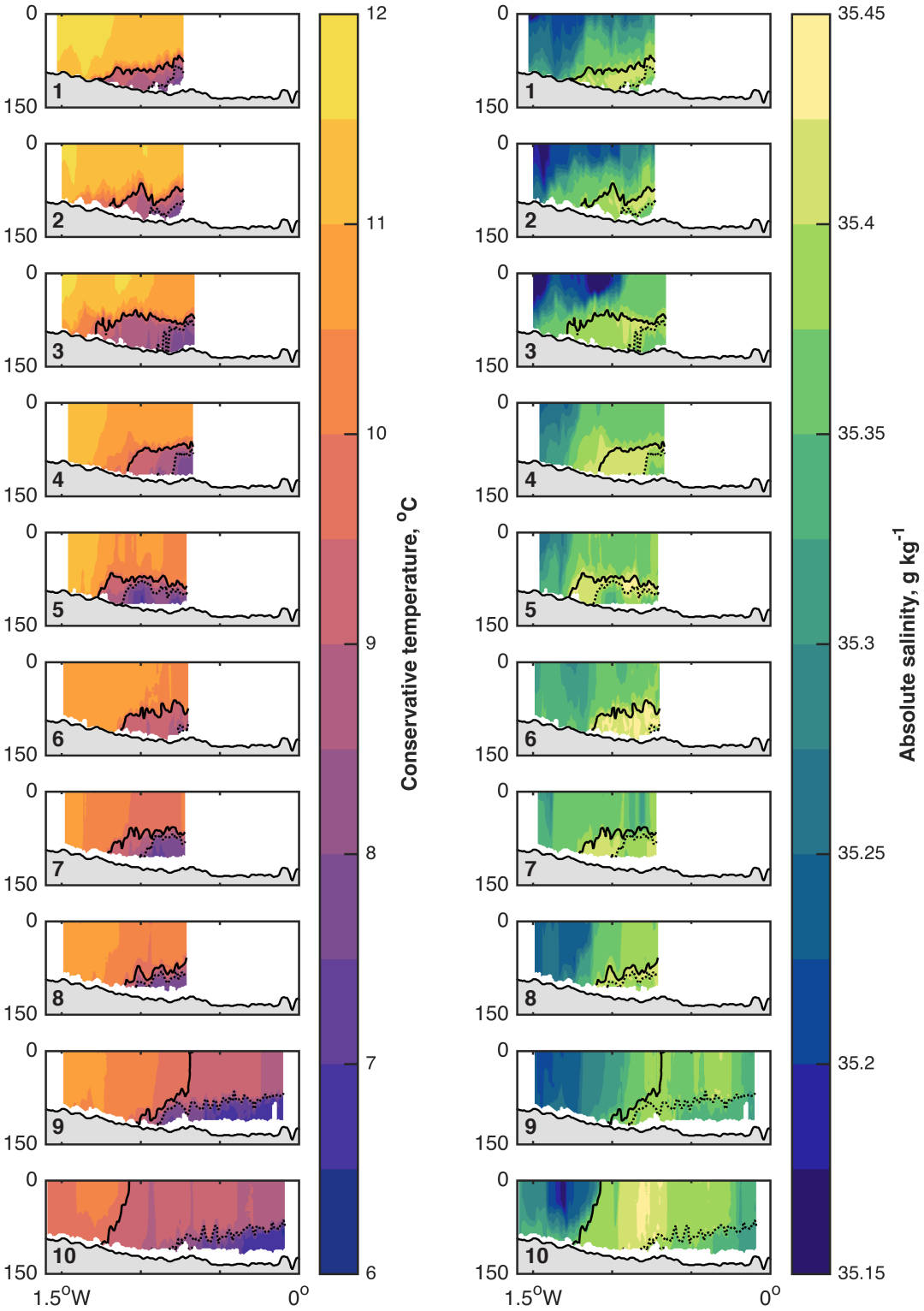

Figure 4.4 Conservative temperature (°C, left-hand side) and absolute salinity (g kg^{-1}, right-hand side). The 1027.2 kg m^{-3} isopycnal (solid line) and 1027.4 kg m^{-3} isopycnal (dotted line) are plotted. Occupation number is in the bottom left of each panel.

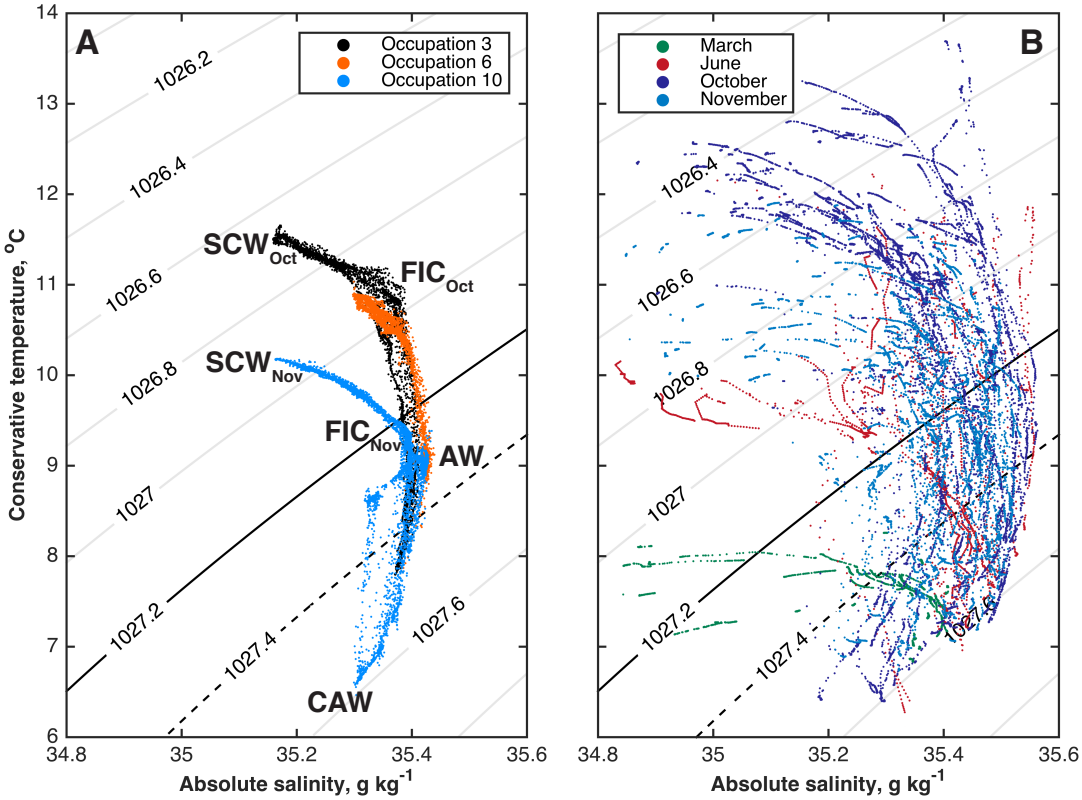

Figure 4.5 **A** Temperature-salinity plot of glider observations from occupations three (black), six (orange) and 10 (blue). SCW: Scottish Coastal water. FIC: Fair Isle Current water. AW: Atlantic Water. CAW: Cooled Atlantic Water. **B** Temperature-salinity plot of ship observations from all Marches (green), Junes (red), Octobers (dark blue) and Novembers (light blue) in the 27-year data set presented and described in Chapter 2. In both panels, contours are of potential density (kg m^{-3}); the 1027.2 and 1027.4 kg m^{-3} isopycnals are plotted as a solid and dashed black line respectively, as in Figures 4.4, 4.6 and 4.8.

two and three). The large number of observations that lie on the mixing line between SCW and FIC water attests to the high degree of mixing that occurs between the two water masses in the current systems to the north and west of Scotland (Dooley, 1974; Turrell et al., 1990, 1992). We use the same subscript notation introduced above to distinguish between the temperature-salinity FIC water in October and in November. The observed temperature decrease in FIC water matches that of SCW, suggesting that heat loss to the atmosphere affects both water masses to a comparable extent. The salinity of FIC water is greater than that of SCW, a consequence the mixing of high-salinity Atlantic water into the FIC (Dooley, 1974; Turrell et al., 1992).

The most saline water observed by the glider has a salinity of over 35.4 g kg^{-1} (Figure 4.4) and is the most undiluted Atlantic-origin water to be found in the northwestern North Sea (Turrell et al., 1992). Following earlier convention, we refer to this as Atlantic Water (AW; e.g. Turrell et al., 1992). The temperature of AW remains at just over 9°C, and its core density is just over 1027.3 kg m^{-3} (Figure 4.5A). In observations obtained in September 1987, Turrell et al. (1992)

find AW at the bottom of the water column, sitting just to the east of FIC water. Our glider observations reveal a more complicated picture. As surface heat loss cools the water column during the deployment (Chapter 3) and thermal stratification breaks down, density tends to increase (Figures 4.4 and 4.5A). In particular, note the outcropping of the 1027.2 kg m^{-3} isopycnal that occurs between occupations eight and nine, and its westward retreat between occupations nine and 10 (Figure 4.4). In these final two occupations, the proportion of the section that falls between the 1027.2 and 1027.4 kg m^{-3} isopycnals, in which density range AW is found, is greater than in occupations one to eight. Consequently, AW is considerably more prevalent in occupation 10 than in earlier occupations: the outcropping of the 1027.2 kg^{-3} isopycnal allows AW to occupy the entire water column in occupation 10 (between 0.75 and 1°W), whereas in earlier occupations (e.g. four to six) it is confined to depths below 80 m (Figure 4.4). Turrell et al. (1992) trace AW northwards from the JONSIS section to the region to the east of the Shetlands. Their near-surface salinity measurements suggest that, in September, AW is found close to the surface around the southern tip of the Shetlands, but that it is subducted beneath the less dense SCW and FIC water entering the North Sea through the Fair Isle Gap (FIG) as it travels southward. Our observations suggest that any such subduction is likely to be a summer phenomenon, with AW being able to remain at the surface in winter when the average density of the water column is greater. Outside the North Sea, dynamics in the Faroe-Shetland Channel – for instance, fluctuations in the location of the ESEC (Figure 1.1) – are thought to control how much water from the open northern Atlantic is transported onto the northwestern European continental shelf (Huthnance et al., 2009).

It is possible that mixing between FIC water and AW changes the salinity of FIC water over the course of the deployment. Unlike the salinity of SCW water, the salinity of FIC water increases over the deployment from the lower to the upper end of the range 35.35 to 35.4 g kg^{-1} (Figure 4.5A). Coupled to the cooling, this reduces the density of FIC water from around 1026.9 to 1027.2 kg m^{-3}, drawing the core density of SW closer to that of AW (Figure 4.5A). Consequently, as the temperature of SW decreases and the density difference between SW and AW decreases, mixing between the two water masses becomes more likely. Acting together, an increase in the salinity of FIC water brought about by possible mixing with AW (Figure 4.5A), and the shoaling of AW (Figure 4.4) strengthen the horizontal salinity gradient, and could, in part, bring about the transition between summertime thermohaline flow driven primarily by the temperature distribution and a wintertime thermohaline flow driven primarily by the salinity distribution (Chapter 2).

The coldest ($>$ 7°C), densest ($>$ 1027.4 kg m^{-3}) water observed by the glider is Cooled Atlantic Water (CAW; Turrell et al., 1992). It is observed only in the deepest and most eastern parts of the section. CAW is what remains of water trapped beneath the seasonal pycnocline, its temperature being set by ocean-atmosphere exchange the preceding winter (Turrell et al., 1992). CAW is thought to cover large portions of the seafloor in the northern North Sea, and the horizontal density gradients between it and surrounding water masses of lower density are

a key driver of thermohaline circulation in the region (Hill et al., 2008). The salinity of CAW is lower than that of AW, which is of more recent oceanic origin (Turrell et al., 1992), and is even slightly lower than that of FIC water (Figure 4.5A). This is potentially a consequence of fresh water input from rainfall while the water column is well mixed during winter (Turrell et al., 1992). The full-depth spreading of AW observed during the final occupation (Figure 4.4) could well be the first phase in the formation of CAW for the following year: bringing AW into contact with the atmosphere until the formation of the next year's seasonal pycnocline submerges it below warmer, fresher surface layers. AW entering the North Sea via the northwestern inflows, particularly at times of year when it is in contact with the atmosphere – i.e. in winter, between the breakdown of stratification (Figure 4.4) and the development of stratification the following spring – is therefore a key means by which open-ocean properties may propagate into and be stored in the northern North Sea on inter-seasonal time scales. Furthermore, the properties of AW entering the North Sea in autumn and winter, before its hypothesised conversion in CAW, could therefore be of key importance to bottom-dwelling organisms, as it will set the hydrographic conditions of benthic habitats for the coming year.

FIC water does not lie on a direct mixing line between SCW and AW, either in early or late occupations (Figure 4.5A), implying that mixing between either FIC water or AW, or both, and a third water mass is responsible for setting its properties. Turrell et al. (1992) find evidence of water from the Norwegian Coastal Current (NCC) in the central North Sea and infer a broad region of mixing between and FIC water NCC water. The salinity signal of NCC water at the surface towards the east of the JONSIS section is apparent in long-term hydrographic averages of summer conditions (Chapter 2); wind conditions in summer are more conducive to westward Ekman transport across the North Sea (Sætre et al., 1988). The FIC water in our observations could therefore be influenced by mixing with a westward extension of NCC water from the summer immediately prior to the glider deployment; its salinity is similar to that taken to be the signal of westward extensions of NCC water (Chapter 2). However, it is also possible that surface water found in the central northern North Sea is of a lower salinity than inflowing AW at greater depths, perhaps because of precipitation.

The shape of the temperature-salinity distribution in October and November from historical observations is qualitatively similar to that observed by the glider in 2013 (Figure 4.5B), although there is clearly a large degree of interannual variability in the temperatures and salinities of both SCW and AW (Figure 4.5B). For instance, the salinity of AW can, in October, vary between 35.3 and 35.55 g kg^{-1} over the 27 years of observations, and the temperature of SCW can, also in October, vary between 10 and 13.5°C; this, along with putative variability in the degree of mixing between the two, leads to a comparably large degree of interannual variability in the temperature and salinity of FIC water (Figure 4.5B). The temperature and salinity properties of CAW are similarly variable. Changes in temperature and salinity appear to occur together: warm years tend also to be salty years, and vice versa (Figure 4.5B). The pronounced cooling of SCW and FIC water between October and November that occurs in

2013 also appears to be consistent with the pattern found in the historical observations.

SCW and FIC water as observed by the glider in 2013 sit at the cooler and fresher end of the range observed in previous years (Figure 4.5), although the exact properties of, in particular, FIC water over the time series are difficult to define exactly. Furthermore, the salinity of SCW as observed by the glider is difficult to compare with previous years given that the glider likely did not sample the end-point of this water mass: salinity decreases, and SCW concentration is presumed to increase, with distance west (Figures 4.4 and 4.5), and the glider did not occupy the JONSIS section as far west as the ships did (Figures 4.3). AW in 2013 is similarly towards the cool end of the interannual range, but is of intermediate salinity; CAW in 2013 is particularly cold, but is of an intermediate salinity (Figure 4.5).

Profiles that do not contain either SCW or FIC water – e.g. in June and October when the dominant feature is a change in temperature that is not accompanied by the freshening signal that indicates mixing with SCW (Figure 4.5B) – are from the eastern JONSIS section; this signal is not present in the glider observations because the glider primarily occupied the central portion of the JONSIS section (Figure 4.3). It is the influence of this warm water mass – potentially the influence of NCC water (Sætre et al., 1988) – that appears to be the reason why FIC water does not lie on a mixing line between SCW and AW. The low-salinity signal of SCW is also apparent in the spring and summer (i.e. March and June; Figure 4.5B). CAW in the spring and summer, as in October and November, is the coldest water mass present at the JONSIS section. This is the case even when, in March, SCW, FIC water and AW are all colder than 8°C. However, in some instances CAW in March is warmer than at other times of year, which is likely a consequence of heat from above the thermocline being mixed down to lower depths as stratification decays.

4.3.2 Influence of tidal mixing on water mass properties

The glider observations presented above reveal that there is great variability in water mass composition and distribution at the JONSIS section in autumn (Figures 4.4 and 4.5), a consequence of the diverse regions from which the inflowing water masses originate. A consequence of this variability is that FIC water is not always observed to be the vertically well-mixed strip of water that previous studies have reported (e.g. Chapter 2; Dooley, 1974; Turrell et al., 1990, 1992). Occupations six and seven present what are perhaps the best examples of the traditional view of the FIC, but in other occupations there is horizontal and vertical variability such that no comparable strip of FIC water is present (Figure 4.4). This lack of a spatially coherent, temporally persistent strip of FIC water at the JONSIS section could be because the section is still within the region of intense tidal mixing around the FIG. Turrell et al. (1992) observed a vertically well-mixed and coherent FIC some distance south of the JONSIS section; indeed, they report changes in the temperature-salinity characteristics of the FIC between sections to the west of the FIG (i.e. upstream of JONSIS) and a section further south in the North Sea (i.e. downstream of JONSIS). In addition, Turrell et al. (1990) report entrainment of

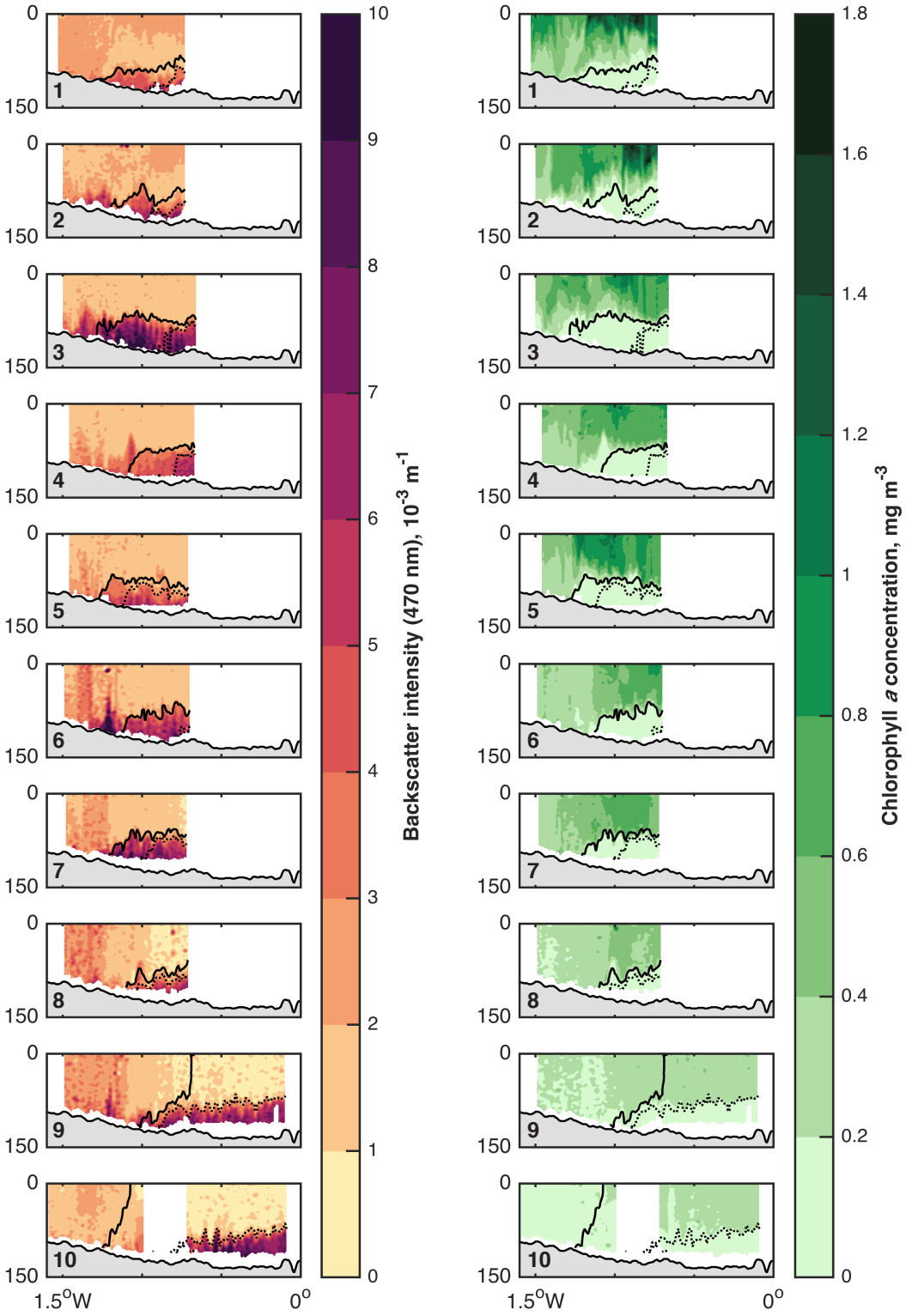

Figure 4.6 Backscatter intensity (left-hand side; 10^{-3} m $^{-1}$) and chlorophyll *a* concentration (right-hand side; mg m^{-3}). The 1027.2 kg m^{-3} isopycnal (solid line) and 1027.4 kg m^{-3} isopycnal (dotted line) are plotted. Occupation number is in the bottom left of each panel.

oceanic and shelf water masses into the FIC as it passes through the FIG. The proximity of the observations to the region of mixing may make the appearance of the FIC as a coherent water mass unlikely: such a feature may more frequently emerge downstream, further into the North Sea.

Another potential reason for the lack of a coherent, vertically well-mixed strip of FIC water at the JONSIS section is that, despite the previously reported intensity of tidal mixing in the vicinity of the FIG and the Scottish coast (Svendsen et al., 1991; Turrell et al., 1992; Sheehan et al., 2018), full-depth tidal mixing is not predicted to occur at those parts of the JONSIS section sampled by the glider at the beginning of the deployment. The region of full-depth tidal mixing is expected to be confined to longitudes west of approximately 1.5°W during the first three occupations (Chapter 3), which may explain why the eastward extensions of SCW occur at the surface. The evolution of tidal mixing can be seen in the backscatter intensity and chlorophyll distributions (Figure 4.6). As the greatest backscatter intensity is observed at the seafloor (Figure 4.6), we conclude that this represents the signal of resuspended sediment stirred up from the seafloor by the currents. There is no apparent relationship between water mass distribution and backscatter intensity, nor is there an apparent relationship between DAC velocity and backscatter intensity. An interesting feature of the observations is that depth-mean backscatter intensity (not shown) is, in general, constant across the section: no portion of the section exhibits backscatter intensity that is consistently higher or lower than other portions. The amount of sediment being stirred up into the water column is therefore fairly constant across the section. In the first five occupations, backscatter intensity decreases with depth, with the 1027.2 kg m^{-3} isopycnal frequently acting as a barrier between turbid waters below and relatively clearer waters above (Figure 4.6). In occupations six and subsequently, two regimes emerge. In the west of the section, moderate backscatter intensities are observed. In contrast, in the east of the section the distinction between high-turbidity bottom waters and low-turbidity surface waters is maintained (Figure 4.6). In occupations nine and 10, as the 1027.2 kg m^{-3} isopycnal shoals, outcrops and retreats westward, the boundary between high- and low-turbidity waters is instead marked by the 1027.4 kg m^{-3} isopycnal. The eastward advance of full-depth tidal mixing (Chapter 3) would explain these observations, bringing suspended sediment to the surface in the expanding mixed zone and tending to even out sediment concentration in the fully mixed region.

Aspects of the chlorophyll distribution are the inverse of the backscatter intensity distribution and similarly imply that full-depth mixing spreads eastwards across the section as the deployment progresses. Waters with high chlorophyll concentrations have low backscatter intensity and vice versa (Figure 4.6). This also suggests that phytoplankton assemblages are not unduly affecting the backscatter intensity distribution, confirming the interpretation of the backscatter intensity as representing suspended sediment concentration. In the first three occupations, with full-depth tidal mixing expected to be confined to the west of the section, high chlorophyll concentrations are observed at the surface, especially to the east of 1°W (Figure 4.6). There

is a gradual decline in chlorophyll concentration at all longitudes over the deployment, but the decline is particularly pronounced to the west of the section from occupation six onwards as full-depth tidal mixing becomes established there. Chlorophyll concentrations at the surface in the more stable eastern part of the section remain higher (e.g. occupations six, seven and eight in Figure 4.6), probably because the stability of the water column is such that they spend enough time in the euphotic zone – the high-light surface region of the water column – to survive. As with backscatter intensity, there is no clear relationship between chlorophyll concentration and water mass distribution, although the very highest chlorophyll concentrations are observed during the first two occupations in regions of mixed SCW and FIC water (Figure 4.6). This implies that phytoplankton growth is not nutrient limited, but is instead limited by light availability and stratification.

Our glider observations reveal more temporal and spatial variability in the hydrography of the northwestern North Sea than has been captured by previous observational campaigns (e.g. Turrell et al., 1992). The region hosts diverse and markedly different water masses of clear coastal and oceanic origin. The distribution of these water masses changes considerably on weekly time scales and responds quickly to changes in the density distribution brought about by the decay of seasonal stratification. The evidence of variability presented here adds to the challenge of managing the North Sea, especially as posed by the EU's MSFD, as the natural state of the region – i.e. without human influence – may be harder to define in the face of such variability. It also adds greater importance to the study of mixing in the region. Intense tidal mixing is known to occur in the FIG and at the western portion of the JONSIS section (Chapter 3): the hydrographic result of this mixing could potentially change considerably, with attendant consequences for the hydrography of the wider North Sea basin, as water masses of such markedly different properties are advected in and out of these mixing hotspots. These results also have implications for future observations of the northwestern North Sea. Using standard longitudes and depths to define the characteristics of water masses is a common technique – for instance, the bottom 50 m of water in the six eastern-most stations on Scottish occupations of the JONSIS section (i.e. stations east of 1.5°W; Figure 2.1C) are assumed to sample CAW (e.g. Turrell et al., 1996). However, the results presented above (Figure 4.4) demonstrate the possible flaws in this technique: it has the important advantages of simplicity and consistency, but the spatial variability that is apparent our glider observations increases the uncertainty that is attached to such spatially invariant water mass definitions. Approaches that account for the changing distribution of water masses over time would likely yield more accurate results.

4.4 Velocity and transport

DAC flow across the JONSIS section is predominantly southward, i.e. into the North Sea (Figure 4.7). The tendency for the flow to be south-southwestward is in agreement with the finding

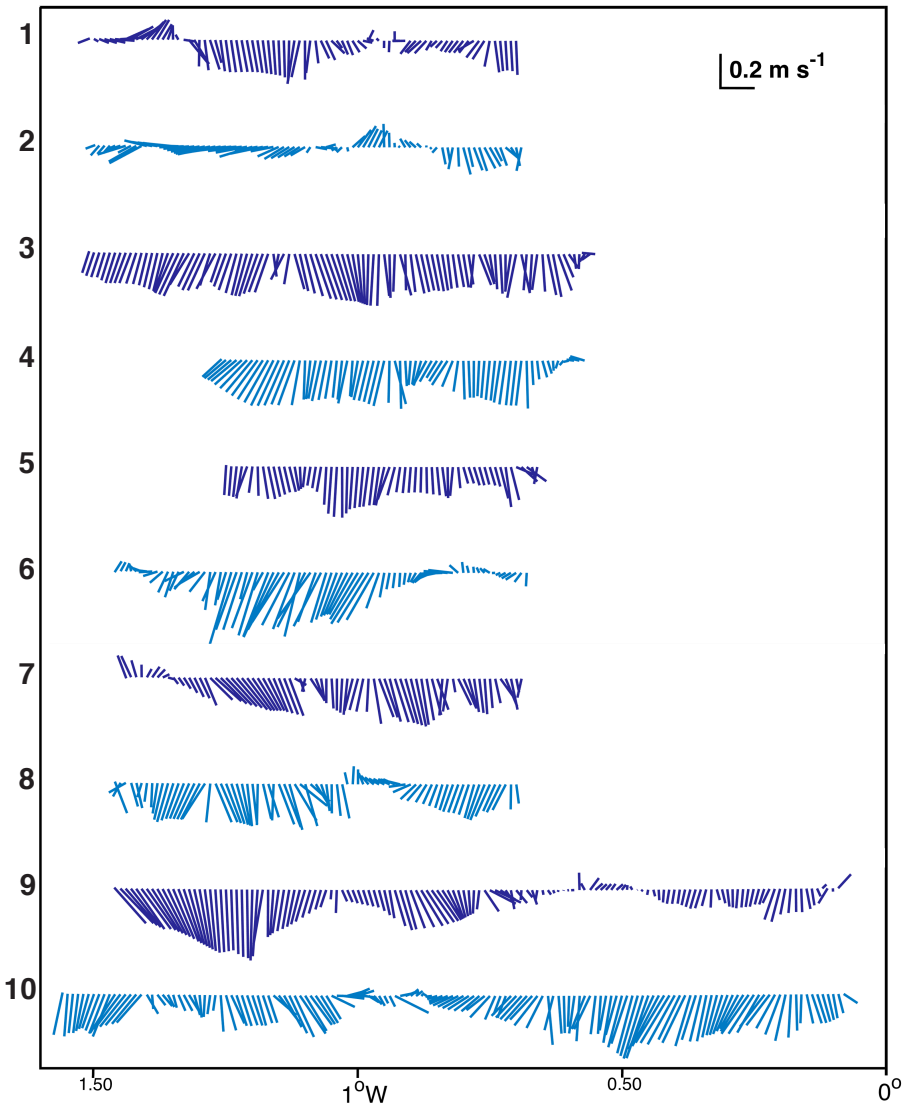

Figure 4.7 DAC observations, de-tided, projected onto the JONSIS section along meridians and gridded by occupation.

that, within the North Sea, the FIC tends to follow the 100 m isobath, which crosses the JONSIS section from south-southwest to north-northeast at approximately 1.4°W (Figure 4.3A). However, periods of coherent south-southeastward flow, and of northward flow, suggest that the inflows are not wholly tied to bathymetry. The mean meridional velocity is -0.13 m s^{-1} (negative velocity indicates southward flow). The mean zonal velocity is -0.01 m s^{-1} (negative velocity indicates westward flow, i.e. towards the Orkney Islands). A mean westward flow, albeit a small one, at the JONSIS section is an interesting result given the proximity of the section to the FIG, through which the velocity of the FIC must be orientated eastward in order for inflow to be maintained. Consequently, either zonal flow through the FIG was weak during the glider deployment, or else the turning angle of the FIC once it enters the North Sea must be fairly sharp.

Thermohaline velocity across the JONSIS section is commonly focused into some four to six narrow, southward-flowing jets with a characteristic width of between approximately 10 km (Figure 4.8). The fastest of these jets have peak surface velocities in excess of 0.3 m s^{-1}, although the majority have peak surface velocities of between 0.2 and 0.3 m s^{-1}. The majority of these jets are southward flowing and are associated with upward tilt of the isopycnals towards the east (i.e. bottom-left to top-right in Figure 4.8), which is particularly pronounced where the 1027.2 kg m^{-3} isopycnal meets the sea floor. It is possible that the narrow, southward thermohaline jets, coupled with the presence of dense AW and CAW at the east of the section (Figure 4.4), present a meridional barrier to the FIC as it enters the North Sea through the FIG, at which point its velocity must have a considerable zonal component. Such a density-velocity barrier could limit eastward flow in the FIC and cause it to effect the hypothesised sharp turn to the south. The dynamical importance of CAW to circulation in the northern North Sea has previously been hypothesised (Turrell et al., 1992; Hill et al., 2008). In some occupations, there are also northward-flowing jets (e.g. occupations two and eight), which are associated with upward tilt of the isopycnals towards the west (i.e. bottom-right to top-left in Figure 4.8). While southward-flowing jets are present in all 10 occupations, northward-flowing jets are not. The growth and decay of these northward-flowing jets appears to be related to short-lived, wave-like perturbations in the depths of the isopycnals with amplitudes of up to 20 m. Such narrow jets have not been previously observed in the northwestern North Sea: they are not apparent in thermohaline velocity sections derived from coarsely spaced ship observations from standard stations along the JONSIS section (Figure 2.1), either when considered as seasonal means (Figures 2.3 to 2.6; Sheehan et al., 2017) or as individual occupations (not shown); neither has their width been determined from studies of current meter observations (e.g. Turrell et al., 1990). This new result, made possible by the high spatial resolution of glider data, refines our knowledge of the circulation of the region and has implications for the transport of tracers and organisms at times of year when thermohaline flow dominates in the northwestern inflows – i.e. in summer (Dooley, 1974; Turrell, 1992; Turrell et al., 1992).

The absolute velocity (i.e. geostrophic shear referenced to the glider's DAC observations; Figure 4.7; Section 4.2) is strongly influenced by the addition of non-thermohaline flow that is captured by the DACs (Figure 4.8). In the main, the addition of non-thermohaline flow increases southward velocity across the section, although non-thermohaline flow can work against thermohaline flow and retard absolute flow where strong thermohaline flow is present (e.g. occupation two). Maximum absolute velocities are comparable to maximum thermohaline velocities, but the absolute flow does not tend to occur in narrow jets. In some occupations, the thermohaline jets are visible in the absolute velocity distributions – for instance, in occupations five and six (Figure 4.8) – but these jets are not the dominant features of the absolute velocity distributions. Instead, absolute flow across the section occurs in much broader bands approximately 20 to 60 km wide. Features such as surface winds that force non-thermohaline flow therefore occur over larger spatial scales than the density gradients that force thermohaline

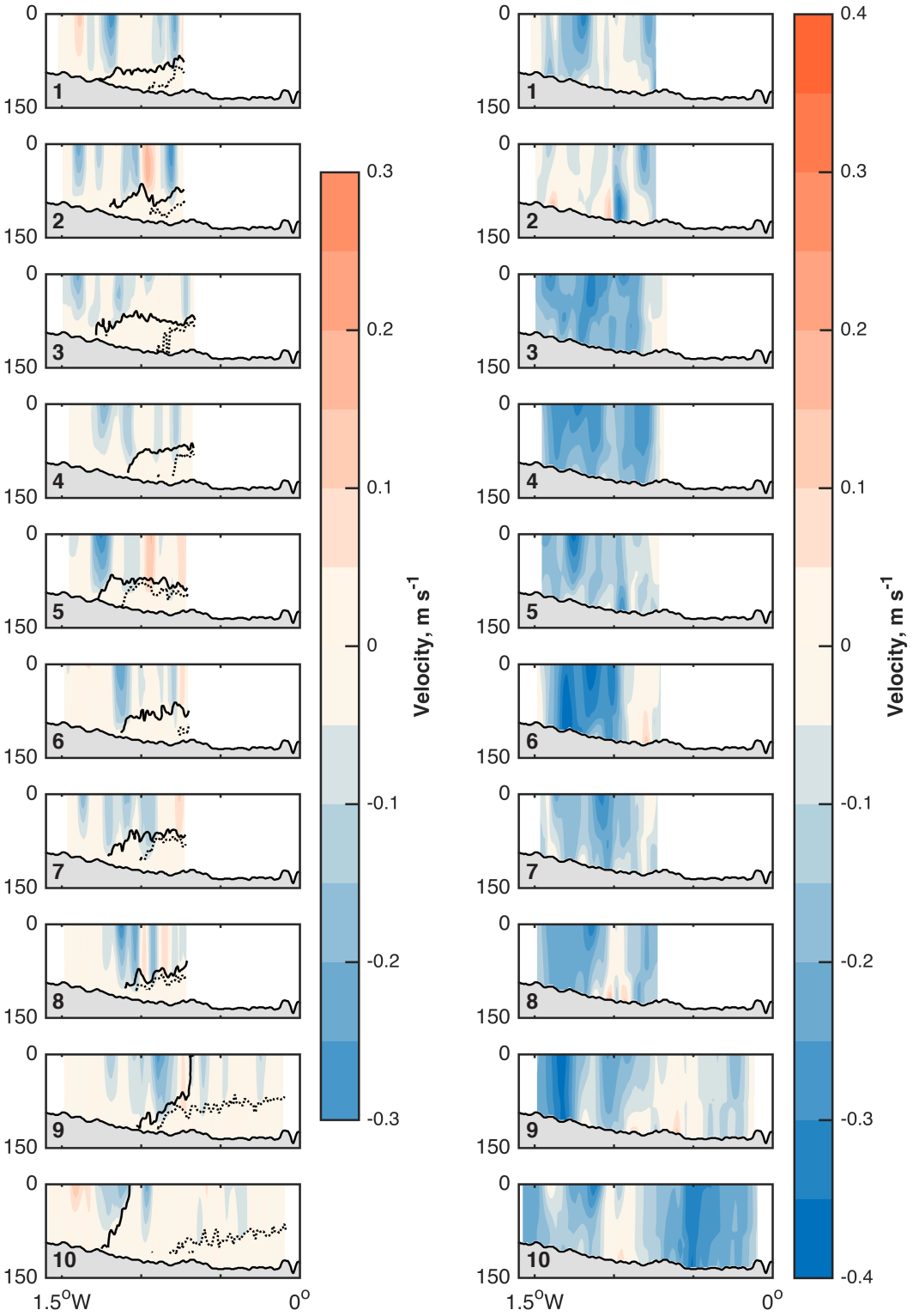

Figure 4.8 Meridional thermohaline (left-hand side) and absolute (right-hand side) velocity (m s^{-1}). Negative velocities indicate southward flow. Tidal flows are excluded. The 1027.2 kg m^{-3} isopycnal (solid line) and 1027.4 kg m^{-3} isopycnal (dotted line) are plotted (left-hand side only). Occupation number is in the bottom left of each panel.

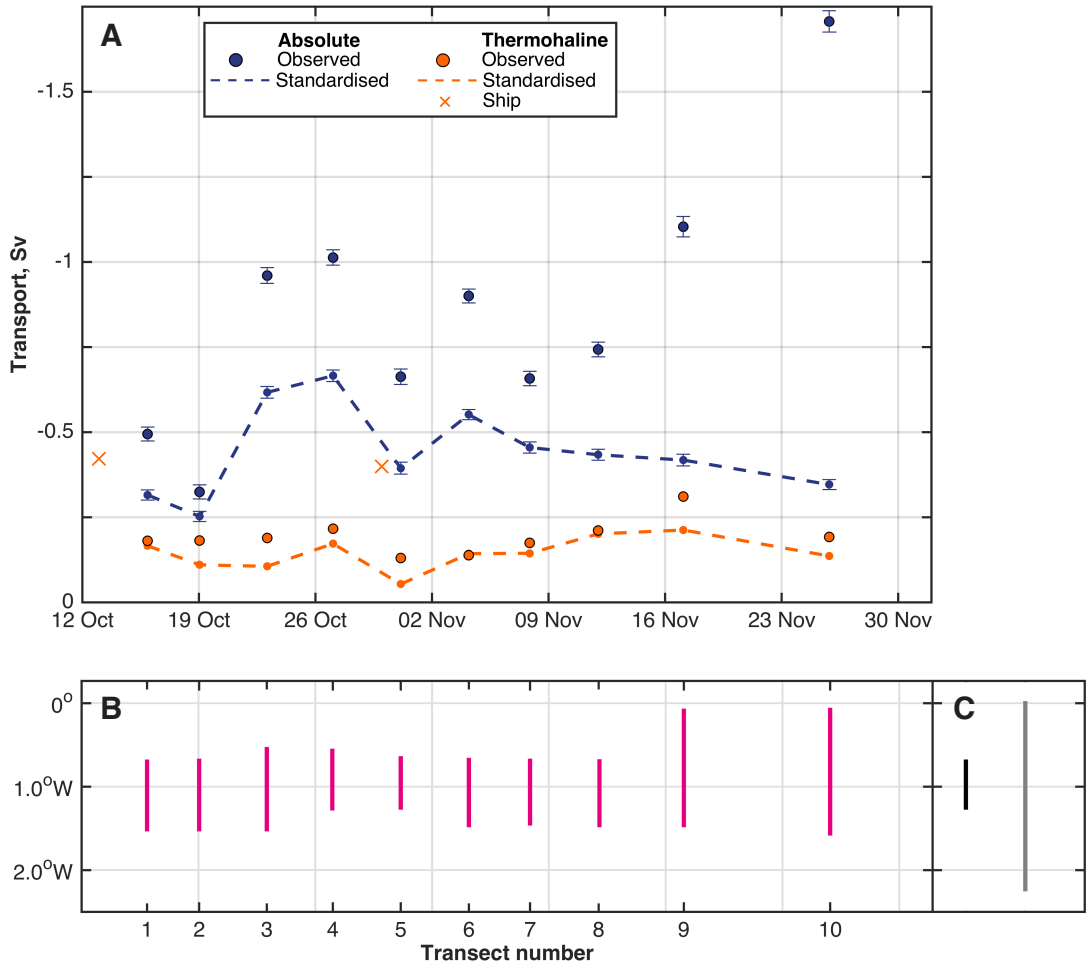

Figure 4.9 **A** Absolute (blue) and thermohaline (orange) volume transport (Sv). Circles indicate full-width transport in each occupation; dashed lines indicate transport across the standardised section; crosses indicate thermohaline transport from ship-based observations of the full JONSIS section (Chapter 2). Error bars indicate $\pm$ one standard deviation, derived from Monte Carlo error estimation (Section 4.2).Note that the y axis has been reversed. **B** Pink lines indicate the portion of the JONSIS section sampled by the glider in each occupation (pink lines). **C** The standardised section: the part of the JONSIS section sampled by the glider in all 10 occupations (black line) and the full JONSIS section (grey line).

flow.

The horizontal structure of absolute velocity changes in time (Figure 4.8). In some occupations, there is southward flow across full width of the section (e.g. occupations three and four), whereas in other occupations there are two regions of strong southward flow separated by a region of near-zero flow (e.g. occupations eight, nine and 10). This is possibly evidence of the separation of the northwestern inflows, the FIC being the western portion of the inflow and the ESAI being the eastern portion of the inflow; this would agree with current meter observations from further south in the northwestern North Sea that reveal the presence of two separate southward flows (Turrell et al., 1992). However, the limited widths of the glider occupations do

not allow us to determine with any certainty whether the inflows are sometimes joined (e.g. occupations three and four) and sometimes separate (e.g. occupations nine and 10), or whether the inflows are always separate.

The considerable barotropic contribution to velocity is apparent in the transport values for each occupations: absolute geostrophic transport for each occupation is higher than the thermohaline transport (Figure 4.9A). The size of this difference means that descriptions of the northwestern inflows based on thermohaline transport alone (Chapter 2) will be of limited utility, at least during the autumn. The hypothesised annual cycle in the forcing of the northwestern inflows – that is, density-driven in summer and wind-driven in winter (e.g. Chapter 2; Dooley, 1974; Turrell, 1992) – means that the thermohaline transport, which reaches a maximum of 0.35 Sv (Figure 2.9; integrated across the entire JONSIS section) in October, likely represents a greater proportion of the absolute transport in summer than it does in winter.

Absolute transport is more variable than thermohaline transport (Figure 4.9A). For example, absolute transport across the standardised section increases from 0.25 Sv in occupation two to 0.75 Sv in occupation three. The increase is even greater when comparing the full-width transports for occupations two and three – note that the occupations are of a similar width (Figure 4.9B). A large increase in absolute transport across the full-width sections iss observed between occupations nine and 10, which are also of a similar width (Figure 4.9B). The thermohaline component of transport changes less markedly over time, showing no evidence of the single-section peaks and troughs that are found in the absolute transport time series. This appears to be in agreement with results presented in Chapter 2 which show that variability in the thermohaline transport across the JONSIS section is predominantly explained by its annual cycle (Figure 2.9). The majority of the variability in absolute transport across the JONSIS section is therefore driven by non-thermohaline processes.

The zonal movement of the FIC and ESAI across the section and proportion of the region of limited flow that separates them which covers the standardised section, is seen to affect the absolute transport time series. Occupations nine and ten provide a good example of this. The full-width absolute transport in occupation 10 is greater than in occupation nine, but the standardised absolute transport in occupations 10 is less than in occupation nine (Figure 4.9A): this is because the region of low-velocity that separates the FIC and the EASI is located in the standardised section in occupation 10, but is located to the east of the standardised section in occupation nine. This demonstrates a key limitation of using the standardised section to compare transport from occupation to occupation. While any hydrographic section that covers only part of a shelf sea or ocean basin will inevitably miss some proportion of the total transport, the standardised section that may be constructed from the glider occupations is too short to cover the full range of longitudes commonly occupied by the northwestern inflows. Consequently, changes in transport through the standardised section signify both changes in the transport of the inflows and, potentially, changes in the location of the inflows. This is a major source of uncertainty in the transport of the northwestern inflows. Thermohaline transport es-

timates calculated from contemporaneous ship occupations that sampled the full width of the JONSIS section are higher than thermohaline transport estimates from the glider occupations (Figure 4.9). They give an indication of the amount of thermohaline transport missed by the glider estimates. DAC-derived transport uncertainties are very small relative to the calculated transport values (Figure 4.9A). Transport uncertainty arising from uncertainty in DAC observations is small; importantly, the magnitude of changes in transport from one occupation to the next is considerably greater than the magnitude of the uncertainties themselves (Figure 4.9A).

More reliable estimates of transport across the JONSIS section could be produced by referencing geostrophic shear calculated from ship surveys along the entire JONSIS section – or along the Orkney-Ustire section, which covers the full width of the North Sea basin (Chapter 2) – to surface velocities derived from, for instance, the GlobCurrent programme (Rio et al., 2016). Alternatively, two or more gliders could be deployed simultaneously in a single campaign, which would allow for greater coverage of the section.

4.5 Non-thermohaline forcing

4.5.1 Wind forcing

We use the glider's de-tided DAC time series to examine the influence of wind forcing on the northwestern inflows. Wind reanalysis data for the northwestern North Sea and Faroe-Shetland Channel region are taken from the ERA Interim reanalysis product (Dee et al., 2011). The correlation between the time series of daily-mean DAC velocity and the daily-mean wind velocity at each point on the ERA Interim grid (0.75° resolution in latitude and longitude) was calculated using the vector correlation method of Kundu (1976, see also Box 4.1 on page 68). The method produces a correlation coefficient, R_{vcorr}, and an angle of offset, θ_{vcorr}, that quantifies the mean rotation of the two time series relative to one another (Figure 4.10). The significance of the correlation was estimated. Because of auto-correlation in the two time series, the autocorrelation time scale was calculated; the degrees of freedom required to estimate the significance is the number of autocorrelation time scales that fit into the length of the time series. The degrees of freedom of the wind vector time series is calculated at each point on the ERA Interim grid: at each grid point, we use the smallest degrees of freedom to calculate significance, whether it pertains to the DAC or the wind. The position of DAC observations was not considered. Regions where the vector correlation is not significant at the 5% level are masked in Figure 4.10.

High vector correlations ($R^2_{vcorr} > 0.3$) between the wind and DAC time series are found over the northern United Kingdom and the Orkney Islands, and extend into the central Faroe-Shetland Channel and the central FIG (Figure 4.10). Of principal interest are high correlations over water. The region of high correlation does not extend far east into the northern North Sea; generally east of the prime meridian the vector correlation is not significant (Figure 4.10). This

BOX 4.1 Vector correlation

The vector correlation method of Kundu (1976) quantifies the similarity, once the mean has been removed, between two sets of vectors using two coefficients, which in this thesis are labelled R_{vcorr} and θ_{vcorr}. The first of these, R_{vcorr}, is comparable to the correlation coefficient, R, used in normal correlation: a value of $\pm$ 1 represents perfect correlation (positive or negative) and a value of zero represents no correlation. The value of R_{vcorr} is not affected by multiplication of a vector time series by a common scale factor, neither is it affected by rotation of one vector time series relative to another other by a constant angle. Therefore, two time series of the form:

$$(m, \theta) = (\alpha m, \theta + \beta)$$

where m is the magnitude, θ is the angle a vector makes with the x axis, and α and β are constants, will return a vector correlation coefficient, R_{vcorr} of one.

The second of the vector correlation coefficients quantifies the average rotation, in degrees, of one set of vectors relative to the other. In the above example, θ_{vcorr} will be equal to the scale factor β. A positive value indicates positive (i.e. anticlockwise) rotation; a negative value indicates negative (i.e. clockwise) rotation. The following is an idealised example:

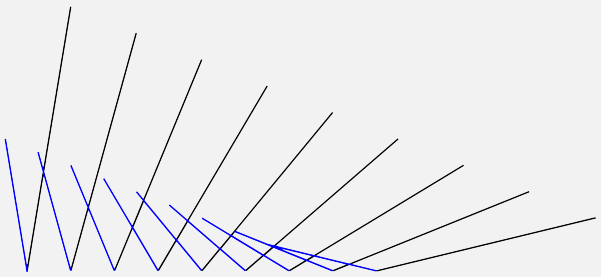

The u components of the black vectors increase from left to right from 5 to 10 units in increments of 1 unit. The v components of the black vectors decrease from left to right from 10 to 5 units, also in increments of 1 unit. The u and v components of the blue vectors are half the magnitude of, respectively, the u and v components of the black vectors. In addition, the u component of the blue vectors has been reflected in the y axis. The R_{vcorr} of these sets of vectors is 1.0; the θ_{vcorr} value is 90°. Were, for example, the v component of the blue vectors to be reflected in the x axis the θ_{vcorr} would be 180°; the R_{vcorr} would remain 1.0.

result implies that wind stress to the west of the FIG acts to “push” Atlantic water into the North Sea, rather than wind stress to the east of the FIG acting to “pull” water in. The region of high vector correlations covers several important features. Around the northwestern coast of the United Kingdom is found the fresh SCW that is observed at the western end of the JONSIS section (Dooley, 1974; Turrell et al., 1992); flowing northward approximately along the shelf break (Figure 4.10) is the ESEC (Figure 1.1), which separates shelf waters from those of the open ocean (Souza et al., 2001); and to the west of the shelf break are the high-salinity waters of the northern Atlantic. The region around the small, uninhabited island of Rona (Figure 4.10) has been identified as a site of potential mixing between Atlantic waters and SCW that could prove to be the source of the FIC (Turrell et al., 1992). Our results suggest that the velocity of the FIC inside the North Sea is being influenced by wind stress in this potential source region. Furthermore, within this region of greatest wind influence are found the SCW and AW water masses observed in the northwestern North Sea, both in this study (Figures 4.4 and 4.5) and

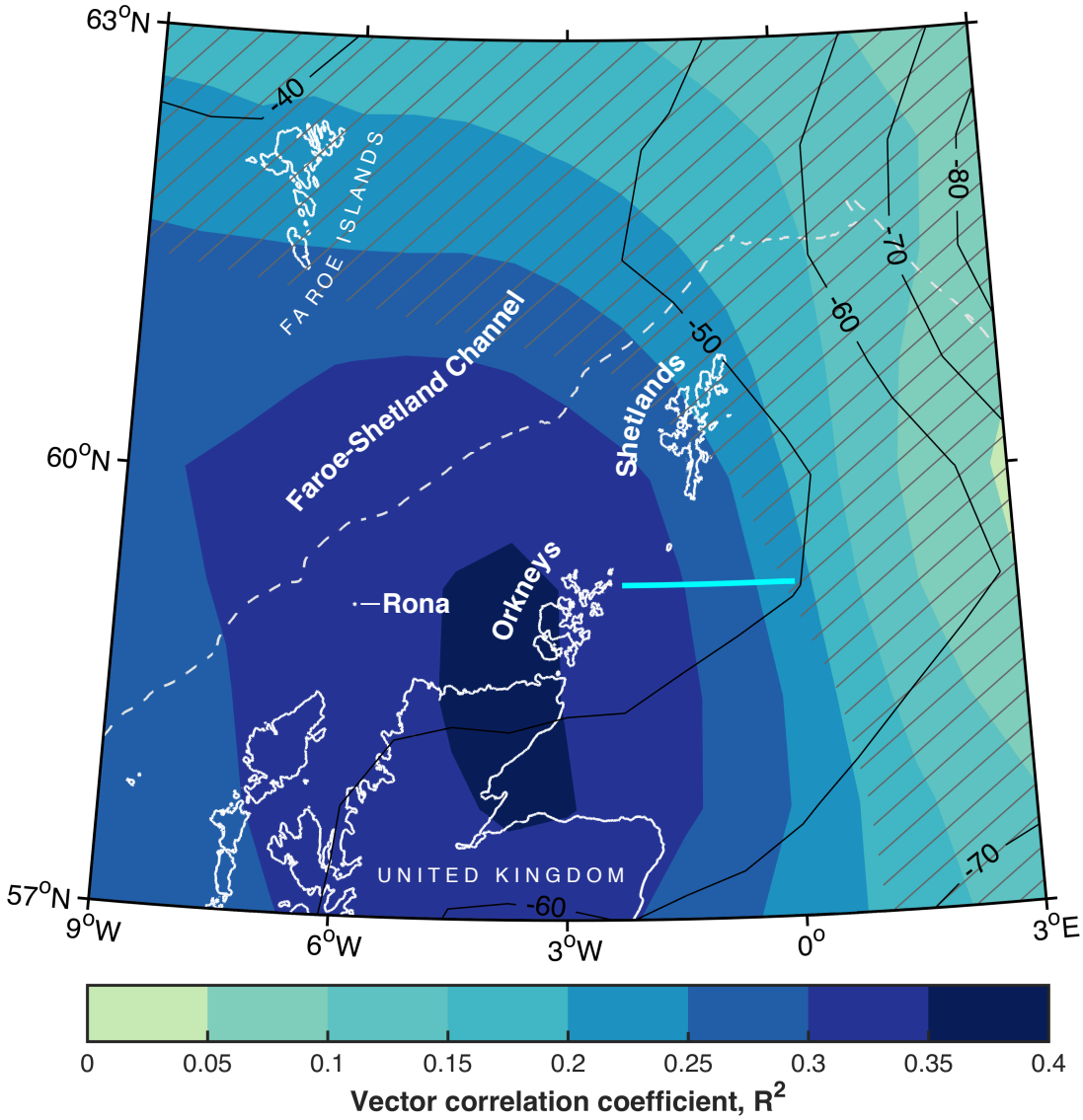

Figure 4.10 Map of squared vector correlation coefficients, R^2_{vcorr} (colour shading), and offset angles, θ_{vcorr} (contours), between the DAC and wind time series. Hatching covers the region where the vector correlation is not significant at the 5% level. The coastline is shown in by the solid line; the shelf break, represented by the 200 m isobath, is shown by the dashed line; the JONSIS section is shown in cyan.

previously (Dooley, 1974; Turrell et al., 1992).

The average angular offset between the wind and DAC time series in the region of high correlation is between -40 and -50° (Figure 4.10), the minus sign indicating that the DAC is negatively rotated (i.e. clockwise) relative to the wind. These angular offsets (Figure 4.10) indicate that the wind is most likely to promote purely southward flow across the JONSIS section when blowing from the northwest; the wind is most likely to promote purely eastward flow through the FIG when blowing from the southwest. This result is not dissimilar to those of previous studies. Winther and Johannessen (2006) report that strong westerly winds promote high transport in the northwestern inflows. In particular, Turrell et al. (1990) report that, in the

presence of North Sea stratification, flow in the northwestern inflows is enhanced by winds from the north. That the angular offsets are negative suggests that flow forced by wind stress is influenced by the Coriolis effect; however, the fact that the that the angular offset is less than 90° suggests that Ekman transport is not the primary driver of the inflows. This could be because the Ekman layer is either deeper or shallower than the depth of the water column. For a given wind speed, s (m s^{-1}), the Ekman depth, D_E (m) is given by:

$$D_E = \frac{4.3s}{(sin\theta)^{1/2}} \tag{4.2}$$

where θ is latitude (Pond and Pickard, 1983). Within the domain shown in Figure 4.10, the mean wind speed is 8 m s^{-1}, which would result in an Ekman depth of 37 m. For a representative high wind speed (20 m s^{-1}), the Ekman depth is 93 m; for a representative low wind speed (3 m s^{-1}), the Ekman depth is 14 m. It is therefore most likely that wind influence is felt in the surface layer and does not reach the sea floor. Consequently, the limited influence of wind forcing on DACs appears to be partly because wind forcing sets up a two-layer flow structure: a wind-driven surface Ekman layer sits above a non-Ekman layer at the sea floor.

The vector correlations over the region around Rona may be statistically significant, but with maximum correlations of between 30 and 35% (Figure 4.10), wind variability in this region does not explain a majority of DAC variability at the JONSIS section on daily time scales. Instead, it would appear that wind forcing has a moderating effect on the northwestern inflows on daily time scales. The limited influence of wind on flow is further apparent from a visual comparison of DAC vectors (Figure 4.7) and occupation-mean wind vectors (Figure 4.11): occupation-mean wind varies considerably in strength and direction over the course of the glider deployment, but flow remains predominantly southward. The most pronounced example of wind influence on the northwestern inflows appears to be occupation two, when strong easterly wind over the region of maximum wind influence (Figure 4.11) appear to be responsible for a significant retardation of the northwestern inflows (Figures 4.7, 4.8 and 4.9); however, even under these conditions, which appear to be least conducive to inflow, southward transport is sustained (Figure 4.9).

If thermohaline jets and the presence of dense patches of AW and CAW are controls on the path of the FIC and ESAI within the North Sea (Section 4.4), they may also act to dampen the response of the FIC and ESAI to wind forcing. Thermohaline transport does not make a large contribution to the absolute transport during the glider deployment (Figure 4.9A), but the presence of stratification that drives thermohaline transport (Figures 4.4 and 4.8) may be expected to enhance a two-layer structure set up by the wind. It is already known that the FIC and ESAI respond more slowly to wind forcing when stratification is present than when it is absent (Turrell et al., 1990, 1992), and that stratification precludes a barotropic response to wind forcing (Turrell et al., 1992). The presence of stratification also limits the correlation between flow in the FIC on either side of the Orkneys, which is high only when stratification is absent (Turrell et al., 1990). It is possible that the direction of the FIC and

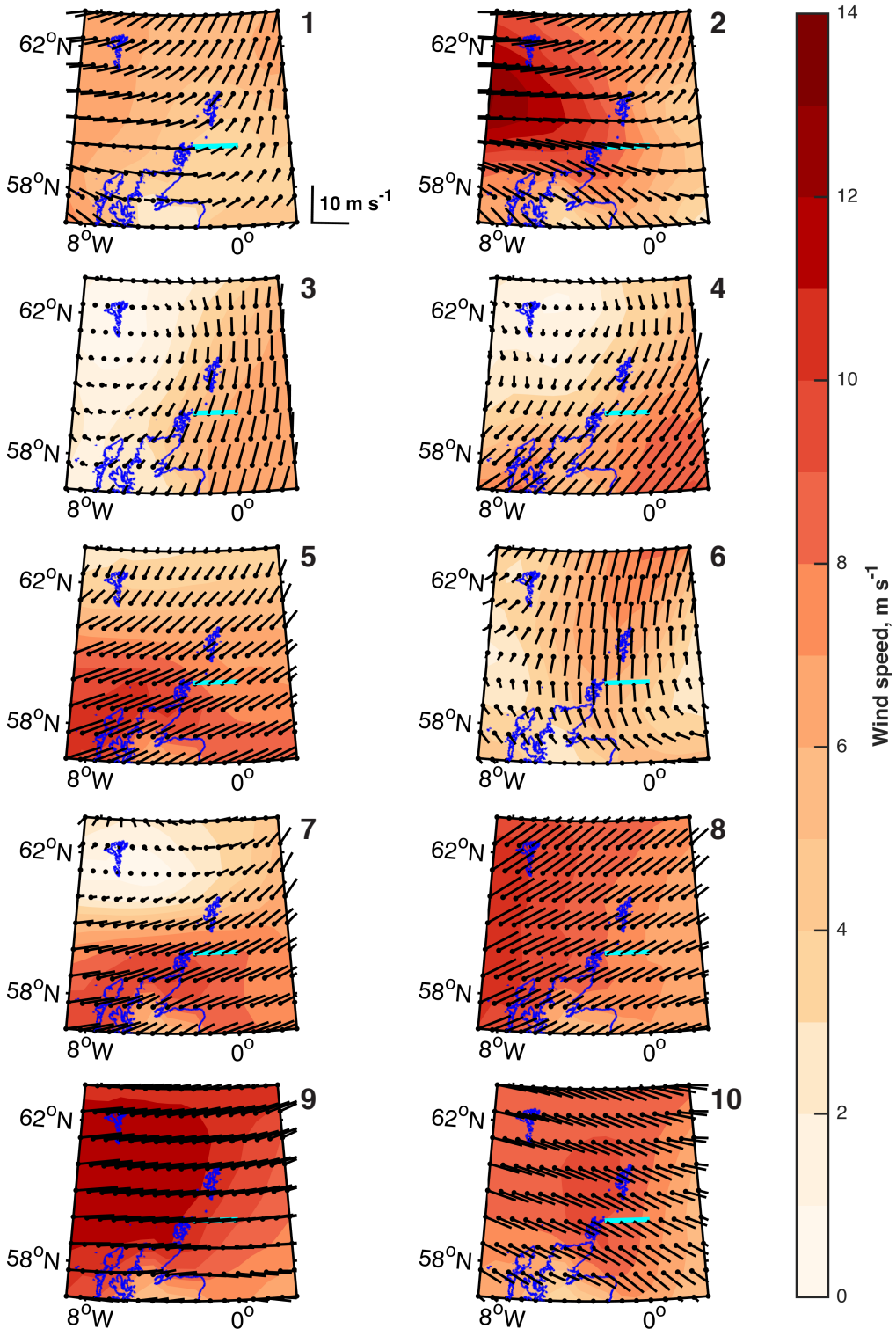

Figure 4.11 Maps of occupation-mean wind vectors (m s^{-1}). Vector size is indicated by the key to the bottom right of subplot 1. The origin of each vector is indicated by a black dot. Shading indicates wind speed (m s^{-1}). The coastline is shown in blue and the the JONSIS section is shown in cyan. Occupation number is in the top right of each subplot. A key is shown to the bottom right of panel one.

ESAI is less responsive to wind forcing when the inflows are partially under the influence of strong thermohaline jets (Figure 4.8): specifically, southward thermohaline flow may increase the tendency of the FIC and ESAI to flow southward even when wind conditions would be expected to promote flow in another direction. The finding that wind plays only a moderating role in the forcing of the northwestern inflows is in contrast to studies that report a strong link between wind forcing and flow in the northwestern North Sea on daily to weekly (e.g. Turrell et al., 1990; Winther and Johannessen, 2006).

The relatively small size of the study area may also influence the strength of the correlation between wind variability and current variability. Studies investigating the influence of wind on North Sea circulation commonly examine the entire basin (e.g. Winther and Johannessen, 2006; Mathis et al., 2015). It is possible that the strength of the northwestern inflows is influenced by wind forcing and the associated response over the entire North Sea basin. For instance, Furnes (1980) finds that steady and homogeneous winds blowing from the north and west tend to drive an anti-clockwise circulation in the North Sea, which would imply stronger flow in the northwestern inflows; and that winds blowing from the south and east tend to drive a clockwise circulation in the North Sea, which would imply weaker flow in the northwestern inflows. A stronger relationship between wind forcing and flow over the whole North Sea basin than over an individual current system that represents just a part of the basin-scale circulation would imply that wind forcing of North Sea currents operates on the spatial scales of the entire basin (100s km), rather than on the spatial scale of an individual current (10s km).

4.5.2 Oceanic forcing

In addition to wind forcing, open-ocean processes in the northern Atlantic can exert an influence on the northwestern inflows (Huthnance, 1997; Holt and Proctor, 2008; Huthnance et al., 2009; Marsh et al., 2017). Marsh et al. (2017) find relationships between sea-surface height differences across key sections – across the FSC, for example – and inflow to the North Sea. We find no significant relationship between daily-average DAC velocity and daily-averaged sea-surface height differences across the Faroe-Shetland Channel, the FIG and the Orkney-Utsire section, the extension of the JONSIS section that crosses the entire North Sea. Sea-surface height observations were downloaded from the Copernicus Marine Environment Monitoring Service[5]. This is probably because the time lag between changes in sea-surface height forcing and the response of the northwestern inflows is greater than two months, i.e. the length of the glider occupation. The relationships reported by Marsh et al. (2017) are derived from multi-year time series.

Holt and Proctor (2008) run a numerical model simulation of the northwestern European continental shelf with only oceanic forcing at the model margin. They find that ocean- and wind-driven currents occur in similar locations, and that both oceanic and wind forcing produce

[5]www.copernicus.eu, date set: DATASET-DUACS-REP-GLOBAL-MERGED-ALLSAT-PHY-L4-V3

currents of a comparable spatial scale. However, the ocean-driven currents are less variable in time than the wind-driven currents. Furthermore, ocean-driven flow is more consistently into the North Sea (i.e. predominantly southward across the JONSIS section): unlike wind and thermohaline forcing, oceanic forcing seemingly lacks the capacity to reverse the direction of the FIC and ESAI. Importantly, they calculate that the ocean-driven component of the northwestern inflows, when examined seasonally, is commonly responsible for more transport than either the wind-driven or thermohaline components. The results of Holt and Proctor (2008) assist in the interpretation of our glider observations. The presence of a steady, inflowing, ocean-driven component to the FIC and ESAI could combine with the thermohaline jets and dense pools of bottom water observed by the glider (Figures 4.4 and 4.8) to limit the influence of the wind, even as stratification decays (Figures 3.4 and 4.4; Chapter 3) and thermohaline dynamics become less significant.

The temporal and spatial scales on which oceanic forcing influences the northwestern inflows appear to be greater than those which may be examined from our glider observations, which are more suited to an analysis of the thermohaline and wind forcing of the northwestern inflows. Nevertheless, the generally fairly southward nature of the inflows and the moderate sensitivity of the inflows to wind forcing, would appear to be consistent with a prominent role of oceanic forcing in influencing flow into the North Sea.

4.6 Summary

Physical and biogeochemical observations from a two-month glider deployment at the JONSIS section have been analysed to describe the hydrographic properties and volume transport of the FIC and ESAI in the age of high-resolution oceanography. Water mass characteristics are consistent with previous descriptions of hydrography in the northwestern North Sea, but it is clear from our observations that the spatial distribution of key water masses – of fresh SCW and saline AW in particular – is highly variable in time. This result, coupled with the observation that the region of full-depth tidal mixing advances eastward with the autumn decay of stratification, is likely of ecological significance and should inform management decisions. Furthermore, existing regional time series that rely on strict definitions of depth and longitude to quantify the properties of water masses should, in future, be evaluated in light of this variability.

The horizontal temperature and salinity gradients across the section give rise to thermohaline jets, the majority of which are southward and which tend to be associated with the eastward-upward tilt of the isopycnals over AW and CAW intrusions. Thermohaline flow is appreciable even as stratification decays. The existence of thermohaline flow in the northwestern inflows has been long established (e.g. Dooley, 1974; Turrell, 1992; Turrell et al., 1992; Hill et al., 2008), but where previous studies have identified fairly broad thermohaline jets of some 50 to 70 km across (Chapter 2), our results reveal the presence of clusters of jets which are, individually, very narrow (around 10 km). Previous studies have lacked sufficient spatial

resolution to separate individual thermohaline jets.

Volume transport in the FIC and ESAI is found to be dominated by the non-thermohaline component, which likely comprises wind- and ocean-driven flow. It is a clear advantage of gliders over traditional ship surveys that gliders allow us to reference high-resolution geostrophic shear to an independent observation of flow, although the limited width of the glider-occupied section means that glider observations of transport do not capture the entire flow of the FIC and ESAI. The maximum velocities of thermohaline and non-thermohaline flow are comparable: the dominance of the latter comes instead from the broad spatial scales of non-thermohaline flow relative to the narrow thermohaline jets. The influence of wind on the FIC an ESAI has been found to be perhaps more limited than by other studies: wind variability explains no more than 35% of DAC velocity variability. The presence of southward thermohaline jets, dense layers of AW and CAW, and a steady, southward ocean-driven flow as reported by Holt and Proctor (2008) are hypothesised to limit the influence of the wind on the FIC and ESAI, accounting for the persistence of generally southward flow in diverse wind conditions.

Chapter 5

Conclusion

The forcing and variability of the Fair Isle Current (FIC) and the East Shetland Atlantic Inflow (ESAI), the northwestern inflows to the northern North Sea, has been investigated on timescales ranging from the day-to-day to the year-to-year. Scientifically, three conclusions are prominent. Firstly, the influence of the wind on short timescales is found to be limited; however, we report a possible influence of wind forcing on hydrography on interdecadal time scales through the influence of the North Atlantic Oscillation (NAO). We find that wind variability explains less than a majority ($>$ 30%; Figure 4.10) of glider dive-average current (DAC) variability. This is in contrast to previous studies that have found wind forcing to be highly significant on daily, weekly and seasonal time scales (Turrell et al., 1990; Winther and Johannessen, 2006; Mathis et al., 2015, respectively). However, the wind could be the mechanism behind the negative relationship between the strength of the NAO and mean temperatures in the northwestern inflows (Section 2.6): a positive NAO tends to increase the strength of westerly winds over the North Sea, particularly in winter (Mathis et al., 2015), so it would be expected that a tendency towards stronger wind mixing would suppress temperatures. In addition, or else alternatively, the strength of westerly winds could alter circulation in the Atlantic in such a way that anomalously cold water is advected into the North Sea.

Secondly, salinity has been shown to be an important component of the dynamics of the northwestern inflows. The annual cycle of temperature dominates the annual cycle of thermohaline transport (Section 2.5) and, along with tidal mixing, surface heating is the dominant control on frontal location in summer (Section 3.3). But in winter, when the horizontal temperature gradient is at a minimum, the horizontal salinity gradient drives appreciable thermohaline transport and maintains distinctions between key water masses that sustain frontal boundaries that do not exist in the temperature distribution (Section 3.3). The response of North Sea temperatures to climate change is known with greater certainty than the response of North Sea salinities to climate change (Holt et al., 2010). The regional importance of salinity demonstrated by these results indicates that an accurate prediction of future North Sea salinities is an important aspect of an accurate prediction of the North Sea under climate change. The range

and drivers of the interannual variability of salinity deserve further investigation, particularly as the correlations between salinity and the NAO and the Atlantic Meridional Oscillation (AMO, Figure 2.10) are not significant at the 5% level. Globally, salinity is likely to be similarly important in other shelf sea regions with significant oceanic inflow: for instance, the South China Sea (Shaw, 1991; Su, 2004), along the eastern coast of the United States (Blanton et al., 1981) and around Antarctica (Moffat et al., 2009).

Thirdly, elements of this work are relevant to the study of the North Sea under climate change. An understanding of the range of natural variability on climate-relevant time scales (i.e. decades) is a prerequisite for identifying unnatural change. The identification of the NAO and AMO as drivers of hydrographic variability on interdecadal time scales helps us to better understand this natural variability. (Of course, we overlook feedbacks between climate change, and the NAO and AMO.) Furthermore, the enhanced understanding of thermohaline flow in the FIC and ESAI provided by Chapter 2, coupled with the description of the processes controlling frontal location presented in Chapter 3, increase our knowledge of how processes attendant on the development and decay of seasonal stratification affect the hydrography and circulation in the region. Observations of the same frontal system at the summer peak of stratification would be an interesting further study of the h/u^3 criterion in general, and would provide an instructive test of the conclusions of Chapter 3 in particular. The projected increase in the duration of stratification under climate change increases the influence that such processes will have on the system over an annual cycle, and motivates further work in this area.

In addition to the scientific conclusions, the three studies presented in this thesis prompt a consideration of the value of gliders to a shelf sea observing system. The spatial resolution of the glider observations presented in Chapters 3 and 4 is much higher than the spatial resolution of the CTD observations presented in Chapter 2. The ship and glider observations presented in Figure 5.1 are separated by a few days – the glider was slower than the ship and so took longer to complete even a partial occupation of the JONSIS section – which likely explains some differences between the two sets of observations, as does the southward advection of the glider away from the JONSIS section; but these differences notwithstanding, it is clear that the glider (dives 300 m apart) is observing fine-scale structure in the temperature and salinity, and therefore density, distributions that cannot be observed by the ship (casts average 11 km apart). The benefits of this high resolution to the research presented in this thesis have principally been two-fold. Firstly, this high horizontal resolution allows the glider to more accurately capture narrow features such as the depression of isohalines between 1 and 1.5°W (Figure 5.1). The ship observations do not resolve this feature, which appears instead as a horizontal perturbation in otherwise largely straight-line isohalines. The same feature is observed in the isopycnals. Secondly, the thermohaline velocity derived from the glider observations reveal the existence of very narrow thermohaline jets which commonly appear in clusters (Figure 4.8). In the lower-resolution ship observations, the individual jets do not appear as separate features: for instance, what the glider observes as two southward-flowing

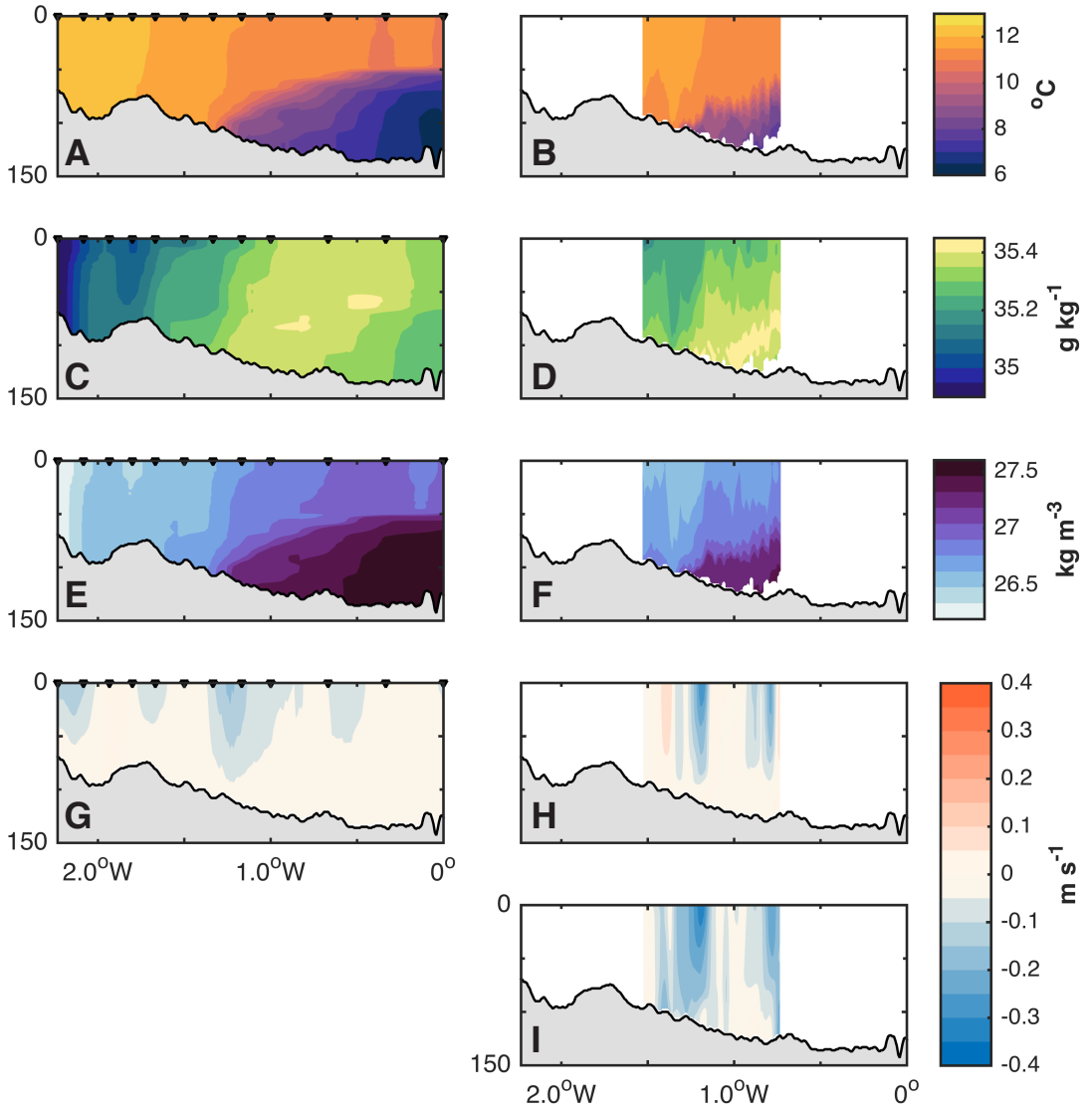

Figure 5.1 From the Scotia cruise that deployed the glider (left-hand panels), and from the glider itself (occupation one; right-hand panels): **A** and **B** conservative temperature (°C); **C** and **D** absolute salinity (g kg^{-1}); **E** and **F** density (kg m^{-3}); **G** and **H** thermohaline geostrophic velocity (m s^{-1}); and **I** absolute geostrophic velocity (m s^{-1}). Triangles on the left-hand panels indicate the location of casts.

jets and one, weaker northward-flowing jet, the ship observes as a single, broader southward flow (Figure 5.1). Ship observations lack an independent observation of current to which geostrophic shear may be referenced, so the same comparison cannot be made for absolute velocity. In general, the ability to observe the narrow nature of thermohaline jets in the region has the potential to improve our knowledge of transport pathways, especially if the influence of these narrow jets may be realistically represented in models.

The glider allows us to observe the northwestern inflows at higher temporal resolution than is possible from ships: we present ten glider occupations from a two-month period, whereas the number of ship occupations in a given year has not exceeded eight since the late 1980s

(Figure 2.1), and likely has not ever. In the two-month period of the glider deployment, observations from two ship occupations are available. The greater temporal resolution of the glider observations allows the evolution of the hydrography, velocity and transport of the northwestern inflows to be tracked on time scales of around three days to one week. Examining the data instead in longitude-time space allowed us to identify the location of the front and to quantify its offshore movement ten times over the deployment (Figure 3.4A). The ship observations provide us with just two frontal crossings.

The use of glider observations in this thesis has highlighted some of the disadvantages of gliders as an observational platform. The southward advection of the glider by the residual flow and the difficulty of keeping the glider flying straight along the transect have added a degree of positional uncertainty to the glider observations. This uncertainty does not affect ship observations. The occupation of only part of the JONSIS section by the glider (e.g. Figures 4.4 and 4.9) makes interpretation of the transport observations difficult: distinguishing with certainty a genuine temporal change in transport from a apparent temporal change arising from incomplete spatial observation of the flow is not possible. Both of these limitations may be avoided by glider pilots in a future deployment. An understanding of how sampling limitations have affected analysis of the present glider observations will be of use to future mission design. Deploying two or more gliders, each occupying a portion of the section, in any such future mission would enable the separate influence of spatial and temporal changes to be better understood.

Appendix A

Heating-stirring model

A.1 Model modifications

This section describes modifications to the heating-stirring model of Simpson and Bowers (1984) made by Hughes (2014), who evaluated the model in its original form and made the modifications used in Chapter 3. The material presented here is not included for examination but is intended to augment the description of the model presented in Section 3.3.

The original version of the heating-stirring model used in Section 3.3 was described by Simpson and Bowers (1984). In the original formulation of the model, the heat flux through the surface of the ocean, Q is given by:

$$Q = Q_s + \lambda(T_d - T_s) \tag{A.1}$$

where Q_s is incoming solar radiation (W m^{-2}), λ is a thermal exchange coefficient, and T_d and T_s are the atmospheric dew-point and sea-surface temperature respectively (°C; Edinger et al., 1968). The second term on the right-hand side of Equation A.1 represents heat loss to the atmosphere. A positive flux is one from the atmosphere to the ocean; a negative flux is one from the ocean to the atmosphere. The model uses this surface heat flux to calculate the daily change in sea-surface temperature according to:

$$\frac{dT_s}{dt} = \frac{Q}{c_w \rho} \tag{A.2}$$

where c_w is the specific heat capacity of water (J kg^{-1} K-1) and ρ is density (kg m^{-3}). The model assumes a two-layer structure: 55% of any heat gain is absorbed by the top layer; the remaining 45% is distributed exponentially with depth in the bottom layer. The model also uses the surface heat flux to calculate the change in potential energy, V (J m^{-3}):

$$\frac{dV}{dt} = \frac{g\alpha Qh}{2c} \tag{A.3}$$

where g is gravitational acceleration (m s^{-2}), α is the thermal expansion coefficient of seawater ($^{\circ}C^{-1}$) and h is depth (m).

When using Equation A.1 to calculate Q, the heating-stirring model underestimates surface temperatures in winter (Bowers and Simpson, 1990; Elliott and Clarke, 1991; Hughes, 2014) because it overestimates heat loss in that season. To improve the model's representation of surface temperatures, Hughes (2014) replaced Equation A.1 with:

$$Q = Q_s + Q_r + Q_c + Q_e \tag{A.4}$$

where Q_r is the radiative heat flux, Q_c is the conductive heat flux and Q_e is the evaporative heat flux (all in W m^{-2}). The heat loss term in Equation A.1 is equivalent to the sum of Q_r, Q_c and Q_e in Equation A.4. Because heat fluxes are rarely directly observed, they are instead calculated from meteorological observations using the formulas of Gill (1982) as implemented by Hughes (2014):

$$Q_r = E_m S_b (T_s + 274)^4 (0.39 - 0.05\sqrt{e_a})(1 - kC_c^2) \tag{A.5}$$

$$Q_c = S\rho_a c_a W(T_s - T_a) \tag{A.6}$$

$$Q_e = (l\rho_a DW)(q_w - q_a) \tag{A.7}$$

where:

- E_m = 0.985 is the emissivity of the sea surface
- S_b = 5.67 $\times$ 10^{-8} is the Stephan-Boltzmann constant (W m^{-2} K^{-4})
- e_a is the vapour pressure of water (Pa)
- k is a latitudinal adjustment for cloud cover
- C_c is cloud cover (tenths)
- S = 1.45 $\times$ 10^{-3} is the Stanton number
- ρ_a is the density of air (kg m^{-3})
- c_a = 1004 is the specific heat capacity of air (J kg^{-1} K^{-1})
- W is wind speed (m s^{-1})
- T_a is air temperature ($^{\circ}$C)
- l is the latent heat of evaporation (J kg^{-1})
- D = 1.5 $\times$ 10^{-3} is the Dalton number
- q_w and q_a are the specific humidity of air at water and air temperature respectively (g kg^{-1})

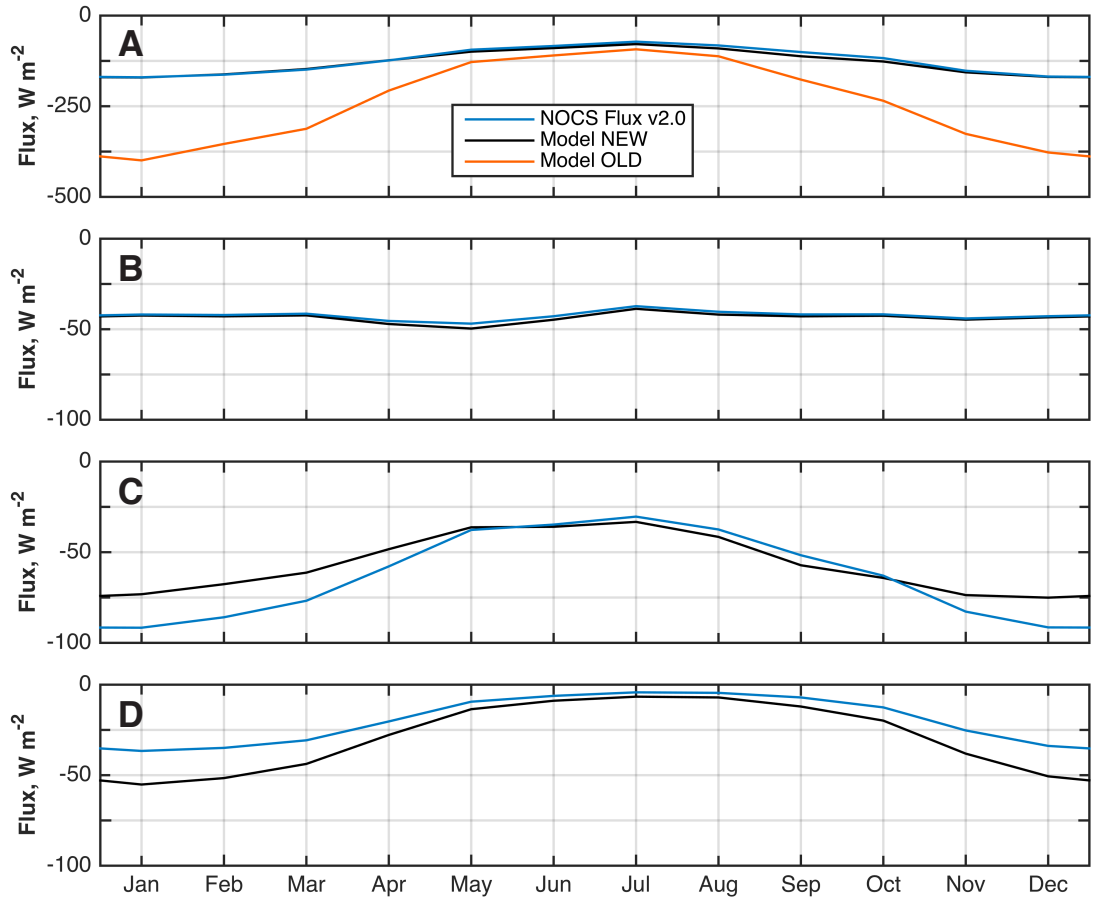

Figure A.1 **A** Heat loss over an annual cycle, which is the sum of the: **B** radiative heat flux, **C** latent heat flux and **D** sensible heat flux. Fluxes are in W m^{-2}. Blue lines represent flux estimates extracted from the NOCS Flux v2.0 data set, black lines lines represent flux estimates calculated by the modified heating-stirring model, and the orange line (panel A only) represents the heat loss calculated by the original formulation of the model. Data are from east of Shetland and are monthly means calculated for the period 1973 – 2003. Tick marks are at the middle of each month. Figure modified from Hughes (2014, figure 3.2) and reproduced by kind permission.

Q_s, the meteorological observations used to force the model, and the flux estimates used for validation of the new method are taken from the NOCS Flux v2.0 data set (National Oceanography Centre, 2008; Berry and Kent, 2009, 2011). With the exception of Q_s, flux estimates from NOCS Flux v2.0 cannot be input directly because the model calculates heat loss from modelled sea-surface temperature and so must be allowed to evolve within the model.

The new method simulates surface heat fluxes over an annual cycle that are in reasonable agreement with fluxes extracted directly from the NOCS Flux v2.0 data set (Figure A.1). Importantly, the overall heat loss term matches the NOCS Flux v2.0 values closely and is a considerable improvement on the heat loss term calculated using Equation A.1 (Figure A.1A). Consequently, the modified heating-stirring model produces more accurate surface temperatures (Hughes, 2014).

The second modification made by Hughes (2014) is to include the effects of additional

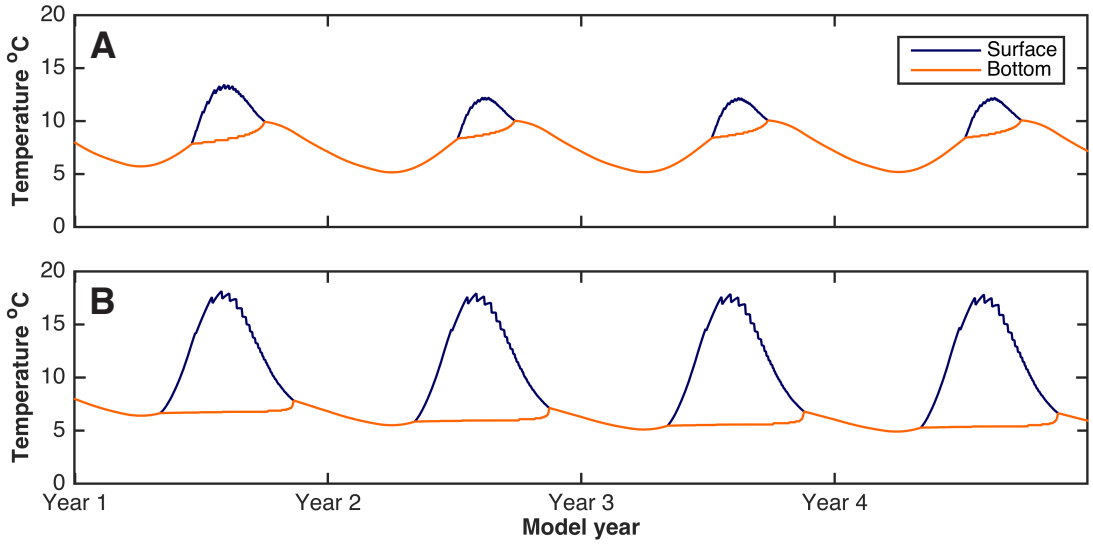

Figure A.2 Time series of temperature (°C) from all four years of the model run for **A** the westernmost longitude (2.2°W) and **B** the easternmost longitude (0°). In both panels, the blue line indicates surface temperature, and the orange line indicates bottom temperature. Note that the depth of the bottom is 73 m for panel A and 126 m for panel B.

mixing brought about by a constant residual current: originally, the model included only the effects of tidal mixing. The original model calculates the average depth-mean flow speed, $\widehat{u}^3$ (m s^{-1}), over an M_2 tidal cycle according to:

$$\widehat{u}^3 = \frac{4}{3\pi} u_t^3 \tag{A.8}$$

where u_t^3 is the depth-mean amplitude of the tidal speed (m s^{-1}). This is commonly taken to be the velocity amplitude of the M_2 tide. The tide is assumed to be rectilinear. To add the effects of a constant residual current, Hughes (2014) assumes a constant flow aligned with the axis of the rectilinear tide. Because mixing is related to the cube of u, and because the tidal current will alternately flow with and against the residual current, the combined effect of the two currents cannot be calculated by adding their average values together. Instead, in cases when the speed of the residual current is greater than the amplitude of the tidal speed, the average depth-mean flow over a tidal cycle is:

$$\widehat{u}^3 = u_r^3 + \frac{3u_r u_t^2}{2} \tag{A.9}$$

Alternatively, when the speed of the residual current is less than the amplitude of the tidal speed, the average depth-mean flow over a tidal cycle is:

$$\widehat{u}^3 = \frac{4u_t^3}{3\pi} + \frac{6u_t u_r^2}{\pi} \tag{A.10}$$

Hughes (2014) concluded that the above modifications improved the accuracy of the heating-stirring model, and enhanced its ability to model temperatures in the northern North Sea.

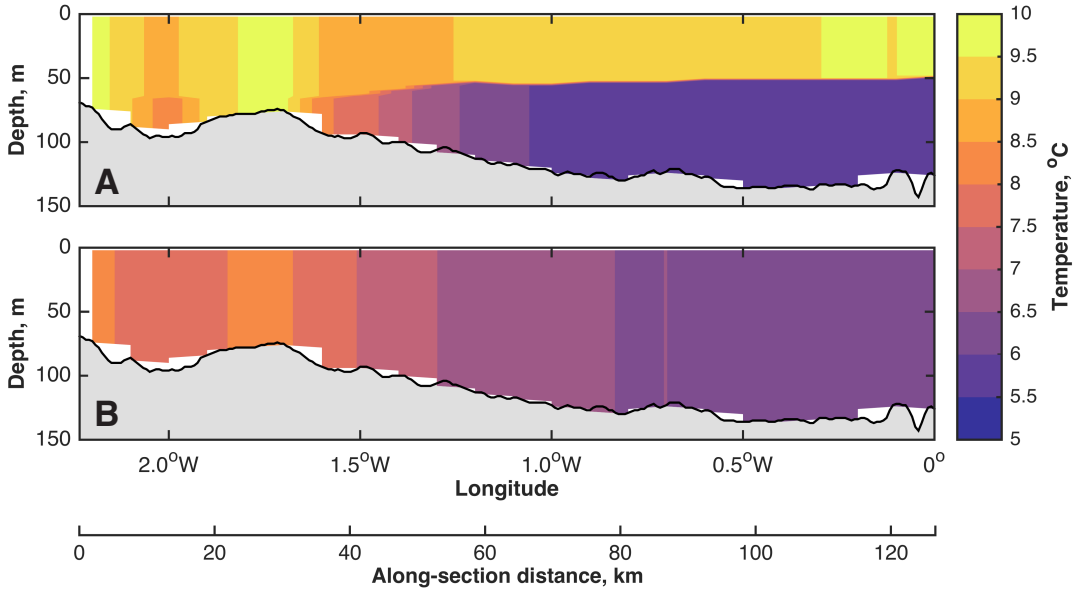

Figure A.3 Sample output (temperature, °C) from the heating-stirring model **A** from 12th October 2013, the first day of the glider deployment and **B** from 1st December 2013, the last day of the glider deployment.

A.2 Model set-up

To run the model experiments in Section 3.3, temperature at the JONSIS section was simulated for 2013 at daily resolution and at a horizontal spacing of 0.1° longitude. Meteorological data for 2013 were extracted from NOCS Flux v2.0 and were interpolated from monthly to daily resolution; at each day, values were interpolated along the section to 0.1° resolution. Tidal speed amplitude for an intermediate tide (i.e. mid-way between a spring and a neap tide) was calculated as described in Section 3.3 and was similarly interpolated along the section to 0.1° resolution.

From an arbitrary depth-uniform starting temperature of 8°C, the model reached a stable annual cycle after three simulated years (Figure A.2; Elliott and Clarke, 1991; Hughes, 2014). Additionally, the starting temperature had no effect on the modelled temperatures after this time (see also Elliott and Clarke, 1991). Note that each year received the same meteorological forcing. Results covering the period of the glider deployment (12th October – 1st December; Figure 3.4) were extracted from the fourth simulated year. Example sections from this final simulated year of the model run are shown in Figure A.3. Note that the model reproduces key features such as the separation of the JONSIS section into a western, fully mixed region and an eastern, stratified region, as well as the strengthening of the thermocline to the east. Furthermore, the amplitude of the annual cycle of temperature in the east is greater than in the east (Figure A.2). The increase in bottom temperature with the onset of full-depth mixing in the autumn is also correctly reproduced (Figures A.2 and A.3; Simpson and Bowers, 1984). Note that a fully mixed profile in the west is produced at spring tide velocities (cf. Figure A.2).

References

Ådlandsvik, B. (2008). Marine downscaling of a future climate scenario for the North Sea, *Dynamic Meteorology and Oceanography* **60**: 451 – 458.

Alheit, J., Pohlmann, T., Casini, M., Greve, W., Hinrichs, R., Mathis, M., O'Driscoll, K., Vorberg, R. and Wager, C. (2012). Climate variability drives anchovies and sardines into the North and Baltic Seas, *Progress in Oceanography* **96**: 128 – 139.

Backhaus, J. O. and Maier-Reimer, E. (1983). On seasonal circulation patterns in the North Sea, *in* J. Sündermann and W. Lenz (eds), *North Sea Dynamics*, Springer-Verlag, Berlin, Germany.

Barrett, J. H., Locker, A. M. and Roberts, C. M. (2004). The origins of intensive marine fishing in medieval Europe: the English evidence, *Proceedings of the Royal Society of London B* **271**: 2417 – 2421.

Beaird, N., Fer, I., Rhines, P. and Eriksen, C. C. (2012). Dissipation of turbulent kinetic energy inferred from Seagliders: an application to the Eastern Nordic Seas overflows, *Journal of Physical Oceanography* **42**: 2268 – 2282.

Beaugrand, G. (2004). The North Sea regime shift: evidence, causes, mechanisms and consequences, *Progress in Oceanography* **60**: 245 – 262.

Berry, D. I. and Kent, E. C. (2009). A new air-sea interaction gridded dataset from ICOADS with uncertainty estimates, *Bulletin of the American Meteorological Society* **90**: 645 – 656.

Berry, D. I. and Kent, E. C. (2011). Air-sea fluxes from ICOADS: the construction of a new gridded dataset with uncertainty estimates, *International Journal of Climatology* **31**: 987 – 1001.

Berx, B., Damerell, G. M., Gallego, A., Hall, R. A., Heywood, K. J., Lee, G. A. and Queste, B. Y. (2018). Glider observations of northwestern inflows of Atlantic water to the North Sea, DOI: 10/ck8r.

Berx, B., Gallego, A., Hughes, S. L., Slesser, G., Dunn, J., Lee, D., Geldart, M., O'Hara-Murray, R., Hindson, J., Turrell, W. R. and Sanchez, J. (2014). Brahan Project in situ data, www.thebrahanproject.com, DOI: 10.7489/1597-1.

Berx, B. and Hughes, S. L. (2009). Climatology of surface and near-bed temperature and salinity on the north-west European continental shelf for 1971 – 2000, *Continental Shelf Research* **29**: 2286 – 2292.

Blanton, J. O., Atkinson, L. P., Pietrafesa, L. J. and Lee, T. N. (1981). The intrusion of Gulf Stream water across the continental shelf due to topographically-induced upwelling, *Deep-Sea Research* **28**: 393 – 405.

Bowers, D. G. and Simpson, J. H. (1987). Mean position of tidal fronts in European shelf seas, *Continental Shelf Research* **1**: 35 – 44.

Bowers, D. G. and Simpson, J. H. (1990). Geographical variations in the seasonal heating cycle in northwest European shelf seas, *Continental Shelf Research* **10**: 185 – 199.

Bretherton, F. P., Davis, R. E. and Fandry, C. B. (1976). A technique for objective analysis and design of oceanographic experiments applied to Mode-73, *Deep-Sea Research* **23**: 559 – 582.

Brown, J., Hill, A. E., Fernand, L. and Horsburgh, K. J. (1999). Observations of a seasonal jet-like circulation at the central North Sea cold pool margin, *Estuarine, Coastal and Shelf Science* **48**: 343 – 355.

Chami, M., Marken, E., Stamnes, J. J., Khomenko, G. and Korotaev, G. (2006). Variability of the relationship between the particulate backscattering coefficient and the volume scattering function measured at fixed angles, *Journal of Geophysical Research* **111**: C05013.

Chereskin, T. K. and Trunnell, M. (1996). Correlation scales, objective mapping, and absolute geostrophic flow in the California Current, *Journal of Geophysical Research* **101**: 22619 – 22629.

Claussen, U., Zevenboom, W., Brockmann, W., Topuc, D. and Bot, P. (2009). Assessment of the eutrophication status of transitional, coastal and marine waters within OSPAR, *Hydrobiologia* **629**: 49 – 58.

Coelingh, J. P., van Wijk, A. J. M. and Holtslag, A. A. M. (1996). Analysis of wind speed observations over the North Sea, *Journal of Wind Engineering* **61**: 51 – 69.

Damm, P., Hinzpeter, H., Luthardt, H. and Terzenbach, U. (1994). Seasonal and interannual variability in the atmosphere and the sea, *in* J. Sündermann (ed.), *Circulation and comtaminant fluxes in the North Sea*, Springer-Verlag, Berlin, Germany.

Dee, D. P., Uppala, S. M., Simmons, A. J., Berrisford, P., Poli, P., Kobayashi, S., Andrae, U., Balmaseda, M. A., Balsamo, G., Bauer, P., Bechtold, P., Beljaars, A. C. M., van de Berg, L., Bidlot, J., Bormann, N., Delsol, C., Dragani, R., Fuentes, M., Geer, A. J., Haimberger, L., Healy, S. B., Hersbach, H., Hólm, E. V., Isaksen, L., Kållberg, P., Köhler, M., Matricardi, M., McNally, A. P., Monge-Sanz, B. M., Morcrette, J.-J., Park, B.-K., Peubey, C., de Rosnay, P., Tavolato, C., Thépaut, J.-N. and Vitart, F. (2011). The ERA-Interim reanalysis: configuration and performance of the data assimilation system, *Quarterly Journal of the Royal Meteorological Society* **137**: 553 – 597.

Denman, K. L. and Freeland, H. J. (1985). Correlation scales, objective mapping and a statistical test of geostrophy over the continental shelf, *Journal of Marine Research* **43**: 517 – 539.

Dickson, R. R., Meincke, J., Malmberg, S. A. and Lee, A. J. (1988). The great salinity anomaly in the northern North Atlantic 1968 – 1982, *Progress in Oceanography* **20**: 103 – 151.

Dooley, H. D. (1974). Hypotheses concerning the circulation of the northern North Sea, *Journal du Conseil International pour l'Exploration de la Mer* **36**: 54 – 61.

Dooley, H. D. (1983). Seasonal variability in the position and strength of the Fair Isle Current, *in* J. Sündermann and W. Lenz (eds), *North Sea Dynamics*, Springer-Verlag, Berlin, Germany.

du Bois, P. B. (1996). Mapping of water masses in the North Sea using radioactive tracers, *Endeavour* **20**: 2 – 7.

Edinger, J. E., Duttweiler, D. W. and Geyer, J. C. (1968). The response of water tempearture to meteorological conditions, *Water Resources Research* **4**: 1137 – 1143.

Edwards, M., Beaugrand, G., Reid, P. C., Rowden, A. A. and Jones, M. B. (2002). Ocean climate anomalies and the ecology of the North Sea, *Marine Ecology Progress Series* **239**: 1 – 10.

Edwards, M., Johns, D. G., Leterme, S. C., Svendsen, E. and Richardson, A. J. (2006). Regional climate change and harmful algal blooms in the northeast Atlantic, *Limnology and Oceanography* **51**: 820 – 829.

Egbert, G. D., Bennett, A. F. and Foreman, M. G. G. (1994). TOPEX/POSEIDON tides estimated using a global inverse model, *Journal of Geophysical Research* **99**: 24821 – 24852.

Egbert, G. D. and Erofeeva, S. Y. (2002). Efficient inverse modelling of barotropic ocean tides, *Journal of Atmospheric and Oceanic Technology* **19**: 183 – 204.

Egbert, G. D., Erofeeva, S. Y. and Ray, R. D. (2010). Assimilation of altimetry data for nonlinear shallow-water tides: quarter-diurnal tides of the northwest European shelf, *Continental Shelf Research* **30**: 668 – 679.

Elliott, A. and Clarke, T. (1991). Seasonal stratification in the northwest European shelf seas, *Continental Shelf Research* **11**: 467 – 492.

Emeis, K.-C., van Beusekom, J., Callies, U., Ebinghaus, R., Kannen, A., Kraus, G., Kröncke, I., Lenhart, H. J., Lorkowski, I., Matthias, V., Möllmann, C., Pätsch, J., Scharfe, M., Thomas, H., Weisse, R. and Zorita, E. (2015). The North Sea: a shelf sea in the anthropocene, *Journal of Marine Systems* **141**: 18 – 33.

Eriksen, C. C., James Osse, T., Light, R. D., Wen, T., Lehman, T., Sabin, P. L., Ballard, J. W. and Chiodi, A. M. (2001). Seaglider: a long-range autonomous underwater vehicle for oceanographic research, *IEEE Journal of Oceanic Engineering* **26**: 424 – 436.

EU (2000). Directive 2000/60/EC of the European Parliament and of the Council, 23rd October 2000 (Water Framework Directive), *Official Journal of the European Union* (L327): 1 – 72.

EU (2008). Directive 2008/56/EC of the European Parliament and of the Council, 17th June 2008 (Marine Strategy Framework Directive), *Official Journal of the European Union* (L164): 19 – 40.

Fer, I., Peterson, A. K. and Ullgren, J. E. (2014). Microstructure measurements from an underwater glider in the turbulent Fareo Bank Channel overflow, *Journal of Atmospheric and Oceanic Technology* **31**: 1128 – 1150.

Frajka-Williams, E., Eriksen, C. C., Rhines, P. B. and Harcourt, R. R. (2011). Determining vertical water velocities from Seaglider, *Journal of Atmospheric and Oceanic Technology* **28**: 1641 – 1656.

Fulton, T. W. (1897). The currents of the North Sea and their relation to fisheries, *Report of the Fishery Board for Scotland, 15th year (1896), part 3* **15**: 334 – 395.

Furnes, G. K. (1980). Wind effects in the North Sea, *Journal of Physical Oceanography* **10**: 978 – 984.

Furnes, G. K., Hackett, B. and Sætre, R. (1986). Retroflection of Atlantic water in the Norwegian Trench, *Deep-Sea Research* **33**: 247 – 265.

Garau, B., Ruiz, S., Zhang, W. G., Pascual, A., Heslop, E., Kerfoot, J. and Tintoré, J. (2011). Thermal lag correction on Slocum CTD glider data, *Journal of Atmospheric and Oceanic Technology* **28**: 1065 – 1071.

Garrett, C. J., Keeley, J. R. and Greenberg, D. A. (1978). Tidal mixing versus thermal stratification in the Bay of Fundy and Gulf of Maine, *Atmosphere-Ocean* **16**: 403 – 423.

Gill, A. E. (1982). *Atmosphere-Ocean Dynamics*, Vol. 30 of International Geophysics series, Academic Press, London, United Kingdom.

Green, R. E., Bower, A. S. and Lugo-Fernández (2014). First autonomous bio-optical profiling float in the Gulf of Mexico reveals dynamic biogeochemsitry in deep waters, *PLOS One* **9**: e101658.

Gröger, M., Maier-Reimer, E., Mikolajewicz, U., Moll, A. and Sein, D. (2013). NW European shelf under climate warming: implications for open ocean-shelf exchange, primary production and carbon absorption, *Biogeosciences* **10**: 3767 – 3792.

Hall, R. A., Aslam, T. and Huvenne, V. A. I. (2017). Partly standing internal tides in a dendritic submarine canyon observed by an ocean glider, *Deep-Sea Research I* **126**: 73 – 84.

Harwood, A. J. P., Dennis, P. F. Marca, A. D., Pilling, G. M. and Millner, R. S. (2008). The oxygen isotope composition of water masses within the North Sea, *Estuarine, Coastal and Shelf Science* **78**: 353 – 359.

Hill, A. E., Brown, J., Fernand, L., Holt, J. T., Horsburgh, K. J., Proctor, R., Raine, R. and Turrell, W. R. (2008). Thermohaline circulation of shallow tidal seas, *Geophysical Research Letters* **35**: L11605.

Hill, A. E., Horsburgh, K. J., Garvine, R. W., Gillibrand, P. A., Slesser, G., Turrell, W. R. and Adams, R. D. (1997). Observations of a density-driven recirculation of the Scottish Coastal Current in the Minch, *Estuarine, Coastal and Shelf Science* **45**: 473 – 484.

Hill, A. E., James, I. D., Linden, P. F., Matthews, J. P., Prandle, D., Simpson, J. H., Gmitrowicz, E. M., Smeed, D. A., Lwiza, K. M. M., Durazo, R., Fox, A. D. and Bowers, D. G. (1993). Dynamics of tidal mixing fronts in the North Sea, *Philosophical Transactions of the Royal Society of London, Series A* **343**: 431 – 446.

Hjøllo, S. S., Skogen, M. D. and Svendsen, E. (2009). Exploring the currents and heat within the North Sea using a numerical model, *Journal of Marine Systems* **78**: 180 – 192.

Holliday, N. P. and Reid, P. C. (2001). Is there a connection between high transport of water through the Rockall Trough and ecological changes in the North Sea?, *ICES Journal of Marine Science* **58**: 270 – 274.

Holt, J., Hughes, S. L., Hopkins, J., Wakelin, S. L., Holliday, N. P., Dye, S., Gónzalez-Pola, C., Hjøllo, S. S., Mork, K. A., Nolan, G., Proctor, R., Read, J., Shammon, T., Sherwin, T., Smyth, T., Tattersall, G., Ward, B. and Wiltshire, K. H. (2012). Multi-decadal variability and trends in the temperature of the northwest European continental shelf: a model-data synthesis, *Progress in Oceanography* **106**: 96 – 117.

Holt, J. T. and James, I. D. (1999). A simulation of the southern North Sea in comparison with measurements from the North Sea Project, *Continental Shelf Research* **19**: 1087 – 1112.

Holt, J. T. and Proctor, R. (2008). The seasonal circulation and volume transport on the northwest Eurpoean continental shelf: a fine-resolution model study, *Journal of Geophysical Research* **113**: C06021.

Holt, J. T. and Umlauf, L. (2008). Modelling the tidal mixing fronts and seasonal stratification of the northwest European continental shelf, *Continental Shelf Research* **28**: 887 – 903.

Holt, J., Wakelin, S. L., Lowe, J. and Tinker, J. (2010). The potential impacts of climate change on the hydrography of the northwest European contintenal shelf, *Progress in Oceanography* **86**: 361 – 379.

Hopkins, J. and Polton, J. A. (2012). Scales and structure of frontal adjustment and freshwater export in a region of freshwater influence, *Ocean Dynamics* **62**: 45 – 62.

Hughes, S. L. (2014). *Inflow of Atlantic water to the North Sea: seasonal variability on the East Setland Shelf*, PhD thesis, University of Aberdeen, Aberdeen, United Kingdom. See: ethos.bl.uk/OrderDetails.do?uin=uk.bl.ethos.629386.

Hurrell, J. W. (2009). North Atlantic Oscillation, *in* J. Steele, K. Turekian and S. Thorpe (eds), *Encyclopedia of Ocean Sciences*, Academic Press, San Diego, United States of America.

Hurrell, J. W., Kushnir, Y., Ottersen, G. and Visbeck, M. (2003). An overview of the North Atlantic Oscillation, *in* J. Hurrell, Y. Kushnir, G. Ottersen and M. Visbeck (eds), *The North Atlantic Oscillation: climatic significance and environmental impact*, American Geophysical Union, Washington D.C., United States of America.

Huthnance, J. M. (1997). North Sea interaction with the North Atlantic ocean, *Deutsche Hydrografische Zeitschrift* **49**: 153 – 162.

Huthnance, J. M., Holt, J. T. and Wakelin, S. L. (2009). Deep-ocean exchange with the west-European shelf seas, *Ocean Science* **5**: 621 – 634.

Inall, M. E., Gillibrand, P. A., Griffiths, C., MacDougal, N. and Blackwell, K. (2009). On the oceanographic variaiblity of the Northwest European shelf to the west of Scotland, *Journal of Marine Systems* **77**: 210 – 226.

IOC, SCOR and IAPSO (2010). *The international thermodynamic equation of seawater, 2010: calculation and use of thermodynamic properties (English)*, Intergovernmental Oceanographic Commission, manuals and guides number 56, UNESCO.

Ivanoff, A. (1977). Oceanic absorption of solar energy, *in* E. B. Kraus (ed.), *Modelling and prediction of the upper layers of the ocean*, Pergamon Press, Oxford, United Kingdom.

Janssen, F., Schrum, C. and Backhaus, J. O. (1999). A climatological data set of temperature and salinity for the Baltic Sea and the North Sea, *German Journal of Hydrography* (Supplement 9): 1 – 245.

Kannen, A. (2014). Challenges for marine spatial planning in the context of multiple sea uses, policy arenas and actors based on experiences from the German North Sea, *Regional Environmental Change* **14**: 2139 – 2150.

Kröncke, I. (2011). Changes in Dogger Bank macrofauna communities in the late 20th century caused by fishing and climate, *Estuarine, Coastal and Shelf Science* **94**: 234 – 245.

Kröncke, I., Dippner, J., Heyen, H. and B., Z. (1998). Long-term changes in macrofaunal communities off Norderney (East Frisia, Germany) in relation to climate variability, *Marine Ecology Progress Series* **167**: 25 – 36.

Kröncke, I., Reiss, H. and Dippner, J. (2013). Effects of cold winters and regime shifts on macrofauna communities in shallow coastal regions, *Estuarine, Coastal and Shelf Science* **119**: 79 – 90.

Kundu, P. K. (1976). Ekman veering observed near the ocean bottom, *Journal of Physical Oceanography* **6**: 238 – 242.

Larsen, K. M. H., Gónzalez-Pola, C., Fratantoni, P., Beszczynska-Möller, A. and Hughes, S. L. (eds) (2014). *ICES Report on Ocean Climate 2014, ICES co-operative reseach report no. 329*, International Council for the Exploration of the Sea, Copenhagen, Denmark.

Larsen, K. M. H., Gónzalez-Pola, C., Fratantoni, P., Beszczynska-Möller, A. and Hughes, S. L. (eds) (2016). *ICES Report on Ocean Climate 2015, ICES co-operative reseach report no. 331*, International Council for the Exploration of the Sea, Copenhagen, Denmark.

Lenhart, H. J., Mills, D. K., Baretta-Bekker, H., van Leeuwen, S. M., van der Molen, J., Baretta, J. W., M., B., Desmit, X., Kühn, W., Lacriox, G., Los, J. H., Ménesguen, A., Neves, R., Proctor, R., Ruardij, P., Skogen, M. D., Vanhoutte-Brunier, A., Villars, M. T. and Wakelin, S. L. (2010). Predicting the consequences of nutrient reduction on the eutrophication status of the North Sea, *Journal of Marine Systems* **81**: 148 – 170.

Lenhart, H. J., Radach, G., Backhaus, J. O. and Pohlmann, T. (1995). Simulations of the North Sea circulation, its variability and its implemetation as hydrodynamical forcing in ERSEM, *Netherlands Journal of Sea Research* **33**: 271 – 299.

Leterme, S. C., Pingree, R. D., Skogen, M. D., Seuront, L., Reid, P. C. and Attrill, M. J. (2008). Decadal fluctuations in North Atlantic water inflow in the North Sea between 1958 – 2003: impacts on temperature and phytoplankton populations, *Oceanologia* **50**: 59 – 72.

Lindley, J. A., Roskell, J., Warner, A. J., Halliday, N. C., Hunt, H. G., John, A. W. G. and Jonas, T. D. (1990). Doliolids in the German Bight in 1989: evidence for exceptional inflow into the North Sea, *Journal of the Marine Biological Association of the United Kingdom* **70**: 679 – 682.

Loder, J. W. and Greenberg, D. A. (1986). Predicted positions of tidal fronts in the Gulf of Maine region, *Continental Shelf Research* **6**: 397 – 414.

Lorkowski, I., Pätsch, J., Moll, A. and Kühn, W. (2012). Interannual variability of carbon fluxes in the North Sea from 1970 to 2006: competing effects of abiotic and biotic drivers on the gas exchange of CO_2, *Estuarine, Coastal and Shelf Science* **100**: 38 – 57.

Marsh, R., Haigh, I. D., Cunningham, S. A., Inall, M. E., Porter, M. and Moat, B. I. (2017). Large-scale forcing of the European Slope Current and associated inflows to the North Sea, *Ocean Science* **13**: 315 – 335.

Mathis, M., Elizalde, A., Mikolajewicz, U. and Pohlmann, T. (2015). Variaiblity patterns of the general circulation and sea water temperature in the North Sea, *Progress in Oceanography* **135**: 91 – 112.

Matthias, V., Bewersdorff, I., Aulinger, A. and Quante, M. (2010). The contribution of ship emmisions to air pollution in the North Sea regions, *Environmental Pollution* **158**: 2241 – 2250.

Merckelbach, L. M. (2016). Depth-averaged instantaneous currents in a tidally dominated shelf sea from glider observations, *Biogeosciences* **13**: 6637 – 6649.

Merckelbach, L. M., Briggs, R. D., Smeed, D. A. and Griffiths, G. (2008). Current measurements from autonomous underwater gliders, *Proceedings of the IEEE/ES/CMTC ninth working conference on current measurement technology*, New York, pp. 61 – 67.

Moffat, C., Owens, B. and Beardsley, R. C. (2009). On the characteristics of Circumpolar Deep Water intrusions to the west Antarctic Peninsula continental shelf, *Journal of Geophysical Research* **114**: C05017.

Mork, M. (1981). Circulation phenomena and frontal dynamics of the Norwegian Coastal Current, *Philosophical Transactions of the Royal Society of London, Series A* **302**: 635 – 647.

National Oceanography Centre, Southampton, U. K. (2008). NOCS Surface Flux Dataset v2.0. Research Data Archive at the National Center for Atmospheric Research, Computational and Information Systems Laboratory: rda.ucar.edu/datasets/ds260.3/ Accessed May 2016.
URL: *rda.ucar.edu/datasets/ds260.3/*

Neumann, H., de Boois, I., Kröncke, I. and Reiss, H. (2013). Climate change facilitated range expansion of the non-native angular crab *Goneplax rhomboides* into the North Sea, *Marine Ecology Progress Series* **484**: 143 – 153.

Núñez-Riboni, I. and Akimova, A. (2015). Monthly maps of optimally interpolated in situ hydrography in the North Sea from 1948 to 2013, *Journal of Marine Systems* **151**: 15 – 34.

Núñez-Riboni, I. and Akimova, A. (2017). Quantifying the impact of the major driving mechanisms of interannual variability of salinity in the North Sea, *Progress in Oceanography* **154**: 25 – 37.

Nurser, A. J. G. and Bacon, S. (2014). The Rossby radius in the Arctic Ocean, *Ocean Science* **10**: 967 – 975.

O'Dea, E. J., Arnold, A. K., Edwards, K. P., Furner, R., Hyder, P., Martin, M. J., Siddorn, J. R., Storkey, D., While, J., Holt, J. T. and Liu, H. (2012). An operational ocean forecast system incorporating NEMO and SST data assimilation for the tidally driven European north-west shelf, *Journal of Operational Oceanography* **5**: 3 – 17.

Ottersen, G., Planque, B., Belgrano, A., Post, E., Reid, P. C. and Stenseth, N. (2001). Ecological effects of the North Atlantic Oscillation, *Oecologia* **128**: 1 – 14.

Otto, L., Zimmerman, J. T. F., Furnes, G. K., Mork, M., Sætre, R. and Becker, G. (1990). Review of the physical oceanography of the North Sea, *Netherlands Journal of Sea Research* **26**: 161 – 138.

Palmer, M. R. (2010). The modification of current ellipses by stratification in the Liverpool Bay ROFI, *Ocean Dynamics* **60**: 219 – 226.

Peperzak, L. (2003). Climate change and harmful algal blooms in the North Sea, *Acta Oecologia* **24**: S139 – S144.

Pingree, R. D. and Griffiths, D. K. (1978). Tidal fronts on the shelf seas around the British Isles, *Journal of Geophysical Research* **83**: 4615 – 4622.

Pingree, R. D., Holligan, P. and Mardell, G. T. (1978). The effects of vertical stability on phytoplankton distributions in the summer of the northwest European shelf, *Deep-Sea Research* **25**: 1011 – 1028.

Pohlmann, T. and Puls, W. (1994). Currents and transport in water, *in* J. Sündermann (ed.), *Circulation and comtaminant fluxes in the North Sea*, Springer-Verlag, Berlin, Germany.

Pond, S. and Pickard, G. L. (1983). *Introductory Dymanical Oceanography*, Pergamon Press, Oxford, United Kingdom.

Prandle, D. (1984). A modelling study of the ^{137}Cs in the seas of the European continental shelf, *Philosophical Transactions of the Royal Society of London, Series A* **310**: 407 – 436.

Queste, B. Y. (2013). *Hydrographic observations of oxygen and related physical variables in the North Sea and western Ross Sea polynya*, PhD thesis, University of East Anglia, Norwich, United Kingdom.

Reiss, H., Greenstreet, S. P. R., Sieben, K., Ehrich, S., Piet, G. J., Quirijns, F., Robinson, L., Wolff, W. J. and Kröncke, I. (2009). Effects of fishing disturbance on benthic communities and secondary production within an intensively fished area, *Marine Ecology Progress Series* **394**: 201 – 213.

Rio, M.-H., Mulet, S. and Picot, N. (2016). Beyond GOCE for ocean circulation estimates: synthetic use of altimetry, gravimetry and in situ data provides new insight into geostrophic and Ekman currents, *Geophysical Research Letters* **41**: 8918 – 8925.

Sætre, R., Aure, J. and Ljøen, R. (1988). Wind effects on the lateral extension of Norwegian Coastal Water, *Continental Shelf Research* **3**: 239 – 253.

Schaeffer, A., Roughan, M., Jones, E. and White, D. (2015). Physical and biological spatial scales of variability in the Eastern Australian Current separation zone from the shelf glider measurements, *Biogeosciences Discussions* **12**: 20101 – 20121.

Schlesinger, M. E. and Ramankutty, N. (1994). An oscillation in the global climate system of 65 – 70 years, *Nature* **367**: 723 – 726.

Schumacher, J. D., Kinder, T. H., Pashinski, D. J. and Charnell, R. L. (1979). A structural front over the continental shelf of the eastern Bering Sea, *Journal of Physical Oceanography* **9**: 79 – 87.

Scotland's National Marine Plan (2015). Scottish government, Edinburgh, United Kingdom.

Sharples, J. (2008). Potential impacts of the spring-neap tidal cycle on shelf sea primary production, *Journal of Plankton Research* **30**: 183 – 197.

Sharples, J., Ross, O. N., Scott, B. E., Greenstreet, S. P. R. and Fraser, H. (2006). Interannual variability in the timing of stratification and the spring bloom in the northwestern North Sea, *Continental Shelf Research* **26**: 733 – 751.

Shaw, P.-T. (1991). The seasonal variation of the intrusion of the Philippine Sea Water into the South China Sea, *Journal of Geophysical Research* **96**: 821 – 827.

Sheehan, P. M. F., Berx, B., Gallego, A., Hall, R. A., Heywood, K. J. and Hughes, S. L. (2017). Thermohaline forcing and interannual variability of northwestern inflows into the northern North Sea, *Continental Shelf Research* **138**: 120 – 131.

Sheehan, P. M. F., Berx, B., Gallego, A., Hall, R. A., Heywood, K. J., Hughes, S. L. and Queste, B. Y. (2018). Shelf sea tidal currents and mixing fronts determined from ocean glider observations, *Ocean Science* **14**: 225 – 236.

Siegismund, F. and Schrum, C. (2001). Decadal changes in the wind forcing over the North Sea, *Climate Research* **18**: 39 – 45.

Simpson, J. H. and Bowers, D. G. (1981). Models of stratification and frontal movement in shelf seas, *Deep-Sea Research* **7**: 727 – 738.

Simpson, J. H. and Bowers, D. G. (1984). The role of tidal stirring in controlling the seasonal heat cycle in shelf seas, *Annales Geophysicae* **2**: 411 – 416.

Simpson, J. H. and Hunter, J. R. (1974). Fronts in the Irish Sea, *Nature* **250**: 404 – 406.

Simpson, J. H. and Sharples, J. (1994). Does the Earth's rotation influence the location of shelf sea fronts?, *Journal of Geophysical Research* **99**: 3315 – 3319.

Simpson, J. H. and Sharples, J. (2012). *Introduction to the Physical and Biological Oceanography of Shelf Seas*, Cambridge University Press, Cambridge, United Kingdom.

Skogen, M. D. and Moll, A. (2005). Importance of ocean circulation in ecological modeling: an example from the North Sea, *Journal of Marine Systems* **57**: 289 – 300.

Souza, A. J. and Simpson, J. H. (1996). The modification of tidal ellipses by stratification in the Rhine ROFI, *Continental Shelf Research* **16**: 997 – 1007.

Souza, A. J., Simpson, J. H., Harikrishnan, M. and Malarkey, J. (2001). Flow structure and seasonality in the Hebridean slope current, *Oceanologica Acta* **24**: S63 – S76.

Su, J. (2004). Overview of the South China Sea circulation and its influence on the coastal physical oceanography outside the Pearl River Estuary, *Continental Shelf Research* **24**: 1745 – 1760.

Sündermann, J. and Pohlmann, T. (2011). A brief analysis of North Sea physics, *Oceanologia* **53**: 663 – 689.

Svendsen, E., Sætre, R. and Mork, M. (1991). Features of the northern North Sea circulation, *Continental Shelf Research* **5**: 493 – 508.

Taylor, A. H. (1987). Modelling contaminants in the North Sea, *The Science of the Total Environment* **63**: 45 – 67.

Thomas, H., Friederike Prower, A. E., van Heuven, S., Bozec, Y., de Baar, H. J. W., Schiettecatte, L.-S. abd Suykens, K., Koné, M., Borges, A. V., Lima, I. D. and Doney, S. C. (2007). Rapid decline of the CO_2 buffering capacity in the North Sea and implications for the North Atlantic ocean, *Global Biogeochemical Cycles* **21**: GB4001.

Thomson, R. E. and Emery, W. J. (2014). *Data Analysis Methods in Physical Oceanography*, Elsevier Science, Amsterdam, the Netherlands.

Trenberth, K. E. and Shea, D. J. (2006). Atlantic hurricanes and natural variability in 2005, *Geophysical Research Letters* **33**: L12704.

Turrell, W. R. (1992). New hypotheses concerning the circulation of the northern North Sea and its relation to North Sea fish stock recruitment, *ICES Journal of Marine Science* **49**: 107 – 123.

Turrell, W. R. and Henderson, E. W. (1990). Transport events within the Fair Isle Current during the Autumn Circulation Experiment, *Estuarine, Coastal and Shelf Science* **31**: 25 – 44.

Turrell, W. R., Henderson, E. W. and Slesser, G. (1990). Residual transport within the Fair Isle Current observed during the Autumn Circulation Experiment (ACE), *Continental Shelf Research* **10**: 521 – 543.

Turrell, W. R., Henderson, E. W., Slesser, G., Payne, R. and Adams, R. D. (1992). Seasonal changes in the circulation of the northern North Sea, *Continental Shelf Research* **12**: 257 – 286.

Turrell, W. R., Slesser, G., Payne, R., Adams, R. D. and Gillibrand, P. A. (1996). Hydrography of the East Shetland Basin in relation to decadal North Sea variability, *ICES Journal of Marine Science* **53**: 899 – 916.

van Leeuwen, S., Tett, P., Mills, D. and van der Molen, J. (2015). Stratified and non-stratified areas in the North Sea: long-term variability and biological and policy implications, *Journal of Geophysical Research: Oceans* **120**: 4670 – 4686.

Verspecht, F., Rippeth, T. P., Howarth, M. J., Souza, A. J., Simpson, J. H. and Burchard, H. (2009). Processes impacting on stratification in a region of freshwater influence: application to Liverpool Bay, *Journal of Geophysical Research* **114**: C110022.

Wakelin, S. L., Artioli, Y., Butenschön, M., Allen, J. I. and Holt, J. T. (2015). Modelling the combined impacts of climate change and direct anthropgenic drivers on the ecosystem of the northwest European continental shelf, *Journal of Marine Systems* **152**: 51 – 63.

Winther, N. G. and Johannessen, J. A. (2006). North Sea circulation: Atlantic inflow and its destination, *Journal of Geophysical Research* **111**: C12018.

Zhang, X., Hu, L. and He., M. X. (2009). Scattering by pure seawater: effect of salinity, *Optics Express* **17**: 5698 – 5710.